2009

Simulations of Turbulence over Superhydrophobic Surfaces

Michael B. Martell
University of Massachusetts Amherst

SIMULATIONS OF TURBULENCE OVER SUPERHYDROPHOBIC SURFACES

A Thesis Presented

by

MICHAEL B MARTELL JR

Submitted to the Graduate School of the
University of Massachusetts Amherst in partial fulfillment
of the requirements for the degree of

MASTER OF SCIENCE IN MECHANICAL ENGINEERING

February 2009

Mechanical and Industrial Engineering

SIMULATIONS OF TURBULENCE OVER SUPERHYDROPHOBIC SURFACES

A Thesis Presented

by

MICHAEL B MARTELL JR

Approved as to style and content by:

Jonathan P. Rothstein, Co-chair

J. Blair Perot, Co-chair

Thomas J. Lardner, Member

Mario Rotea, Department Head
Mechanical and Industrial Engineering

ACKNOWLEDGMENTS

Thank you to my family for pushing me up the ladder, and to Amy for her patience. Many thanks to Blair Perot for enduring countless questions and rounds of debugging. Thanks to Jonathan Rothstein for his continuous support and guidance. Thanks to Jay Gadebusch, David Hebert, Shivasubramanian Gopalakrishnan, Sandeep Menon, Professor David Schmidt and Venkataramanan Subramanian for their invaluable help with all things CFD and Linux. Thanks to Geoff Moss, Michael Nilsson, Kshitij Neroorkar, Dnyanesh Digraskar, Kaustubh Rao, Raghuveer Sesha Vajapeyayajula, Nat Trask, and Hot T for making the lab a fun place to work.

The author would also like to thank the Office of Naval Research for their support under grant N00014-06-1-0497.

Written in LaTeX 2$_\varepsilon$ using BibTeX

ABSTRACT

SIMULATIONS OF TURBULENCE OVER SUPERHYDROPHOBIC SURFACES

FEBRUARY 2009

MICHAEL B MARTELL JR

B.S., NORWICH UNIVERSITY

Directed by: Professor Jonathan P. Rothstein and Professor J. Blair Perot

Significant effort has been placed on the development of surfaces which reduce the amount of drag experienced by a fluid as it passes over the surface. Alterations to the fluid itself, as well as the chemical and physical composition of the surface have been investigated with varying success. Investigations into turbulent drag reduction have been mostly limited to those involving bubbles and riblets. Superhydrophobic surfaces, which combine hydrophobic surface chemistry with a regular array of microfeatures, have been shown to provide significant drag reduction in the laminar regime, with the possibility of extending these results into turbulent flows. Direct numerical simulations are used to investigate the drag reducing performance of superhydrophobic surfaces in turbulent channel flow. Slip velocities, wall shear stresses, and Reynolds stresses are considered for a variety of superhydrophobic surface micro-feature geometry configurations at friction Reynolds numbers of $Re_\tau = 180$, $Re_\tau = 395$, and $Re_\tau = 590$. This work provides evidence that superhydrophobic surfaces are capable of reducing drag in turbulent flow situations by

manipulating the laminar sublayer and turbulent energy cascade. For the largest micro-feature spacing of $90\mu m$ an average slip velocity over 80% of the bulk velocity is obtained, and the wall shear stress reduction is found to be greater than 50%. The simulation results suggest that the mean velocity profile near the superhydrophobic wall continues to scale with the wall shear stress, but is offset by a slip velocity that increases with increasing micro-feature spacing.

TABLE OF CONTENTS

LIST OF TABLES

Table **Page**

LIST OF FIGURES

Figure **Page**

CHAPTER 1

INTRODUCTION

1.1 Motivation

With the ever-increasing cost and scarcity of energy resources facing the planet today, many in the scientific community have begun to focus on technology which increases the efficiency, and decreases the fuel consumption, of transportation systems. In 2006, the United States received nearly 420 million short tons of imported goods by means of tanker, dry-bulk carrier, container, and freighter vessel, which constitutes 72% of all imports into the country [3].

Considering the prominence of ocean-borne transport, there is no question as to why a significant amount of research has focused on reducing the energy requirements of waterborne craft. The development of a safe, cost-effective means of reducing drag experienced by ocean going ships would have far reaching consequences, including reducing global consumption of fossil fuels, decreasing response time of defense and rescue vessels, and adding knowledge and expertise to the field of turbulent fluid flow.

A few back-of-the envelope calculations can be performed to estimate the energy consumed and pollution generated by a typical ocean going cargo vessel. As an example, consider a Suezmax Crude Carrier ship, with a gross tonnage of 81,000 tons, operating a 22,000 brake horse power engine at 91 rotations per minute, traveling at a typical cruising speed of 15.5 knots. The engine burns heavy fuel oil [4], often called residual, or "#6" oil, which currently costs 0.44 USD per kilogram [1]. The Suezmax crude carrier burns an average of 56 metric tons of heavy fuel oil per day [4], which is nearly $25,000 USD per day at the current price and quoted operating conditions.

This fuel consumption is a function of the load the vessel is carrying, and the resistance the ship experiences as it travels through the water, as well as other factors such as engine efficiency, fuel energy density, the weather, the location of the ship, and the temperature of the water. Here, a typical cargo load will be assumed, and only the ships resistance to motion will be considered. The total resistance experienced by a typical cargo ship can be separated into the resistance due to friction, the wave resistance, the eddy resistance, and the air resistance. For a slow-moving vessel (such as a cargo vessel), the friction drag represents nearly 90% of the total drag [2]. If, by applying a superhydrophobic surface to the hull of the Suezmax Crude Carrier, one could reduce the friction drag by 25%, then the overall drag experienced by the ship could be reduced by 22.5%. This could translate directly into a 22.5% savings in fuel consumption, recovering over $5,500 USD per day, and a 22.5% reduction in equivalent CO_2 emissions, preventing over 43 metric tons of pollution from entering the atmosphere [6].

1.2 Background

When an object passes through a fluid it experiences drag. Drag can be thought of as friction between the fluid and the object, as well as friction experienced within the fluid itself. The drag an object feels as it passes though a fluid is directly related to the amount of effort required to move the object. The less drag an object experiences, the easier it will be to move that object. For a given *pressure drop* down a channel, the mass and volume flow rates are directly related to the drag the fluid experiences as it passes through the channel. Often, it is desirable to reduce the amount of drag resulting from the interaction between the fluid and the object, be it a channel, a pipe, or the hull of an ocean vessel. With this goal in mind, it is logical to examine the relationship between the surface of the object and the amount of drag the fluid experiences while passing over this surface.

There is a growing volume of research suggesting that drag reduction is achievable in both the laminar [33, 34, 45] and turbulent flow regimes [22, 16, 26, 18, 11]. In many cases, drag reduction is obtained by manipulating the surface of the object which the fluid passes over. Some methods alter the fluid properties by the addition of long chain polymers or bubbles [30], or by the use of active blowing and suction [22]. These hydrophobic methods, however, only operate on nanometer length scales, and are not effective at producing drag reduction in macroscopic flows. Many methods change the surface geometry, adding features such as riblets [12], compliant walls [19], ridges, or posts. Macro-scale laminar drag reduction is possible with liquids using surface or fluid electric charges ([25]), and via surface chemistry (surface hydrophobicity) ([44]). A theoretical analysis by [16] suggests how a small alteration of the laminar sublayer can affect the entire turbulent boundary layer and subsequently alter the drag. Recent work [33, 34, 16] has focused on surfaces that employ both chemical and geometric attributes to achieve high levels of drag reduction. These surfaces, often called *ultra-* or *superhydrophobic* surfaces, were employed by Ou, *et al.* [33, 34] and Joseph, *at al.* [21] in their study of laminar drag reduction in microchannels, and gave impetus to the current research into turbulent drag reduction.

1.2.1 Superhydrophobic Surfaces

Ou, *et al.* [33, 34] investigated laminar drag reduction using superhydrophobic surfaces in microchannels. By understanding the physical mechanism of superhydrophobic drag reduction, it was possible to configure the microfeatures on the surface for optimal drag reduction performance. In a general sense, the standard measure of a surface's hydrophobic characteristics involves the angle that a fluid droplet's free surface forms when put into contact with a solid object, called the *contact angle*, θ. Here, the contact angle we refer to is the *advancing* contact angle. On wetting (non-hydrophobic, or *hydrophilic*) surfaces such as glass, where by definition $\theta < 90°$,

the droplet will be nearly flat, thus it will have a contact angle very close to $\theta \approx 0°$ [20].

On hydrophobic surfaces, the contact angle is greater than $\theta > 90°$. *Super*hydrophobic surfaces have been developed which support a contact angle approaching $\theta \approx 177°$ [7, 9, 32]. Figure 1.1 shows plan-view micrographs of two superhydrophobic surfaces, one with microridges and the other with microposts. The features are etched into silicon wafers, then treated to be chemically hydrophobic. Studies of these superhydrophobic surfaces [32] have shown that the performance of the surface (namely, the droplet contact angle) is a function of the geometric arrangement of the microposts and microridges, and has little to do with the chemical hydrophobicity as long as $\theta > 90°$. Considering the findings in [32], the performance of such superhydrophobic surfaces could be analyzed through simulation [34], where the geometry of the microfeatures, such as sizing, spacing, and height, could be altered, and a parametric study performed.

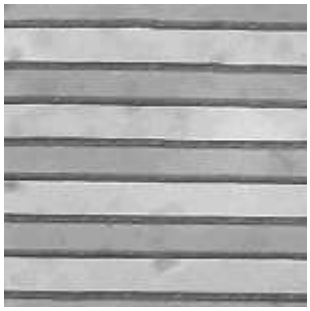

(a) Microridges approximately 30 μm wide, spaced at 30 μm.

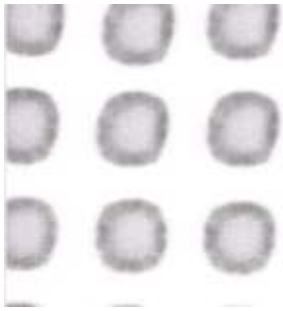

(b) Microposts approximately 30 μm in diameter, spaced at 30 μm.

Figure 1.1. Examples of superhydrophobic surface features.

Before any serious discussion of simulating superhydrophobic surfaces occurs, a better understanding of the physical arrangement of such surfaces is required. Figure 1.2 shows a model of the superhydrophobic surfaces studied. The surface is assumed to be rough, with a regular pattern of micron-sized ridges or posts covering it. The

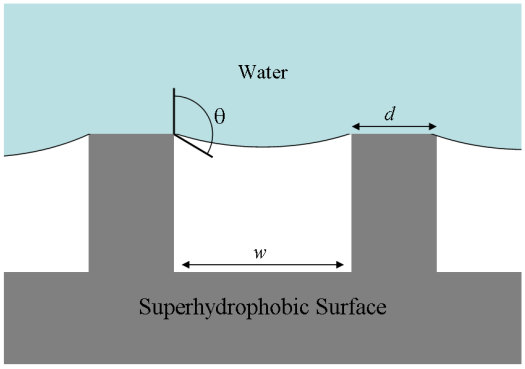

Figure 1.2. A schematic representation of the interaction between fluid and microfeatures with hydrophobic surface coating.

surface is made to be hydrophobic through chemical treatment. If the feature spacing is sufficiently small, and the applied pressure sufficiently low (for a discussion of what a "sufficiently low" applied pressure is for these surfaces, see section 1.2.2.1), then a fluid, covering the surface, will not fall into the space between the posts or ridges. Instead, the water is repelled, and touches only as many microposts or ridges as necessary to support the interface shown. This model was verified in Ou's work [33], and the deflection of the interface with increasing pressure was quantified. A simplified version of this model is used for simulations of both laminar and turbulent flow over such surfaces, and is employed to explain the reason for observed drag reduction in laminar flows.

1.2.2 Laminar Drag Reduction

1.2.2.1 Effective Surface Area

The majority of existing research into the drag reducing capacity of superhydrophobic surfaces has involved flow in the laminar regime. In many cases, this is due to the presence of analytical solutions for simple (not hydrophobic) flow arrangements in channels, pipes, and parallel infinite plates [14, 47, 41], as well as Philip's work [39, 40, 24] on flow over alternating no-slip and no-shear boundary conditions.

With a few assumptions, an examination of laminar flow over these surfaces can lead to a basic understanding of the mechanism at work.

If it is assumed that the interface formed between the microfeatures is unaffected by the fluid motion above that interface, and we only consider a static analysis of the problem, Young's Law may be employed to determine the pressure difference that can be supported by the interface, given a microfeature spacing of w [46]:

$$\Delta p = p_w - p_a = \frac{4\gamma}{w\cos(\pi - \theta)} \tag{1.1}$$

where γ is the surface tension of the fluid in question and θ is the contact angle, as previously described. It is important to point out two observations from Equation 1.1. First, if the contact angle that the fluid forms with the surface falls below 90° ($\frac{\pi}{2}$), the cosine term will fall below zero, and no interface will be supported. Similarly, for a given pressure, if w is increased beyond a certain limit, the interface will not be maintained. This was shown in the work of Öner and McCarthy [32]. Of course, the same result will occur if the pressure exerted by the fluid (here, p_w) is too high. With this in mind, given the proper contact angle, feature spacing, and pressures, the fluid rests only on the tops of the microfeatures, and has large areas of free surface between them. If these free surfaces are treated as having no shear, then drag can now only occur at the tops of the microfeatures, which may represent only a fraction of the surface area. Thus, the surface has a much smaller "effective" area to impart drag to the fluid. This, however, will be counteracted by an increase in drag at the tops of the microfeatures. Thus, any overall drag reduction will be a result of the difference between drag decrease due to less effective surface area, and drag increase on the top of the microfeatures. The drag reduction observed in prior work implies that, for large post spacings, the decrease in drag due to lessened effective surface area far outweighs the increase in drag over the tops of the microridges. Conversely, for small post spacings, these two effects will exactly cancel each other, resulting in little to no

drag reduction. It is important to point out that it has been shown experimentally [33] that the drag experienced on the surface of microridges does **not** increase with increased free-surface area.

1.2.2.2 Slip Velocity and Slip Length

A common way of the measuring global or *macroscopic* effect of a superhydrophobic surface involves the *slip velocity* or *slip length* experienced by the fluid at the surface. Before a discussion of the subject is presented, it is important to explain the difference between the macroscopic and microscopic effects occurring on a superhydrophobic surface. We begin with the definition of the slip length, b [47]:

$$b \equiv \frac{u_{slip}}{\left(\frac{\partial u}{\partial y}\right)_{y=0}} \tag{1.2}$$

where u_{slip} is the average velocity at the superhydrophobic surface, and $\left(\frac{\partial u}{\partial y}\right)_{y=0}$ is the *shear rate* at the wall, taken in the vertical direction. It is important to emphasize the use of the term *average* velocity above, because locally (microscopically), the varying boundary conditions presented by the superhydrophobic surface will produce regions where the velocity at the surface (the local, or microscopic u_{slip}) is zero, and other regions where the local shear $\left(\frac{\partial u}{\partial y}\right)$ is essentially zero, resulting is a large local slip velocity and slip length. Considering this, only a planar average of the velocities or shear rate gradient on the surface will result in an *average* slip velocity or slip length. This concept is key to understanding the way boundary conditions are handled in the simulations, as well as how average statistics are computed.

Equation 1.2 references the physical description shown in Figure 1.3. Again, this is to be taken in a macroscopic, or global sense when considering superhydrophobic surfaces.

Microscopically, two assumptions are made about the behavior of the fluid as it interacts with the microfeatures, and as it interacts with the free surface between (and supported by) the microfeatures. An understanding of these two assumptions becomes important when considering the way boundary conditions are implemented in the numerical simulations. In simulations, the surfaces of the microfeatures are taken to be no-slip, meaning all of the fluid comes to rest at the surface. Similarly, the suspended liquid-gas interface between the microfeatures is approximated as flat and shear-free, meaning the fluid experiences no local drag in those regions and the surface experiences no out-of-plane deflection. In addition, a no-penetration boundary condition is applied for both regions. Recent work by Ybert, *et al.* [48] comments that curvature effects of the shear-free interface is only important when considering surfaces with arrays of holes, where the underlying gas (air) is not connected to other gas reservoirs. This is not the case with microridges or microposts, where the regions of gas in between the features are connected. The free-surface in these simulations is assumed to experience no out-of-plane deflection. When the ratio of the deflection, s, to the gap width, w, is small, $s/w \ll 1$, the deflection can be well approximated by $s/w \approx (w\Delta p)/(8\sigma)$, where σ is the surface tension. For our maximum gap size of $90\mu m$ and water with $\sigma = 7 \times 10^{-2}$ N/m, pressures up to 700 Pa can be supported with deflections of less than ten percent. This spacing is near the upper limit of what

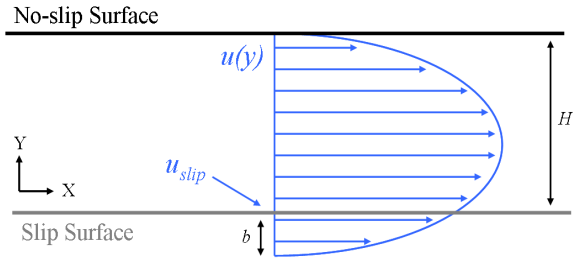

Figure 1.3. A schematic representation of the slip velocity and slip length at a slip (shear-free) interface. Adapted from [33].

can be effectively employed experimentally. The work of [48] confirms that deflections of less than twenty percent produce negligible effects on laminar drag reduction. The assumption of shear-free flow on the free surface is reasonable if the posts and ridges are tall enough (*i.e.* same order of magnitude as the spacing). If the posts or ridges are significantly shorter than the gap width, then the circulating air in the gap between the micro-features could result in drag on the free-surface and cause such a surface to produce less drag reduction than these DNS calculations predict.

The local boundary conditions presented above are a close approximation to reality. Again, Figure 1.3 shows a schematic of slip velocity and slip length at an interface. Physically, if the interface is one between a fluid and a solid, the value of b will be very small (on the order of the fluid molecule size), as will the value of u_{slip}. Thus, assuming zero velocity at a solid surface is a close approximation to reality. If the interface is between two fluids (a liquid and a gas, in the case of the suspended interface between microfeatures), however, the value of u_{slip} and b will not be small, and in fact may be quite large. Although the fluid does experience some drag at this interface, it is very small compared to the drag experienced at the solid surface, thus the approximation of no drag is sufficient. It is important to point out that, in reality, this assumption only holds for features with depths above a certain limit. In the case of very shallow features, the resistance to motion provided by the gas between the features is nontrivial. For this research, the boundary conditions employed are not capable of reproducing this physical situation.

1.2.3 Turbulent Drag Reduction and Delayed Transition

Work by Kim [22] and others has revealed that, as is the case with laminar flows, the manipulation of the of the near-wall region is key to reducing the drag imparted to turbulent flows. Many different methods have been investigated, including the use of hydrophobic surfaces with an assumed slip length [26, 27], permeable walls [19],

bubbles [42], so-called active control of the boundary layer [22], and most recently, superhydrophobic surfaces [16].

In Min and Kim's studies of hydrophobic surfaces [26, 27], direct numerical simulations of a turbulent channel were performed. The channel walls were given boundary conditions that assumed a known, constant slip length in both the streamwise and spanwise directions. As was shown in Equation 1.2, the slip velocities in both those directions (here, u_s and w_s) were proportional to the assigned slip length and the wall shear rate:

$$u_s = L_s \frac{\partial u}{\partial y}\bigg|_{wall}, \; w_s = L_s \frac{\partial w}{\partial y}\bigg|_{wall} \tag{1.3}$$

Min, *et al.* assumed, however, that the slip length was independent of the shear rate, allowing the slip length to be a set constant for the simulations. This assumption is somewhat non-physical, as it essentially applying a macroscopic boundary condition (as described previously) to microscopic boundary conditions. Furthermore, the assumption of a slip length will **always** result in drag reduction when compared to a perfect no-slip surface, considering the relationship between the slip length and the shear at the wall shown in Equation 1.2. Min's simulations monitored the pressure drop for a given mass flow rate down the channel, and calculated the skin-friction drag. This was then compared to the pressure drop across the channel with regular no-slip walls, and the percent difference between the two was recorded. Min, *et al.* found that up to a 17% pressure drop reduction could be achieved for a slip length of 3.566 wall units (normalized by the wall shear velocity of no-slip walls) in both the streamwise and spanwise directions, which is not surprising considering their assumption of a constant slip velocity could not lead to any other conclusion. More importantly, Min and Kim concluded that hydrophobic surface boundary conditions play a major role in the evolution and behavior of near-wall turbulence, and thus of measured pressure drop reduction. Min and Kim also investigated the effect of hydrophobic surfaces on turbulent stability and transition [27] using a similar setup

as described previously. They concluded that the effect of slip on turbulent transition was proportional to the slip length set in the simulations, and that even very small slip lengths have a large effect on transition, namely an increase in the critical Reynolds number with increased slip length, and an increased delay for transition to turbulence with increased slip length.

Changing focus from simulation to experiment, research into turbulent drag reduction was done by Sanders, *et al.* [42] at length scales and Reynolds numbers much larger than previous experiments. Sanders *et al.* made use of a large channel with specially designed walls. In an attempt to control the boundary layer of the fluid near the walls, a large amount of small bubbles were injected into the flow. Although difficult to control and keep at the wall, the investigators were able to form a continuous air pocket on the upper wall of the channel, approximating a large region of shear-free surface. The presence of this gaseous film led to a wall shear stress reduction of nearly 100%. It was concluded that, even when bubble dimensions were much larger than the smallest turbulent structures in the flow, skin friction drag reduction will be achieved assuming a sufficient number of bubbles are located near the walls of the channel [42].

Another method of altering the nature and evolution of near-wall turbulent structures, and hence the drag experienced at those walls, involves making the surfaces permeable. Work by Hahn, *et al.* [19], along with earlier investigations into the nature of near-wall turbulence done by Perot and Moin [38], suggests that permeable walls in turbulent channel flow lead to significant skin-friction reduction at the permeable wall, and can affect changes in the turbulent intensities and Reynolds stresses in the channel. The work also suggested that the skin-friction drag reduction was a function of the boundary layer thickness, which is related to many factors, including the Reynolds number of the flow in question.

A subject that has attracted much attention in the recent past is that of riblets. The work of Choi *et al.* [10] performed direct numerical simulations of turbulent flow over riblets, which consisted of streamwise-oriented triangular ridges which did not support an interface, unlike the ridges and posts found on superhydrophobic surfaces.

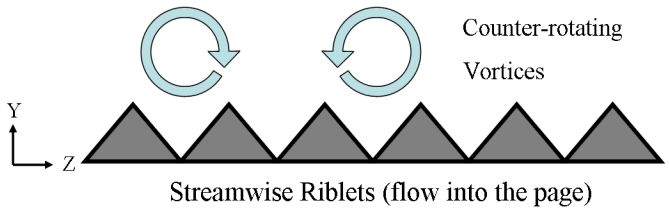

Figure 1.4. Riblets of the type investigated by Choi *et al.* with arrows depicting the turbulent vortex size in comparison to the riblet size.

As is shown in Figure 1.4, the size of the turbulent vortices were such that they scaled closely with the size of the riblets, and aligned themselves with the valleys of the riblets. This alignment led to diminished vortex interaction, which led to marked drag reduction on the ribbed wall. The size of the vortices is directly related to the Reynolds number of the flow, thus riblets of a certain size would only reduce drag for a certain small range of Reynolds numbers. Outside of that range, the vortices would be small enough to group inside of the riblet valleys, thus interacting, or large enough to ride atop the riblet peaks, again allowing for interaction.

To complete the brief review of the state of turbulent drag reduction, the recent work of Fukagata, Kasagi, and Koumoutsakos [16] will be considered. In their work, Fukagata, *et al.* presented a model for the prediction of drag reduction that could be achieved by superhydrophobic surfaces using Min's [26] assumption of a constant, known slip length for the surface in question. Their work suggested that significant drag reduction was achievable for Reynolds numbers up to and exceeding $10^5 - 10^6$ if the surface in question were able to sustain a certain slip length [16]. As with Min's work, this assumes a macroscopic-type boundary condition (a slip length) based on

a sort of averaged slip velocity and shear, which is somewhat non-physical. Fukagata points out that this assumption of an average slip length may only be valid for features below the Kolmogorov scale (see [41]), thus only applying to nanoscale surface features, which are at least an order of magnitude smaller than the superhydrophobic surface feature sizes investigated in the current work. Nevertheless, Fukagata goes as far as to estimate that superhydrophobic surfaces may be able to achieve upwards of 25% drag reduction, even when placed in an extremely high Reynolds number environment, such as the flow around an oil tanker.

1.3 Goals and Objectives

There are three major goals associated with this research, all of which have been met. First and foremost, a thorough understanding of the mechanism involved in turbulent drag reduction was obtained. This knowledge allows the observed drag reduction to be explained, and provides necessary focus for future study. Second, similar to work done in the laminar regime, the relationship between microfeature geometry and the drag reduction performance of a surface was determined. Finally, the relationship between the Reynolds number and drag reduction was discovered, and helped to characterize the surface performance in various flow regimes and determine physical situations where the superhydrophobic surfaces will be useful.

There are many objectives, both major and minor, which lent themselves to the successful completion of this research. Initial objectives centered around the development of the direct numerical simulation (DNS) code. They included implementation of the boundary conditions and the pressure gradient, development of the temporal statistics gathering mechanism, and a significant amount of debugging, along with making the code parallel, and able to run on supercomputers. These objectives have been met.

After the initial code development, the objectives shifted towards validation, and included benchmarking the code against known laminar flow solutions, including those of laminar flow over bands of no-slip and no-shear surfaces. Also, an investigation into laminar flow over superhydrophobic surfaces was performed, in which increases or decreases in mass flow rate for a fixed pressure gradient could be observed, along with the affect of non-aligned (angled) laminar flow over these surfaces. Similar to the validation performed in the laminar regime, a major objective of the first phase of research involved benchmarking the DNS code against known turbulent channel results. These objectives have also been met.

Once work in the laminar regime was completed, and the code was successfully validated against existing turbulent channel flow data, the project's primary objectives could be considered. They included investigating the effect superhydrophobic surfaces have on wall shear stress, Reynolds stresses, and slip velocities or slip lengths in turbulent channel flow. In addition, simulations were performed with several different surface feature sizes and spacings and at several different Reynolds numbers. This allowed the relationship between wall slip velocity, shear stress, surface geometry, and Reynolds number to be characterized.

CHAPTER 2

DIRECT NUMERICAL SIMULATIONS

2.1 Background

In order to fulfill the goals and objectives present in this work, it was necessary to developed a computational fluid dynamics (CFD) code which could simulate turbulent channel flow over a variety of boundary conditions, such as those equivalent to microridges and microposts. Although there are several CFD packages available which could perform this task, developing one using a pre-existing in-house code had many benefits, both practical and educational. First and foremost, an in-house code has no "black box" components, enabling the user to access and understand all portions of the code. Second, the nature of the boundary conditions are such that a detailed knowledge of their implementation was necessary in order to interpret the results from the simulations. In addition, having a fully accessible and well understood code base enabled others to collaborate on extending and validating the code, yielding a more robust and feature rich piece of software. This was evidenced recently by the addition of improved sparse matrix solver exit criteria, heat transfer, and forced turbulence capabilities to the original CFD code. Finally, developing a code "by hand" provides an excellent understanding of the physics, mathematics, and numerical methods behind CFD, whereas the use of a commercial or pre-compiled CFD code would provide results with little to no understanding of the means employed to reach those results.

The direct numerical simulation (DNS) method was employed for the current work. Often, DNS methods are used for fundamental research which does not require extremely high Reynolds number flow to be simulated. This method was chosen over

one which uses turbulence models for several reasons. Although computationally expensive, DNS provided the most accurate results as it is able to resolve both large and small length scales. This is especially important to the current research as superhydrophobic surfaces affect turbulent flows in the boundary layer region, where relevant length scales are small. In addition, these small perturbations affect larger length scales, thus making it imperative to be able to resolve all relevant scales in the flow.

The CFD code used to carry out simulations was originally developed by Prof. Blair Perot here at the University of Massachusetts, Amherst. The code was designed to simulate isotropic, homogeneous decaying turbulence using models such as k-ϵ and k-ω (see [41] for details on these turbulence models). The original code employed a second-order-accurate finite volume scheme with a uniform staggered Cartesian mesh. The code solved the discreet form of the incompressible Navier-Stokes equations numerically, and employed a third-order Runge-Kutta time marching scheme. The original code was heavily modified for use on this project. The turbulence models were removed, the mesh was altered to support non-uniform spacing, the appropriate boundary conditions were added, and a means of collecting both temporally- and spatially-averaged velocity and pressure fields was added. In addition, the ability to set a constant pressure drop across the computational domain in both the streamwise and spanwise direction was added, and the code was parallelized for use on supercomputer clusters.

2.2 Numerical Methods

The CFD code is written in FORTRAN 95 and performs direct numerical simulations on turbulent channel flows. The code resolves the pressure, and the three velocity components, at every grid point in its domain, at every fractional time step. The governing Navier-Stokes equations are numerically solved using a Cartesian stag-

gered mesh method with classical projection for the pressure solution. This mesh has non-uniform spacing in the vertical direction, allowing greater resolution near the channel's top and bottom walls. A Cartesian mesh is well suited to the channel and microfeature geometry being investigated. A staggered scheme is employed for several reasons. First, the method conserves mass and momentum, as well as vorticity and kinetic energy. There is no numerical viscosity or artificial dissipation inherent to the scheme (see [5, 37] for more details), which is vital to accurately predicting the turbulent energy cascade (see [41, 28]). Thus, this scheme is well suited for fundamental research into the behavior of turbulence, as it quite accurate in its simulation of the physics of the flow. The numerical method is second-order accurate in space and time and locally conserves mass and momentum. The code is fully parallel, using MPI libraries, and optimized for execution on supercomputers. The solution domain is broken in to numerous sub-domains, which are then handled on individual processors or cores.

The code uses the discretized form of Navier-Stokes for fluid flow. The equations accurately describe the motion of a continuum of particles in fluids or gases. The change in momentum is derived on a small scale from pressure differences and the friction between fluid molecules, also frequently referred to as viscous forces. These changes in momentum are based on conservation of momentum, through which the motion of fluids can be calculated. Two of the three areas of conservation that apply to any volume of incompressible fluid are the conservation of mass and momentum (conservation of energy does not apply to the incompressible Navier-Stokes equations).

The incompressible form of the Navier-Stokes equation for a Newtonian fluid has several components to it, which will be defined here [47]. $\frac{D\boldsymbol{u}}{Dt}$ is the substantial derivative, while the density of the fluid is represented by ρ, the pressure field by p, dynamic viscosity by μ, and the rate of deformation tensor $\mathbf{S} = \frac{1}{2}\left(\nabla \boldsymbol{u} + \nabla \boldsymbol{u}^T\right)$. The use of bold, italicized letters indicates a vector, whereas a bold indicates a tensor. For

example, in Cartesian coordinates, the velocity $\boldsymbol{u}$ would translate into u, v, and w. In incompressible flow, $\nabla \cdot \boldsymbol{u} = 0$, which represents conservation of mass. Assuming constant viscosity, Navier Stokes can be simplified.

$$\rho \frac{D\boldsymbol{u}}{Dt} = -\nabla p + 2\mu \nabla \cdot \mathbf{S} \tag{2.1}$$

where $\rho \boldsymbol{f}$ term is removes because body forces (gravity) are neglected. The $\nabla \cdot \mathbf{S}$ term, which is the divergence of the strain rate tensor, can be simplified.

$$\nabla \cdot \mathbf{S} = \frac{1}{2} \nabla^2 \boldsymbol{u} \tag{2.2}$$

Substituting Equation 2.2 into Equation 2.1 yields the conservative form of Navier Stokes, which is what the DNS code solves numerically.

$$\frac{D\boldsymbol{u}}{Dt} + \nabla \cdot (\boldsymbol{u}\boldsymbol{u}) = -\nabla \frac{p}{\rho} + \nu \nabla^2 \boldsymbol{u} \tag{2.3}$$

where ν is the kinematic viscosity, defined as $\nu \equiv \frac{\mu}{\rho}$. Equation 2.3 is the form of the Navier Stokes equation solved numerically in the CFD code, with ρ and ν constant. The simplified form of Navier-Stokes can be thought of as having a convective, a diffusive, and a pressure term which contribute to the evolution of the velocity $\boldsymbol{u}$ through time.

$$u_i^{n+1} = u_i^n + (C_i + D_i - \nabla p)\, \Delta t \tag{2.4}$$

where C, D, and p represent the convection, diffusion, and pressure terms, respectively, the subscript i indicates discretization in space, and the superscript n indicates discretization in time.

Equation 2.4 represents Euler explicit advancement, shown in [15]. The code uses a segregated approach of advancement by means of the fractional step method. This allows for Equation 2.4 to be separated and solved incrementally (see [35, 36]).

$$\begin{aligned}\hat{\mathbf{u}}_i^{n+1} &= \mathbf{u}_i^n + \left[C_i\left(\mathbf{u}_i^n\right) + D_i\left(\mathbf{u}_i^n, \mathbf{u}_i^{n+1}\right) - \nabla p_i^n\right]\Delta t \\ \mathbf{u}_i^{n+1} &= \hat{\mathbf{u}}_i^{n+1} - \nabla\left(p_i^{n+1} - p_i^n\right)\Delta t \end{aligned} \tag{2.5}$$

where $\nabla^2\left(p_i^{n+1} - p_i^n\right)\Delta t = \nabla \cdot \hat{\mathbf{u}}_i^{n+1}$ since $\nabla \cdot \mathbf{u}_i^{n+1} = 0$.

Spatial derivatives in the Cartesian mesh are relatively straight forward, as the locations of every value are known simply from the structure of the mesh. For example, the derivative of the variable ϕ in the vertical direction y would be calculated via

$$\left(\frac{\partial^2\phi}{\partial y^2}\right)_i \approx \frac{\frac{\phi_{i+1}-\phi_i}{y_{i+1}-y_i} - \frac{\phi_i-\phi_{i-1}}{y_i-y_{i-1}}}{\frac{1}{2}\left(y_{i+1} - y_{i-1}\right)} \tag{2.6}$$

where the subscript i indicates discretization in space. The information above provides a basic understanding of the spatial discretization that is employed in the CFD code.

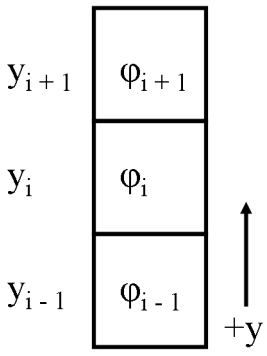

Figure 2.1. An illustration of the discrete derivative shown in Equation 2.6.

For temporal discretization, the program utilizes a three step Runge-Kutta time marching method (RK3), which is second order accurate. Denoting intermediate

solution steps as $\tilde{y}$ and $\tilde{\tilde{y}}$, we arrive at the following low storage, second order accurate form of the hybrid RK3 found in the code:

$$\begin{aligned} \tilde{y}_{n+\frac{1}{2}} &= y_n + \left(\frac{1}{2}\Delta t\right) \cdot f\left(y_n\right) \\ \tilde{\tilde{y}}_{n+1} &= y_n + (\Delta t) \cdot f\left(\tilde{y}_{n+\frac{1}{2}}\right) \\ y_{n+1} &= \tilde{y}_{n+\frac{1}{2}} + \left(\frac{1}{2}\Delta t\right) \cdot f\left(\tilde{\tilde{y}}_{n+1}\right) \end{aligned} \tag{2.7}$$

where $\tilde{y}_{n+\frac{1}{2}}$ represents the velocity **and** pressure information, as described in Equation 2.5. The first step of RK3 uses the explicit Euler method to arrive at a solution at one half the time step. The code then uses this "midpoint" solution to "leapfrog" to the end of the time interval. Finally, it performs an implicit Euler solution to arrive at a reasonably accurate solution at the next time step. The low storage method trades off accuracy for minimal storage. Only two arrays need be stored for any given calculation, the solution from the previous step, y_n, and the result of the previous intermediate step $\tilde{y}$ or $\tilde{\tilde{y}}$. The above information provides a basic understanding of the temporal discretization that is employed in the CFD code. The conjugate gradient (CG) method is employed as the sparse matrix solver. A much more thorough look at CG can be found in [43], and basic operation of the algorithm is presented in Appendix A.

2.3 Mesh

The code employs a stationary Cartesian mesh. Non-uniform spacing of the Cartesian mesh is included in the vertical direction throughout the computational domain. This is to better resolve boundary layer phenomena at the walls, where the focus of the project lies. This scheme also saves computational power and storage near the center of the channel, where there is little interest in resolving very small scales. The

grid spacing in the streamwise and spanwise directions is uniform across the entire domain.

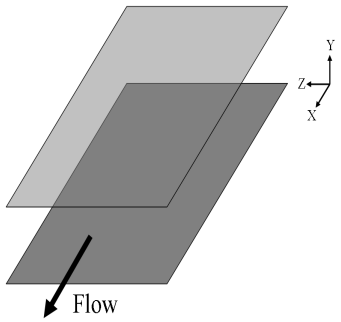

(a) The computational domain.

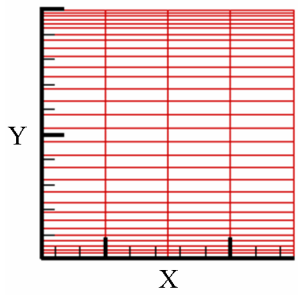

(b) An example of the non-uniform mesh spacing with $C = 0.01$ and $DNY = 32$.

Figure 2.2. Two schematics illustrating the mesh used in the code. X is the streamwise direction, Y the vertical direction, and Z the spanwise direction.

In Figure 2.2, the vertical mesh spacing reaches a high degree of nonuniformity approaching the top and bottom of the domain, and the spacing is symmetric about the center of the channel. This is achieved by employing a hyperbolic tangent function to dictate the mesh spacing at every vertical location. The function returns the location of the "top" of each finite volume, here $f(i)$:

$$f(i) = \left[\frac{\tanh\left(\left(i - \frac{DNY}{2}\right) \cdot C\right)}{\tanh\left(\left(DNY - \frac{DNY}{2}\right) \cdot C\right)} \right] \cdot \frac{LY}{2} \tag{2.8}$$

Here, DNY is the total number of grid points in the Y (vertical) direction, i is the index location of the spacing being calculated (here, i will run from 0 to DNY), LY is the physical length of the domain in the vertical direction, and C is a scalar constant set by the user which dictates the degree of non-uniformity applied to the mesh.

As previously discussed, the code employs a *staggered* Cartesian mesh. The term *staggered* may not immediately imply its meaning, unlike Cartiesian, which simply means the mesh is Cartesian in all three dimensions. A staggered mesh is one that

stores field variables, such as velocities, pressures, and viscosities at different locations. The smallest "unit" of a finite volume mesh (and the one employed here) is a finite volume, often called a cell. For a Cartesian mesh, each cell is a cuboid hexahedron, whose faces are rectangular and perpendicular. Each cell is aligned with the global coordinate system (unlike a moving or unstructured mesh), so each face can have a certain velocity component assigned to it. In addition, the center of the cell often is employed to store scalar information, such as pressure or viscosity. Although somewhat difficult to describe in words, a simple diagram easily illustrates the concept:

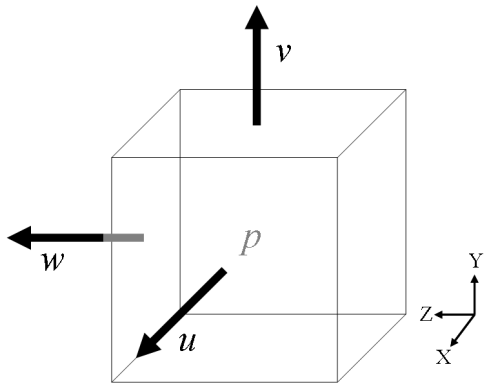

Figure 2.3. An illustration of one finite volume (cell) in the staggered Cartesian mesh. The velocities in the streamwise, vertical, and spanwise directions are u,v, and w, respectively. The pressure, stored as the center of the cell, is p.

A Cartesian mesh such as this one is advantageous in that it allows for a very simple indexing scheme. If we take i to be the index location in the streamwise (X) direction, j to be the index location in the vertical (Y) direction, and k to be the index in the spanwise (Z) direction, we can formulate a general way to determine the index of neighboring cells in any direction.

The mesh stores each velocity at a cell "face". The streamwise velocity u_i is stored on the right face of the cell, as seen in Figure 2.3. The vertical velocity v_i is stored on the top face, and the spanwise velocity w_i is stored on the front face. The pressure

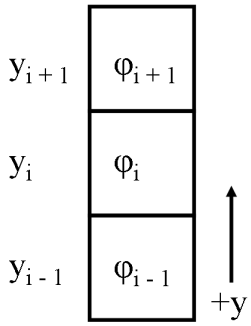

Figure 2.4. A two-dimensional example of the "i+ i-" scheme employed in the code for tracking indices of quantities stored at various cell locations.

p_i, which is a scalar quantity and thus has no directional dependence, is stored in the center of the cell. This method allows for the spatial discretization discussed in the previous section.

2.4 Initial and Boundary Conditions

2.4.1 Initial Conditions

Before boundary conditions are covered in more detail, the topic of initial conditions will be introduced. Up to this point, initial conditions have not been examined due to their abstraction from the physical problem at hand. In order to produce a successful simulation of turbulent channel flow, the CFD code must be seeded with proper initial conditions. The state of these initial conditions can dictate factors such as the amount of time the simulation takes to reach steady state, the development of the turbulent energy cascade, and the presence of the proper turbulent structures at all relevant length scales.

Turbulence is characterized by many factors, two of which are the Reynolds number corresponding to the flow, and the Reynolds stresses within the flow, which are a measure of the shear and normal forces experienced within the fluid (see section 2.5.3, Appendix B, and [41] for more details). Turbulent channel flow is no different,

and there are several ways to determine whether or not a simulation has produced "correct" turbulent channel flow. This research used previous work by Kim [23] and Moser [29] as a means of benchmarking the code (discussed in Chapter 3). Attempting to reproduce the results of Kim and Moser (who studied turbulent channel flow using DNS) implied matching their Reynolds number (in this case, the *friction* Reynolds number, Re_τ, based on the *friction velocity* $\boldsymbol{u}_\tau$), which in turn implied a certain *pressure drop* across the channel, as the *friction velocity* $\boldsymbol{u}_\tau$ can be related to the pressure drop for fully developed channel flow by:

$$\boldsymbol{u}_\tau = \left(-\frac{\delta}{\rho} \frac{dp_w}{dx} \right)^{\frac{1}{2}} \tag{2.9}$$

where δ is defined as the channel half-height, ρ is the fluid density, and $\frac{dp_w}{dx}$ is the change in pressure in the x direction, which in in this case is the streamwise direction. p_w is the mean pressure at the bottom wall, as defined in [41]. Briefly, an *ensemble* average can be thought of as the average of a variable, perhaps the pressure p, over a certain number of repetitions.

$$\langle p \rangle_N \equiv \frac{1}{N} \sum_{n=1}^{N} p^n \tag{2.10}$$

In the channel flow case, the mean streamwise pressure gradient is uniform across the flow, thus

$$\frac{\partial \langle p \rangle}{\partial x} = \frac{dp_w}{dx} = \frac{dp}{dx} \tag{2.11}$$

Considering $\frac{\partial \langle p \rangle}{\partial x}$ is a fixed constant for any given simulation, the means of averaging is not important at this time. The difference between ensemble and spatial averaging will be considered in Section 2.5.1.

In order to match the results of Kim and Moser, it was necessary to impose the proper pressure gradient on the simulations. The need to apply a large pressure gradient to the channel simulation is problematic. If one were to start with quiescent

flow (i.e. $\boldsymbol{u} = 0$) and suddenly impose the proper $\frac{dp}{dx}$, the simulation would quickly become unstable and crash (for a deeper discussion of stability, see [5]). In addition, if one were to start the simulation with fully developed laminar channel flow and then suddenly increase $\frac{dp}{dx}$ to the required value, again the code would become unstable and crash unless a very small time step were used. One solution to this problem is hinted at in the previous sentence: rather than applying the large $\frac{dp}{dx}$ *at once*, one could increase the pressure gradient *gradually*, until the necessary $\frac{dp}{dx}$ is attained. Although avoiding the initial stability problem, this solution creates two other problems. First and foremost, as $\frac{dp}{dx}$ is increased and eventually reaches the target value, the velocity in the streamwise direction will grow very large (because the flow is still laminar), and will continue to grow once the pressure gradient has been fixed. These extremely large velocity values necessitate an extremely small time step in order to maintain stability, and will result in a simulation that requires a very long time to reach steady state. The second problem involves the nature of the extremely fast channel flow: if one were to calculate the Reynolds number based off of the mean velocity, one would discover that it was very high. Further investigation of this flow would reveal that the flow was, in fact, still laminar, despite having a Reynolds number that is well above the critical Reynolds number. This "super laminar" flow will have a parabolic profile, will not exhibit the sort of energy cascade that is expected in a turbulent flow, and will have a Reynolds number (based off of the mean velocity, not $\mathbf{u}_\tau$) that is in fact *higher* than the target mean Reynolds number. Despite having the proper boundary conditions and $\frac{dp}{dx}$, the simulation has not yet become unstable or turbulent. Although describing the mechanics of turbulent transition is beyond the scope of this research, a simple example can illustrate the basic problem. In order for a laminar flow to become turbulent, many conditions, such as the Reynolds number of the flow, must be correct. A laminar flow with a Reynolds number high enough to become turbulent takes time to develop turbulent vortices and establish a turbulent energy

cascade. It is important to note that the statement claiming the flow will never be perturbed into turbulence in not entirely true. As with any numerical scheme, DNS will accumulate round off error as it progresses. This round off error will eventually cause a great enough perturbation in the flow to initiate instability, but it may take an enormous amount of time, as a typical round off error may have to grow from order 10^{-12} to order 10^{-2} to affect a large enough disturbance. In the physical world, this perturbation may come from something as simple as surface roughness, an object in the flow, or a sudden change in the physical conditions the flow is subject to.

With these problems in mind, a hybrid solution must be employed. First, the necessary $\frac{dp}{dx}$ must be approached gradually to ensure stability. Second, the simulation must be seeded with an initial velocity field that has the ability to perturb the flow field such that it rapidly becomes turbulent. Finding a proper initial velocity field to rapidly initiate an energy cascade is not a trivial task, as is discussed in [31] as well as many other sources. Again, the development of proper turbulent initial conditions is beyond the scope of this work. Briefly, these fields must contain certain characteristics, such as flow structures and energy levels at a variety of time and length scales. For this work, proper turbulent initial condition velocity fields were provided by [13] and [31]. The simulations were seeded with isotropic turbulent initial condition superimposed on a modified laminar velocity profile. This modified profile was created by generating the "super laminar" profile associated with the large pressure gradient needed for the simulation, then truncating this profile by eliminating all velocities that were above the expected maximum velocity in the turbulent field.

This method was employed once, to generate the first fields corresponding to $Re_\tau \approx 180$. The initial conditions for both the $Re_\tau \approx 395$ and $Re_\tau \approx 590$ cases were generated by interpolating the existing steady $Re_\tau \approx 180$ and $Re_\tau \approx 395$ fields, respectively, to the new, higher resolution, and lowering the viscosity such that the de-

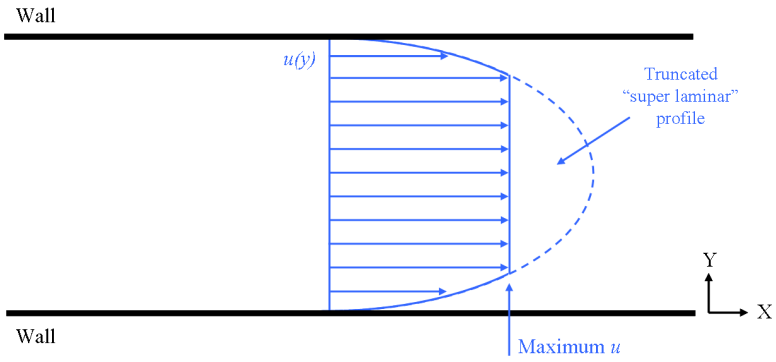

Figure 2.5. Schematic of the truncated "super-laminar" profile.

sired streamwise shear velocity at the wall, u_τ, would be attained once the simulation reached steady state.

2.4.2 Periodic Boundary Conditions

The code utilizes periodic boundary conditions in the streamwise and spanwise directions, and places "walls" at two locations in the vertical direction (to be discussed in 2.4.3). A more detailed look at the theory and implementation of these boundary conditions can be found in [17] (specifically, Chapter 4, and Appendix C in [17]). Periodic boundary conditions existed in all three directions in the original code. In essence, when applied to a domain in a particular direction, a periodic boundary condition will take velocities and pressures exiting the domain in that direction, and apply them to the entrance of the domain. For example, all of the velocity and pressure information at the *exit* of the channel in the streamwise direction will be applied to the *entrance* of the channel, essentially creating a loop between the entrance and exit. The boundary conditions work identically for the spanwise direction. With these boundary conditions present in the streamwise and spanwise direction, the "top and bottom walls" of the channel become flat plates, extending infinitely in both directions.

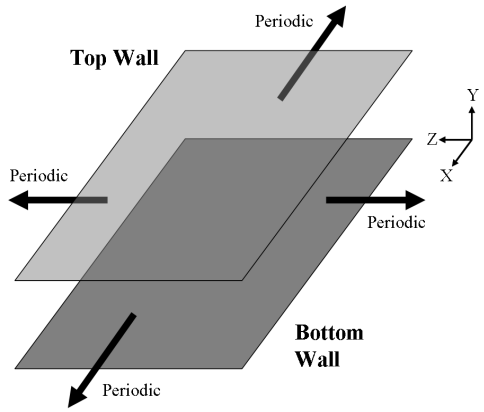

Figure 2.6. A representation of the "channel", which is in fact two parallel infinite plates, extending in the streamwise (X) and spanwise (Z) directions. Note these plates represent the "walls" of the channel discussed previously.

The arrangement shown in Figure 2.6 is not a "channel" in the traditional sense, but is in fact flow between two infinite parallel plates. This is the desired physical situation to be simulated, as it does not present problems such as entrance or edge effects. Furthermore, most of the work done simulating turbulent "channel" flow is in fact simulating turbulent flow between two parallel infinite plates, including the work done by Kim and Moser. These periodic boundary conditions were used in conjunction with the walls in the vertical direction to simulate the behavior of a superhydrophobic surface.

2.4.3 Walls

Initial testing and benchmarking of the DNS code for both laminar and turbulent flows required "smooth wall" boundary conditions to be employed. The term "smooth wall" is used by the author to differentiate between these boundary conditions and those of superhydrophobic surfaces, discussed in the next section. A smooth wall boundary condition is one which is entirely no-slip, and does not have any pattern of shear-free regions. The no-slip boundary condition was mentioned in Chapter One.

In general, a no-slip boundary condition sets the streamwise and transverse velocities, u and w, respectively, equal to zero at the wall.

$$\begin{aligned} u_{wall} &= 0 \\ w_{wall} &= 0 \end{aligned} \tag{2.12}$$

In addition, the wall imposes a *no penetration* condition on the velocity component normal to it, in this case the vertical velocity v:

$$v_{wall} = 0 \tag{2.13}$$

Formally, there is no boundary condition on the pressure field. Numerically, it appears as if the boundary condition

$$\left(\frac{\partial p}{\partial y}\right)_{wall} = 0 \tag{2.14}$$

is applied to the pressure Poisson equation, where y is the vertical direction. One way to implement these boundary conditions in the staggered mesh scheme is to employ "ghost cells", which are extra cells, outside of the regular computational domain, used to implement both the no-slip and periodic boundary conditions.

Figure 2.7 shows the arrangement of the staggered Cartesian mesh at a wall. Note that the streamwise and spanwise velocity information, as well as the pressure information (p) do not lie at the walls themselves, thus the boundary conditions present above cannot be applied directly, except in the case of the vertical velocity v, which can be set identically to zero at the walls. The pressure boundary condition is implemented by setting the pressure "below" the wall (in the ghost cell) equal to the pressure "above" the wall (at the first interior cell). This will effectively set the spatial derivative of the pressure in the vertical direction equal to zero, thus fulfilling the

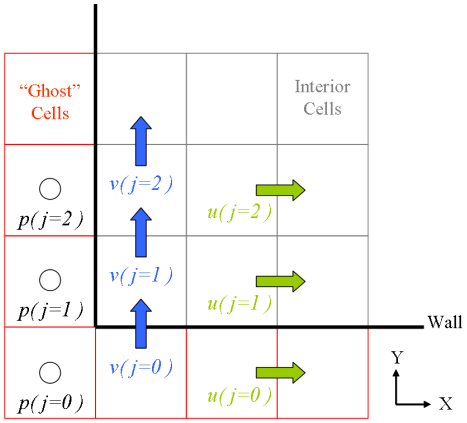

Figure 2.7. A representation of the "ghost cell" scheme in the staggered Cartesian mesh. These cells (colored red), shown here in only two directions for clarity, in fact exist on all six sides of the domain. Note the locations of the velocity and pressure.

"boundary condition" for pressure. Handling the streamwise and transverse velocity boundary conditions requires a more clever approach. Like the pressure, the staggered mesh only allows the *change* in these values *across* the wall to be set, and not the value at the wall itself. Unlike the pressure, these velocities must be set equal to a specific value (zero) at the walls. To do this, the velocity "below" the wall (in the ghost cell) is set to be equal and opposite to that value which is "above" the wall. If the velocity is assumed to vary linearly between these two locations, then the value of the velocity at the wall (which is located halfway between the ghost and inner cells) will be equal to zero. This method is employed for both the streamwise and transverse velocities.

In addition to no-slip walls, the DNS code was also tested with no-shear walls, which can be thought of as an approximation to a "free surface" with no deformation. The boundary conditions for the normal (vertical) velocity and pressure are identical to those for a no-slip wall: the boundary condition does not allow penetration and cannot support a pressure difference. Unlike the no-slip condition, the no-shear condition sets the streamwise and spanwise *shear* equal to zero at the wall.

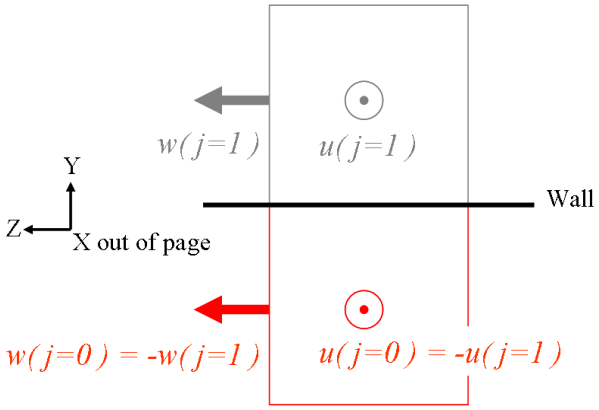

Figure 2.8. Handling the streamwise and transverse velocities at the wall. Note that positive X and u are facing out of the page.

$$\left(\frac{\partial u}{\partial y}\right)_{wall} = 0$$
$$\left(\frac{\partial w}{\partial y}\right)_{wall} = 0 \tag{2.15}$$

Similar to the no-slip case, this as achieved by forcing u and w "below" the wall (in the ghost cell) to be identically equal to u and w "above" the wall, thus forcing the spatial derivative of u and w to zero. The no-slip and no-shear boundary conditions, in the form presented above, are used in combination to implement the superhydrophobic boundary conditions of interest.

2.4.4 Posts and Ridges

The topic of boundary conditions for superhydrophobic surfaces was introduced in Chapter One. Recalling this discussion, note that locally, the proper boundary conditions to apply for such a surface include regions of no-slip and regions of no-shear, corresponding to the locations of the microfeatures (no-slip) and the fluid-gas interface supported between those microfeatures (no-shear), respectively.

Implementation of ridges and posts involves identifying the appropriate portions of the wall to apply no-slip and no-shear boundary conditions. For example, to simulate a periodic array of streamwise ridges whose width and spacing (in the spanwise direction) are equal, repeating boundary conditions of no-slip and no-shear would be applied in the spanwise direction; this pattern would be uniform in the streamwise direction.

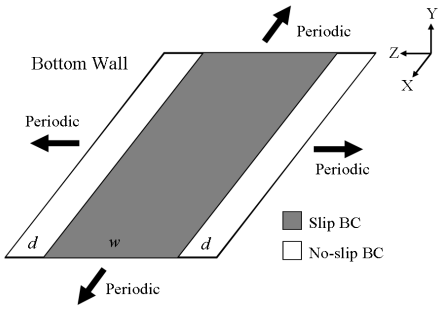

(a) A single streamwise ridge of width d and spacing w. This represents the "minimal periodic unit" of a periodic array of ridges.

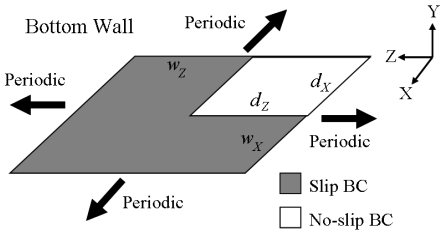

(b) A single post of width d_Z and spacing w_Z in Z, and width d_X and spacing w_X in X. This represents the "minimal periodic unit" of a periodic array of posts.

Figure 2.9. Examples of ridges and posts as presented in the code. Note that these boundary conditions are two dimensional.

It is important to make clear the fact that the ridges and posts affect the fluid at the boundary of the channel. Their effect on the fluid is two dimensional, and we do not need to calculate the height of the microfeatures. The same is true for the interface supported between the ridges and posts: their surface is assumed to be two dimensional, which implies that no deflection occurs. In reality (as shown in Chapter One), the interfaces do in fact deflect. The assumption of zero surface deflection was made for the sake of time and simplicity. It is possible to perform these simulations allowing the interface supported by the microfeatures to deflect, and this may be the subject of future research. Implementation of the posts and ridges in the CFD code is complicated by the staggered mesh. Different velocities are stored at different locations, which makes it difficult to create a post (for example) which appears to be

the same size for streamwise and spanwise velocities, and which appears to be square. Figure 2.10 illustrates this difficulty.

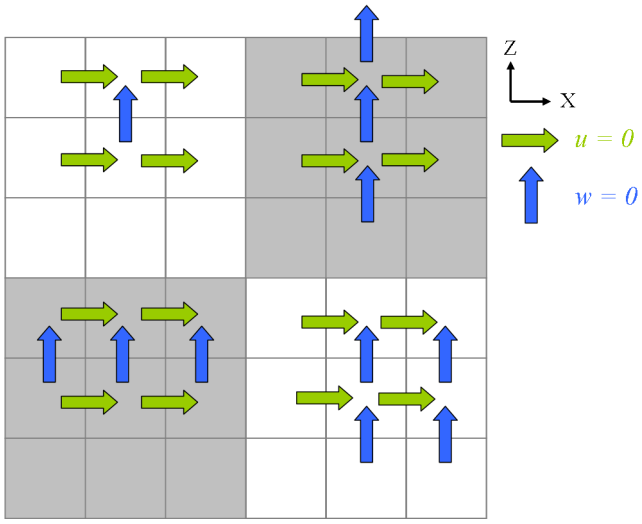

Figure 2.10. The staggered mesh presents difficulty when attempting to place boundary conditions in the proper location, especially in the case of posts, which are "seen" differently by u and w. Four possible post arrangements are shown above.

There is no "standard" way to handle this problem, thus a logical method was adopted and used consistently. As an example, consider a post whose length in the streamwise direction is equal to its width in the spanwise direction. Physically, this post (or, more precisely, the two dimensional boundary condition representing this post) would be a square, lying in the plane of the wall. The staggered mesh, however, will not admit a square geometry for both the u and w velocities. As such, the boundary conditions (in this case, no-slip) must be assigned to streamwise and transverse velocities locations such that they closely approximate a square, as shown in Figure 2.11.

The scheme presented in Figure 2.11 is one which most closely approximates a ridge and a post in the staggered mesh, with each feature occupying an arbitrary number of cells, in this case two in the spanwise direction (for the ridge) and two in both the spanwise and streamwise direction (for the post). Depending on the physical

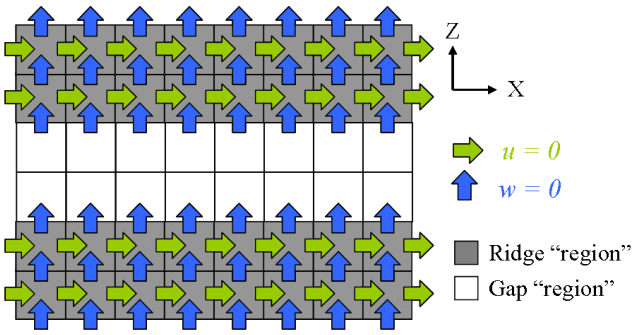

(a) Locations of no-slip boundary condition assignments for a typical ridge.

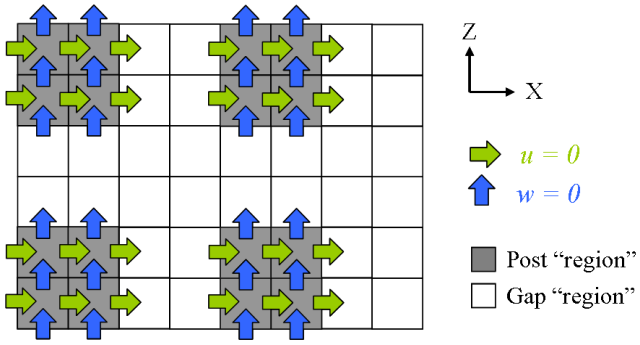

(b) Locations of no-slip boundary condition assignments for a typical post.

Figure 2.11. Examples of velocity boundary conditions for ridges and posts.

size of the domain, the physical size of the features being studied, and the resolution of the simulation, the number of cells occupied may range from four upward to sizes on the order of the subdomain or domain being considered. The more cells a feature includes, the less distortion occurs due to the staggered mesh.

The CFD code makes decisions about ridge and post placement based upon user input and the standard for boundary condition location assignment presented above. Post widths, and ridge widths and lengths, cannot exceed the domain size in the event of a serial (one processor) simulation, or subdomain size if a parallel simulation is being performed. This limitation, combined with upper limits on the overall domain

resolution, does limit the range of microfeature sizes and geometric proportions that the CFD code is capable of simulating.

2.4.5 Parallel Considerations

The DNS code is parallelized and designed to be run on supercomputer clusters. For a much more in-depth look at the parallelization techniques employed in the CFD code, see [17]. When a parallel job is performed, the overall domain is split into several smaller subdomains. Due to the nature of the simulation, the domain is only divided in the streamwise (X) and spanwise (Z) directions where it is split amongst the processors or cores.

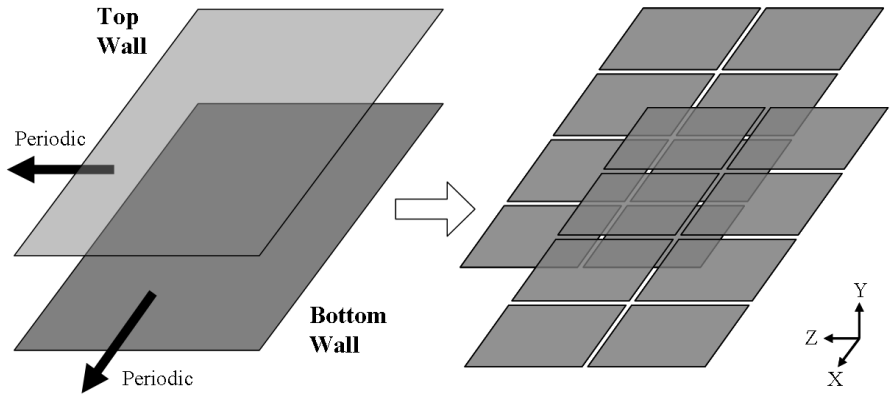

Figure 2.12. An example of a domain split into eight subdomains, which could be run on eight separate processors.

Partitioning the domain into subdomains results in the surface microfeatures being partitioned as well. If this partitioning is not performed carefully, microfeatures may not be separated along lines of symmetry, which would result in each subdomain having imperfect periodicity. As such, the boundary conditions are actually applied to each subdomain, and the dimensions of the ridges and posts are checked against the dimensions of the subdomain.

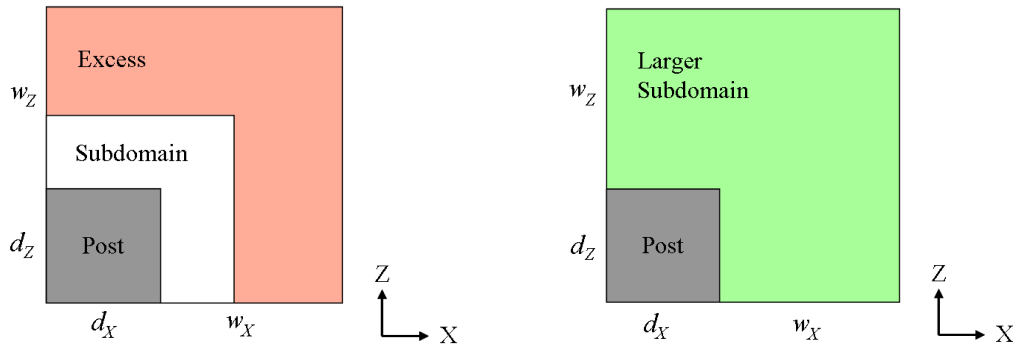

(a) A subdomain that does not fulfill the periodicity requirements. The sum of d_Z and w_Z is greater than the subdomain region (the "excess" shown in red), as is the sum of d_X and w_X.

(b) The proper post boundary condition implementation for this example subdomain, which could be achieved by increasing the subdomain size or decreasing the feature size.

Figure 2.13. Periodicity requirements are a function of subdomain resolution and feature size.

If the combination of the user-input feature dimension and feature spacing is incompatible with the specified subdomain dimensions, the code will prevent the simulation from beginning. This method is necessary to allow the domain to be partitioned into identical subdomains. The current implementation of the superhydrophobic boundary conditions restricts the size and spacing of the features to those which will result in periodic subdomains, and this restricts the feature size to be less than or equal to the subdomain size. This is acceptable, considering current research does not require simulating large feature sizes or spacings. The allowable feature size is directly dependent upon the resolution of the simulation in the streamwise and spanwise directions.

2.5 Post Processing

2.5.1 Spatial and Temporal Averaging

The DNS code is only as good as the results it produces. Being able to quickly and accurately collect and analyze those results is key to a successful simulation. To

facilitate this, once the code has resolved the full velocity and pressure fields, these velocity and pressure fields, along with several statistics calculated from the fields, are stored, and temporally averaged over the entire duration of the simulation. Collecting temporally averaged statistics is necessary for turbulent flows as any instantaneous data will be extremely noisy, making it difficult to identify trends. These fields are, however, useful for turbulent structure identification, covered in Chapter 5 Section 5.2. Additionally, results reported from DNS of turbulent flows are often temporally and spatially averaged if the flow is statistically stationary (in the case of temporal averaging) or homogeneous (in the case of spatial averaging). Also, current theory about turbulent flows predicts only average behavior. Before the discussion of post processing proceeds, the topics of temporal, ensemble, and planar averaging must be addressed. All three forms of statistical averaging are performed on the velocity and pressure fields, and understanding their differences is akin to understanding both the post processing techniques employed, and the results presented.

Temporal averaging of a variable, for example the velocity u, is necessary to obtain smooth and statistically relevant results. At certain time steps (referred to as sample times, whose interval is controlled by the user), the entire field u_s (at some sample time s) is added to u_{s-1}, the field saved from the previous sample time. A counter keeps track of the number of samples taken, N_s. The *temporal* average of u takes the array of u_s, summed over N_s sample times, and divides by N_s. A temporally averaged field is denoted by $\bar{u}^t$. Ensemble averaging is defined in Equation 2.10. In this case, it is performed by adding all fields from each *subdomain*, and dividing by the number of subdomains present. The ensemble average of some field u is denoted $\langle u \rangle$. Finally, a planar average, which is employed in the calculation of quantities such as the velocity profiles and Reynolds stresses, is written as $\bar{u}^{PQ}$, where the superscript PQ indicated the two Cartesian directions in which the planar average has been performed. Nearly all results presented come from fields which have temporal, ensemble, and planar

averaging performed on them. For the variable u averaged in the XZ plane (thus a function only of Y), this is written as $\overline{\langle \bar{u}^t \rangle}^{XZ}$.

Each subdomain produces its own set of temporally averaged data. Once the simulation has completed, this data is read into a separate post processing program, which was developed for this purpose. The temporally averaged information from each subdomain is ensemble averaged with all other subdomain information, resulting in a set of data which is fairly smooth. Performing the ensemble average over every subdomain is valid as each subdomain is of the same dimensions, and has the same boundary conditions, with the microfeatures in identical locations. Although the turbulent structures will change from subdomain to subdomain, the average velocity correlations and turbulent energy cascade will be identical for all subdomains.

It is important to note an issue which arises from the presence of varying slip and no-slip boundary conditions. The previous discussion of slip lengths and slip velocities alluded to this problem, when describing the difference between the global or macroscopic affect of the superhydrophobic surfaces, and the local or microscopic behavior. If, for example, one were to perform a planar velocity average in the streamwise direction along a wall with varying slip and no slip, one would arrive at the *average* effect the features produces, rather than the effect of any one specific region. This comes from the averaging of regions where the streamwise and transverse velocity components are zero (over the microfeatures) and regions where those velocities experience no resistance, and have some non-zero value. This type of planar averaging produces the results that an engineer is likely to observe, as the micro-scale variations are smaller than the typical scales of interest.

2.5.2 Handling the Non-Uniform Grid

Performing proper averaging in a non-uniform mesh is not difficult, but requires special attention be paid to the methods employed for spatial averaging, and in par-

ticular volume weighted integrals. When dealing with a Cartesian mesh, planar and volume averages are often computed by a simple summation and division. For example, if one desired the volume average of streamwise velocity over the entire computational domain, the velocities from each cell in the domain could be summed, and that sum divided by the total number of cells in the domain. This method is acceptable assuming each cell is of equal volume, but produces erroneous results when a non-uniform mesh is employed. If each cell volume is assumed to be identical, then the cell volumes near the center of the domain will be underestimated, while the cell volumes near the walls of the domain will be grossly over estimated. Thus planar averaged velocities at the center of the channel will be lower than the actual average, while the planar average velocities near the walls will be much greater than the true average. The solution to this problem is simple, namely to perform proper integration rather than use the sum and divide shortcut. The proper integration must take into account the varying volumes of the cells, therefore it must have access to information about grid nonuniformity. This is the method employed both in the DNS code and in the post processing software developed to process the data fields.

2.5.3 Reynolds Stresses

The majority of the results presented by Kim [23] and Moser [29] are in the form of Reynolds stresses. A detailed discussion of Reynolds stresses can be found in [41], and a brief description in Appendix B. Examples of these results can be found in Chapter Three. Reynolds stresses are components of the *Reynolds stress tensor*, $R_{ij} \equiv \left\langle \overline{u_i' u_j'}^t \right\rangle$:

$$\begin{bmatrix} \langle \overline{u'^2}^t \rangle & \langle \overline{v'u'}^t \rangle & \langle \overline{w'u'}^t \rangle \\ \langle \overline{u'v'}^t \rangle & \langle \overline{v'^2}^t \rangle & \langle \overline{w'v'}^t \rangle \\ \langle \overline{u'w'}^t \rangle & \langle \overline{v'w'}^t \rangle & \langle \overline{w'^2}^t \rangle \end{bmatrix}$$

Note that the tensor is symmetric, and involves the fluctuating component of the velocities, namely u', v' and w'. It is important to understand the difference between

the velocities used in the Reynolds stress tensor and the common interpretation of the velocities. The velocities used in the stress tensor are the *fluctuating components* of the velocities at every point in the simulation. They are calculated by taking the velocity at every point, say $\boldsymbol{u(x,t)}$, and subtracting the temporal and ensemble averaged velocity $\langle \overline{\boldsymbol{u}}^t \rangle$, resulting in the *fluctuating component* of the velocity at that point, $\boldsymbol{u}'(\boldsymbol{x})$, which is then used in the Reynolds stress tensor. Note that the temporal averaging is not required, but is used in this work to reduce the number of ensemble averages required.

$$\begin{aligned} u'(x,y,z,t) &= u(x,y,z,t) - \langle \overline{u}^t(x,y,z) \rangle \\ v'(x,y,z,t) &= v(x,y,z,t) - \langle \overline{v}^t(x,y,z) \rangle \\ w'(x,y,z,t) &= w(x,y,z,t) - \langle \overline{w}^t(x,y,z) \rangle \end{aligned} \tag{2.16}$$

The six components of the stress tensor are calculated, and averaged both temporally and over ensembles. The turbulent kinetic energy is simply one half the trace of the tensor:

$$K(\mathbf{x}) \equiv \frac{1}{2}\left[\langle \overline{u'^2}^t \rangle + \langle \overline{v'^2}^t \rangle + \langle \overline{w'^2}^t \rangle\right] = \frac{1}{2} R_{ii} \tag{2.17}$$

In addition, planar averages of these seven quantities are calculated at each vertical location (Y), to represent the components of the stress tensor as they vary from the bottom to the top wall of the channel, presenting the data on a scale most interesting to engineers. Due to the aforementioned storage limitations, the code employs a unique Reynolds stress calculation scheme. At every time step, the code stores and calculates the temporal average of a tensor M_{ij}.

$$
\begin{aligned}
M_{ij} &\equiv \overline{\left(\langle \bar{u}^t \rangle + u'\right)_i \left(\langle \bar{u}^t \rangle + u'\right)_j}^t \\
&= \overline{\langle \bar{u}_i{}^t \rangle \langle \bar{u}_j{}^t \rangle}^t + \overline{\langle \bar{u}_i{}^t \rangle u'_j}^t + \overline{u'_i \langle \bar{u}_j{}^t \rangle}^t + \overline{u'_i u'_j}^t \\
&= \overline{\langle \bar{u}_i{}^t \rangle \langle \bar{u}_j{}^t \rangle}^t + \overline{u'_i u'_j}^t \\
&= \langle \bar{u}_i{}^t \rangle \langle \bar{u}_j{}^t \rangle + R_{ij}
\end{aligned}
\tag{2.18}
$$

as $\overline{u'_i \langle u_j \rangle}^t = \overline{u'_i \langle u_j \rangle}^t = 0$ and averaging an average quantity has no effect [41]. In order to calculate R_{ij}, the code simply subtracts $\langle \bar{u}_i{}^t \rangle \langle \bar{u}_j{}^t \rangle$ from M_{ij}

$$
R_{ij} = M_{ij} - \langle \bar{u}_i{}^t \rangle \langle \bar{u}_j{}^t \rangle \tag{2.19}
$$

which results in $\overline{u'_i u'_j}^t$, the standard definition for the temporally averaged Reynolds stress tensor. This is then ensemble averaged $\left\langle \overline{u'_i u'_j}^t \right\rangle$ to obtain even smoother statistics.

CHAPTER 3

CODE VALIDATION

3.1 Background

The Navier Stokes equations admit very few analytical solutions. Most of the closed form solutions that do exist involve simplifications of the equation based on geometry, flow conditions, incompressibility, or scaling arguments. These facts necessitate the use of numerical solution methods, including direct numerical simulation, which is employed for current research. In addition, the nature of the Navier Stokes equations makes it difficult to validate the solutions returned by a numerical simulation, especially in the case of turbulent flows.

In order to trust the solutions returned by the DNS code, it was necessary to compare the results of certain simulations to known solutions. In the laminar regime, the choice of flow conditions to benchmark against was obvious: fully developed laminar flow, with a known pressure gradient, between two no-slip, infinite parallel plates admits an exact solution, referred to as Poiseuille flow (between two plates). The availability of additional boundary conditions in the code allowed two other laminar flows to be tested, namely flow between one fixed and one moving no slip, infinite parallel plate (planar Couette flow, which is *not* driven by a pressure gradient), and pressure driven flow over one infinite plate, with a no-shear ("free") surface as the second, upper boundary condition. Couette flow, and flow over a plate with a free surface, both have analytical solutions. Work originally done by Philip [39, 40], and furthered by Lauga and Stone [24], derived analytical solutions for laminar, pressure driven flow over mixed slip and no-slip boundary conditions, similar (and, in

some cases, identical) to the boundary conditions used to simulate superhydrophobic surfaces. The availability of these solutions not only allowed for further laminar validation to occur, but also provided a means of testing the mixed boundary conditions implimented in the code. For these flows, velocity profiles were used as a means of comparison.

The solutions presented above are steady state and do not provide a way of analyzing the code's ability to predict the transient behavior of velocities or pressures, which is key in turbulent flows. As such, an analytical solution to the Navier-Stokes equations was required that would predict both the transient and steady state solutions for a flow. There are several such solutions (all in the laminar regime), including the two dimensional Taylor vortex decay, which was used to test the code's transient solution capabilities. For these solutions, velocity and pressure decay rates and magnitudes were used as a means of comparison. Finally, the code was validated against previous numerical results for pressure driven turbulent flow between two no slip, infinite parallel plates, performed at various Reynolds numbers by Kim, Moin, and Moser [23, 29]. Here, Reynolds numbers, bulk mean velocities, skin friction coefficients, velocity profiles, and Reynolds stresses were used as means of comparison.

3.2 Laminar Regime

3.2.1 Poiseuille Flow Between Two Plates

The analytical solution to the Navier Stokes equations for steady Poiseuille flow between two infinite plates, adapted from [47]:

$$u(y) = -\frac{(\delta)^2}{2\mu}\frac{\partial p}{\partial x}\left[1 - \left(\frac{y}{\delta}\right)^2\right] \tag{3.1}$$

Table 3.1. Line and symbol key for laminar results. Note that these conventions do not apply to the H/w results presented in Chapter 4.

Line Type	Description	Applies to
——	Simulation U_{bulk} profile - No-Slip	[24], Poiseuille, Half-Channel
– – –	Simulation U_{bulk} profile - Slip	"
·-·-·-·-	Simulation velocity trend	Taylor Vortex Decay
– ·· –	Simulation pressure trend	"

Symbol Type	Description	Applies to
□	Analytical U_{bulk} profile - No-Slip	[24], Poiseuille, Half-Channel
△	Analytical U_{bulk} profile - Slip	"
◇	Analytical velocity trend	Taylor Vortex Decay
▽	Analytical pressure trend	"

where *u(y)* is the streamwise velocity (as a function of vertical position only, making this a one dimensional solution), x is the streamwise direction and y the vertical direction, $\frac{\partial p}{\partial x}$ is the known pressure drop down the streamwise direction of the channel, μ is the viscosity of the fluid, and δ is the channel half-height. Results from the CFD code matched closely (to machine precision) with those obtained from the analytical solution. Figure 3.1 compares the velocity profiles for matching pressure drop, viscosity, and channel geometry.

3.2.2 Couette Flow Between Two Plates

The analytical solution to the Navier Stokes equations for steady Couette flow between two infinite plates, one of which is moving at constant velocity U, adapted from [47]:

$$u(y) = U\left[1 - \frac{(2\delta)^2}{2\mu U}\cdot\frac{\partial p}{\partial x}\left(1 - \frac{y}{2\delta}\right)\right]\left(\frac{y}{2\delta}\right) \tag{3.2}$$

with the same quantities defined for Equation 3.1. For code validation, $\frac{\partial p}{\partial x} = 0$, reducing Equation 3.2 to

$$u(y) = U\frac{y}{2\delta} \tag{3.3}$$

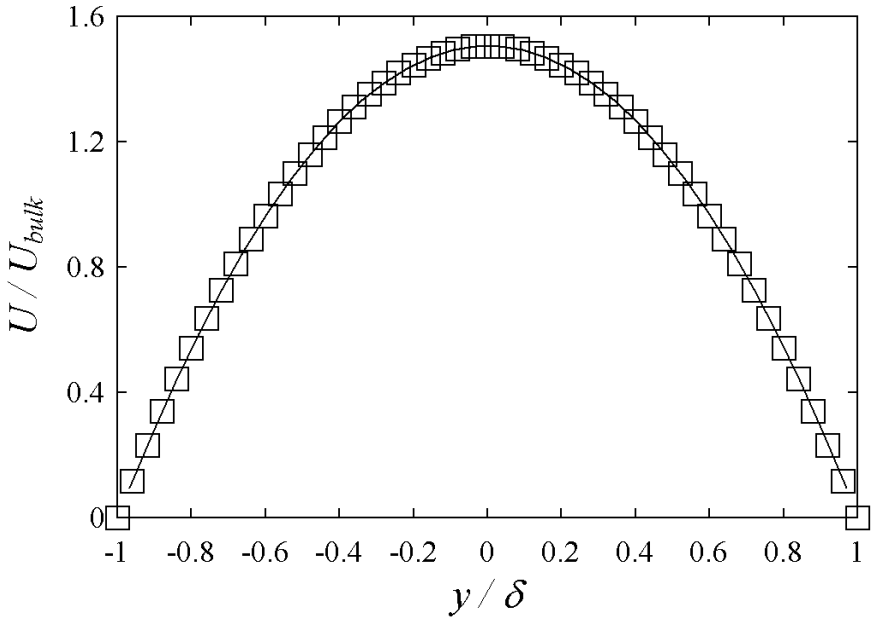

Figure 3.1. A comparison of velocity profiles scaled by the bulk velocity, obtained from the laminar analytical solution (□) and the CFD code (–) for Poiseuille flow between two infinite parallel plates.

which is a linear function in the vertical direction y. Geometry is similar to that of Poiseuille flow between infinite parallel plates, with the exception that there is no pressure gradient and the top plane has a constant velocity. Results from the CFD code matched the analytical solution to machine precision.

3.2.3 Free Surface Flow Over a Plate

The analytical solution to pressure driven flow over a flat plate with the upper boundary condition being a free surface is identical to Poiseuille flow through a channel (see Equation 3.1) where the channel height is twice that of the Poiseuille channel.

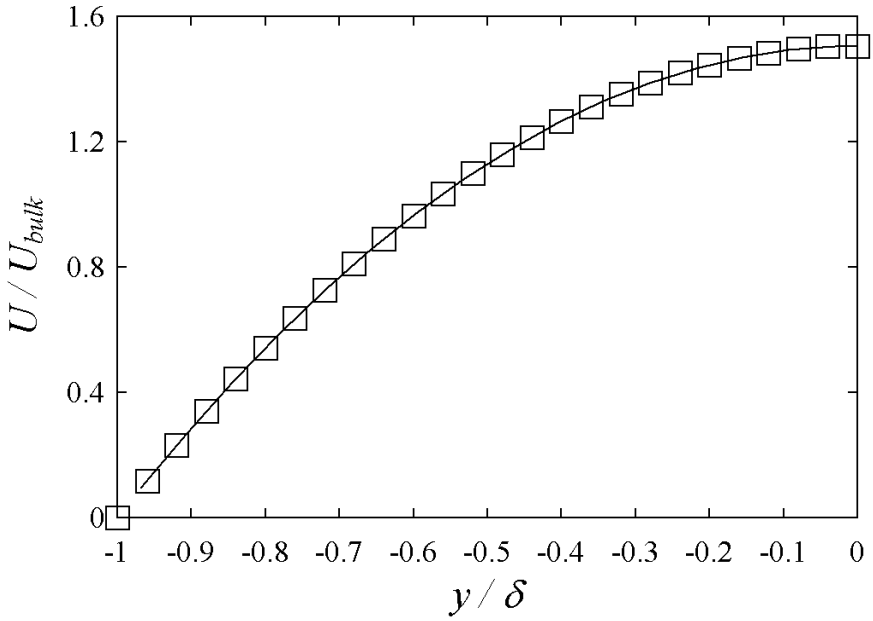

Figure 3.2. A comparison of velocity profiles scaled by the bulk velocity, obtained from the analytical laminar solution (□) and the CFD code (–) for the simulated "half channel".

3.2.4 Solutions by Philip, Lauga, and Stone

Philip [39, 40] derived analytical solutions to the Navier Stokes equations for Stokes flow over mixed no-slip and no-shear boundary conditions. These included (1)

shear flow over a plate with one streamwise no-shear band (which is referred to as a gap in this research), (2) the same flow as (1) with a regular array of no-shear bands in the bottom plate, (3) Poiseuille flow between two infinite parallel plates with a single streamwise no-shear band in the bottom plate, and (4) the same flow as (3) with a regular array of no-shear bands in the bottom plate. These flow conditions were simulated and compared with the forms of Philip's solutions presented by Lauga and Stone [24]. For the solutions presented here, X represents the streamwise direction, Y the vertical direction, and Z the spanwise direction. u_x is the velocity in the streamwise direction, i represents an imaginary number, τ_∞ represents the constant shear stress far from the plate, h represents the gap width, H represents the shear-free band spacing (which only applies to regular arrays of bands), μ represents the fluid viscosity, D represents the spacing of the plates (for the cases with flow between two plates, and U_0 represents the velocity of the upper plate (in the case of shear flow). In addition, $\frac{\partial p}{\partial x}$ represents the constant pressure gradient for the case with Poiseuille flow. The analytical solution for shear flow over a single shear-free band (gap), from [24].

$$u_x(y,z) = \frac{\tau_\infty H}{\mu}\left[\frac{y}{H} + \mathrm{Im}\left[\left(\left(\frac{z+iy}{h}\right)^2 - \frac{1}{2}\right)^{\frac{1}{2}} - \frac{z+iy}{h}\right]\right] \tag{3.4}$$

Note that Im(...) indicates that only the imaginary portions of the argument are taken for the solution. The solution for shear flow over an array of shear-free gaps:

$$u_x(y,z) = \frac{\tau_\infty H}{\mu}\left[\frac{y}{H} + \frac{1}{\pi}\mathrm{Im}\left[\cos^{-1}\left(\frac{\cos\left(\pi\frac{z+iy}{H}\right)}{\cos\left(\frac{\pi}{2}\frac{h}{H}\right)}\right) - \pi\frac{z+iy}{H}\right]\right] \tag{3.5}$$

The solution for Poiseuille flow over a single shear-free gap:

$$u_x(y,z) = U_0 D\left[\frac{y}{D} + \frac{2}{\pi}\mathrm{Im}\left(M\right)\right] \tag{3.6}$$

and the analytical solution for Poiseuille flow over an array of shear-free gaps:

$$u_x(y,z) = -\frac{D^2}{2\mu}\frac{\partial p}{\partial x}\left[\frac{y}{D}\left(1-\frac{y}{D}\right)+\frac{2}{\pi}\mathrm{Im}\left(M\right)\right] \tag{3.7}$$

where

$$M = \left[\cosh^{-1}\left(\frac{\cosh\left(\frac{\pi}{2}\frac{z+iy}{D}\right)}{\cosh\left(\frac{\pi}{4}\frac{h}{D}\right)}\right)-\frac{\pi}{2}\frac{z+iy}{D}\right]$$

Due to the complicated nature of Equations 3.4 to 3.7, a separate program was created to produce the solutions associated with the two dimensional analytical solution equation shown above. These results were compared to the DNS.

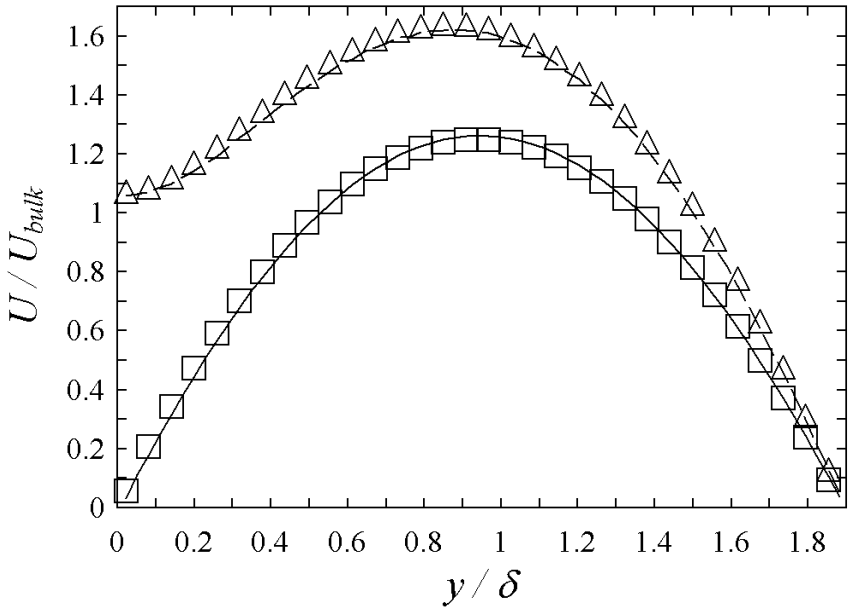

Figure 3.3. A comparison of velocity profiles obtained from the analytical solution (□, △) and the DNS (–) for Poiseuille flow between two infinite parallel plates with a single streamwise no-shear gap in the bottom plate.

As shown in Figure 3.3, simulation results closely matched analytical solutions for the flow conditions investigated. Note the slight discrepancies between the solutions are due to the fact that Philip's solutions have a Reynolds number $Re = 0$, whereas the DNS results have a small but non-zero Reynolds number.

3.2.5 Taylor Vortex Decay

Taylor flow is an incompressible, two dimensional, unsteady, decaying vortex flow which admits an exact solution to the Navier Stokes equations in Cartesian coordinates. The transient solutions for the two velocity components, here u and v, as well as the pressure p are:

$$\begin{aligned} u(x,y,t) &= -\cos\left(\frac{2\pi x}{L_x}\right)\sin\left(\frac{2\pi y}{L_y}\right)e^{\frac{-4\pi^2}{(L_x^2+L_y^2)}\nu t} \\ v(x,y,t) &= \sin\left(\frac{2\pi x}{L_x}\right)\cos\left(\frac{2\pi y}{L_y}\right)e^{\frac{-4\pi^2}{(L_x^2+L_y^2)}\nu t} \\ p(x,y,t) &= -\frac{1}{4}\left[\cos\left(\frac{4\pi x}{L_x}\right)+\cos\left(\frac{4\pi y}{L_y}\right)\right]e^{\frac{-4\pi^2}{(L_x^2+L_y^2)}\nu t} \end{aligned} \tag{3.8}$$

where x and y are the horizontal and vertical positions in the Cartesian coordinate system, L_x and L_y are the domain dimensions in the horizontal and vertical directions, respectively, ν is the kinematic viscosity of the fluid, and t is time. Figure 3.4 shows that the CFD code matched both the magnitude and decay rates of the velocities and pressures predicted by the analytical solution to near-machine precision.

3.3 Turbulent Regime

The process of benchmarking a CFD code for turbulent channel flow is not as straightforward as comparing simulation results to analytical solutions, as was done in the previous section. Instead, results from turbulent channel flow simulations performed by Kim, Moin, Moser and Mansour [23, 29], at various Reynolds numbers were used to benchmark the CFD code. The six components of the Reynolds stress tensor and velocity profiles were compared (see Appendix B for more details). Other results, such as center-line and mean Reynolds numbers, skin friction coefficients, and certain velocity ratios for all Reynolds numbers investigated can be found in Appendix C. Velocity profiles near the wall are presented to better represent the profile's shape

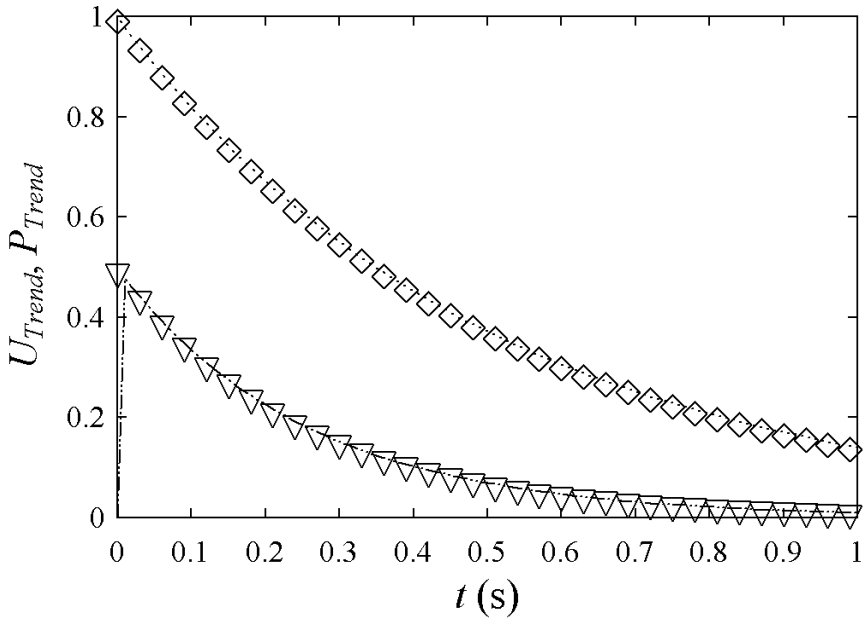

Figure 3.4. A comparison of velocities from the analytical solution (◊) and the CFD code (---), as well as pressures obtained from the analytical solution (▽) and the CFD code (– ·· –) for Taylor vortex showing decay.

very close to the wall. The velocity profiles are also shown with standard scaling to represent the behavior of the profile near the center of the channel. Results from these simulations (performed at $Re_\tau \approx 180$, $Re_\tau \approx 395$, and $Re_\tau \approx 590$) are plotted against a non-dimensional channel height y^+, which is defined in [41].

$$y^+ \equiv \frac{u_\tau y}{\nu} \tag{3.9}$$

where u_τ is the *friction velocity*, calculated from the *wall shear stress* τ_w, both defined in [41]:

$$\begin{aligned} u_\tau &\equiv \left(\frac{\tau_w}{\rho}\right)^{\frac{1}{2}} \\ \frac{\tau_w}{\rho} &\equiv \nu \left(\frac{d\overline{\langle \bar{u}^t \rangle}^{XZ}}{dy}\right)_{wall} \end{aligned} \tag{3.10}$$

where ρ is the fluid density and $\overline{\langle \bar{u}^t \rangle}^{XZ}$ is the temporal and ensemble averaged streamwise velocity at the wall, which is then averaged along the XZ planes corresponding to the bottom and top walls, as described in Subsection 2.5.1. Re_τ is the *friction Reynolds number*, defined as

$$Re_\tau \equiv \frac{u_\tau \delta}{\nu} \tag{3.11}$$

where δ is the channel half height.

Note that by convention, the vertical position (in this case, y or y^+) is plotted on the horizontal axis. The left end of the axis corresponds to the bottom wall of the channel, and the right end corresponds to the center of the channel. For these results, the statistics and profiles are symmetric about the channel's vertical center plane and thus are only presented for one half of the channel. It is important to point out that this assumption of symmetry does not apply to simulations of channels with an SHS, as the SHS boundary conditions are applied only to the bottom wall of the channel. To be consistent with data from [23] and [29], all vertical locations are normalized by the channel half height δ, all velocities are scaled by the friction velocity u_τ, and all friction Reynolds stresses are scaled by the square of the friction velocity, u_τ^2.

Table 3.2. Line and symbol key for turbulent results.

Line Type	Description	Applies to
---------	Non-SHS data	Moser [29] or Simulation Benchmark
———	$Re_\tau \approx 180$ simulations	All geometries
– – –	$Re_\tau \approx 395$ simulations	"
– ·· –	$Re_\tau \approx 590$ simulations	"

Symbol Type	Description	Applies to
⊞	Benchmark U_{bulk} profile	Moser [29] only
∗	Simulation U_{bulk} profile	Comparison with Moser [29]
○	Simulation R_{11} profile	"
⊕	Simulation R_{22} profile	"
⊗	Simulation R_{33} profile	"
●	Simulation R_{12} profile	"
□	15μm - 15μm ridge	All Re_τ
△	30μm - 30μm ridge	"
◊	30μm - 50μm ridge	"
▽	30μm - 90μm ridge	"
▲	30μm - 30μm post	"
♦	30μm - 50μm post	"
▼	30μm - 90μm post	"
☆	Experimental data	From Daniello, *et al.* [11]

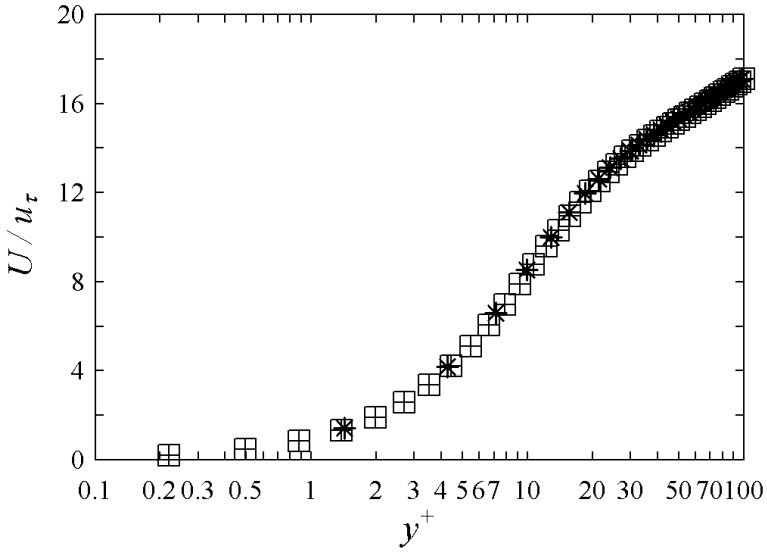

Figure 3.5. $Re_\tau \approx 180$: A comparison of near wall velocity profiles obtained from Moser *et al.* [29] (⊞) and the CFD code (∗) for turbulent channel flow between two infinite parallel plates.

3.3.1 $Re_\tau \approx 180$

As seen in Figures 3.5 through 3.10 (subsequent pages), the velocity profiles and Reynolds stresses generated from the CFD code matched closely with those from [23] and [29]. The small discrepancies seen in the velocity profiles are most likely a result of numerical error, and a consequence of different numerical methods being employed. Kim and Moser used spectral method codes, whereas the CFD code used in current research employs a second order staggered mesh scheme (see Section 2.2 for more details). Note that the symbol and line types shown in Table 3.2 are used consistently throughout all turbulent data presented in this chapter, Chapter 4, and Chapter 5. By convention, lines refer to either data used for benchmarking the code (Moser *et al.* [29]) or the smooth, non-SHS channel data (the CFD benchmark data to follow), for comparison with SHS results. The resolution independence study (Section 4.3), uses a modified version of this convention.

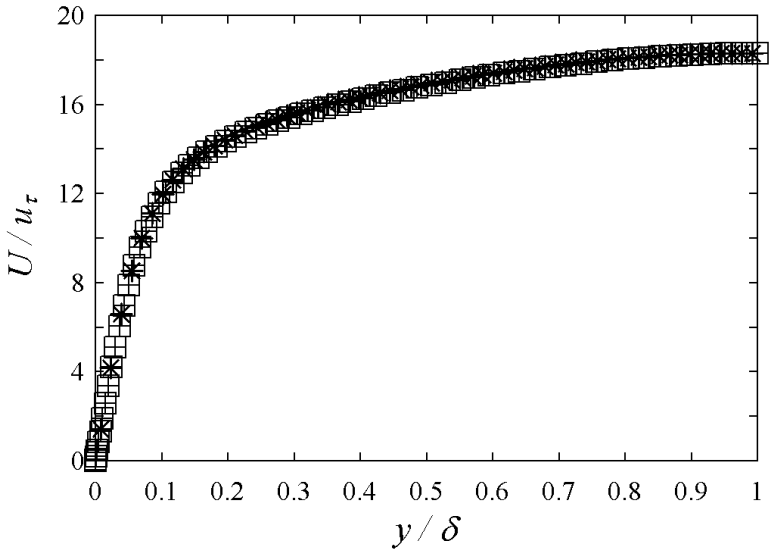

Figure 3.6. $Re_\tau \approx 180$: A comparison of overall half channel velocity profiles obtained from Moser *et al.* [29] (⊞) and the CFD code ($*$) for turbulent channel flow between two infinite parallel plates.

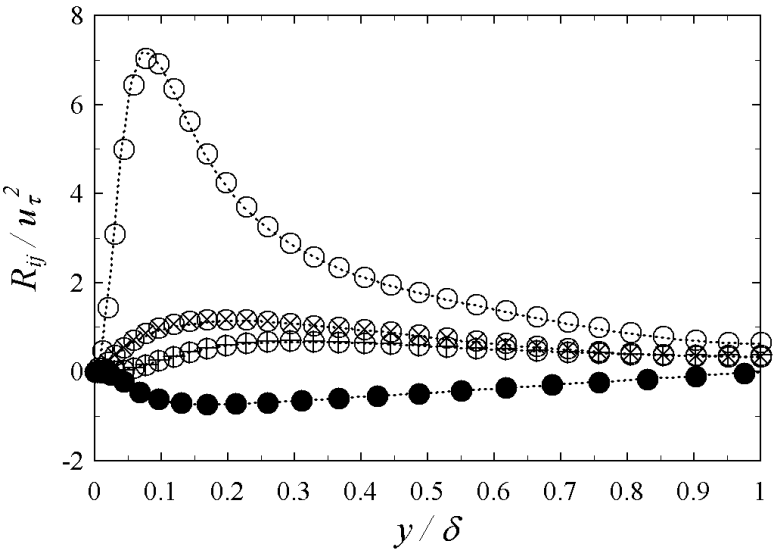

Figure 3.7. $Re_\tau \approx 180$: A comparison of Reynolds stresses obtained from Moser *et al.* [29] (symbols; see Table 3.2) and the CFD code (lines) for turbulent channel flow between two infinite parallel plates.

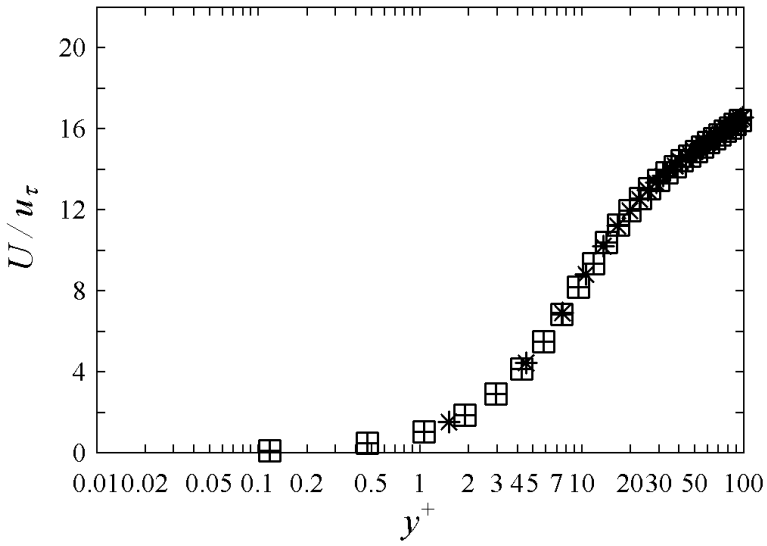

Figure 3.8. $Re_\tau \approx 395$: A comparison of near wall velocity profiles obtained from Moser *et al.* [29] (⊞) and the CFD code (∗) for turbulent channel flow between two infinite parallel plates.

3.3.2 $Re_\tau \approx 395$ and $Re_\tau \approx 590$

In order to trust results from SHS simulations at higher Reynolds numbers, the CFD code was validated at $Re_\tau \approx 395$ and $Re_\tau \approx 590$ against data from [29]. Validation at higher Reynolds numbers required increasing the simulation resolutions to 256^3 grid points for the $Re_\tau \approx 395$ simulation, and 512^3 grid points for the $Re_\tau \approx 590$ simulation in order to properly resolve all relevant scaled in the flow, which become smaller at higher Reynolds numbers. These cases are time consuming, and results from the $Re_\tau \approx 590$ are still reaching steady state, as is evidenced by the appearance of Reynolds stress profiles, especially the non-linearity of the R_{12} profile.

Overall, the $Re_\tau \approx 395$ velocity (Figures 3.8 and 3.9) and Reynolds stress (Figure 3.10) profiles match those from [29] to within 2%, which shows excellent agreement considering the differences in numerical methods explained above. The velocity profiles for the $Re_\tau \approx 590$ case (Figures 3.11 and 3.12) were also within 2% of the benchmark, despite the fact that the simulation has yet to reach statistical steady

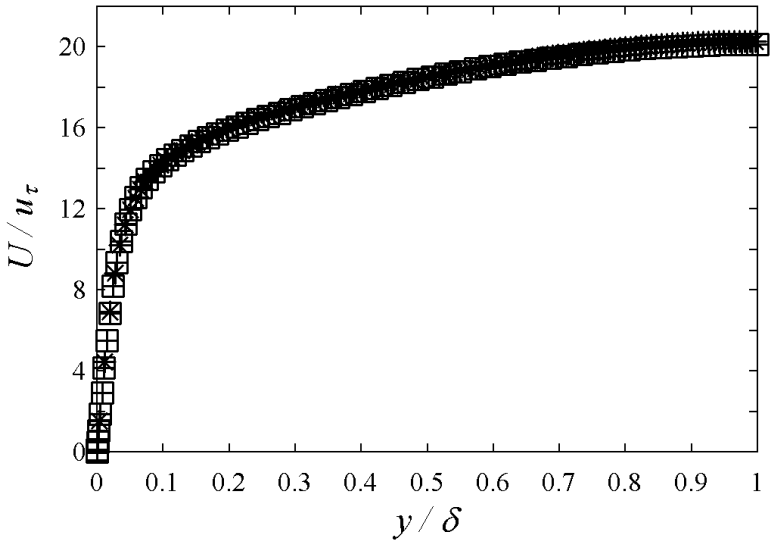

Figure 3.9. $Re_\tau \approx 395$: A comparison of overall half channel velocity profiles obtained from Moser *et al.* [29] (⊞) and the CFD code ($*$) for turbulent channel flow between two infinite parallel plates.

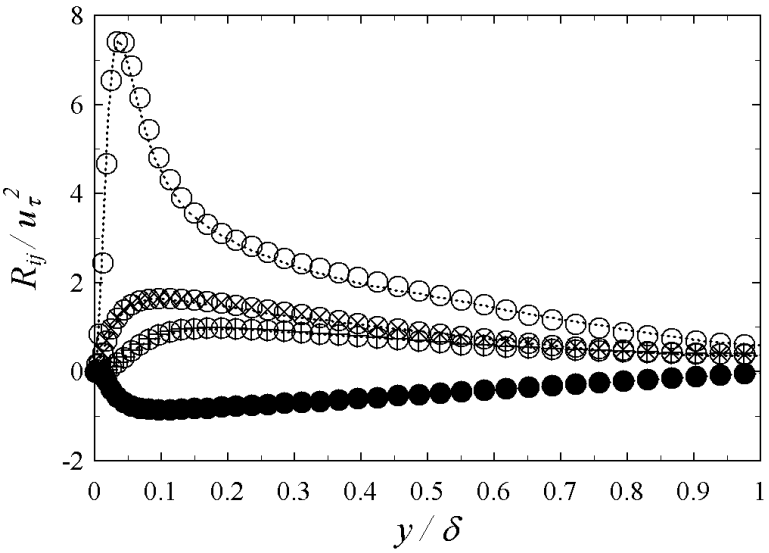

Figure 3.10. $Re_\tau \approx 395$: A comparison of Reynolds stresses obtained from Moser *et al.* [29] (symbols; see Table 3.2) and the CFD code (lines) for turbulent channel flow between two infinite parallel plates.

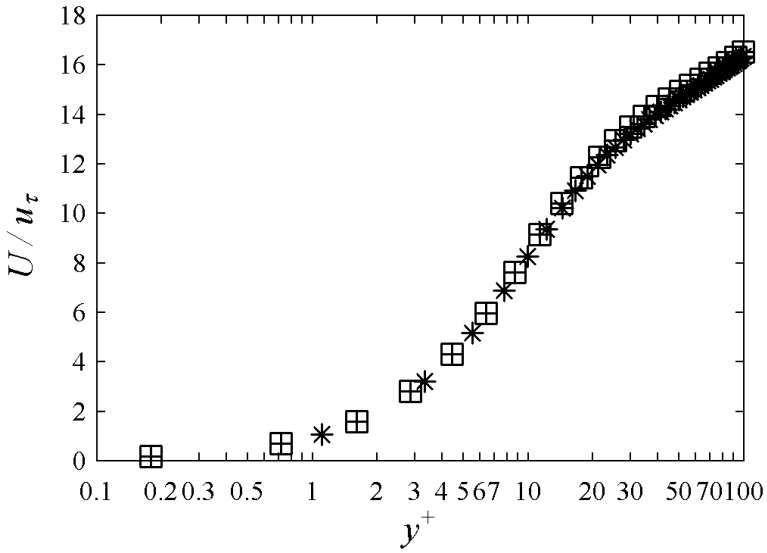

Figure 3.11. $Re_\tau \approx 590$: A comparison of near wall velocity profiles obtained from Moser *et al.* [29] ($\boxplus$) and the CFD code ($*$) for turbulent channel flow between two infinite parallel plates.

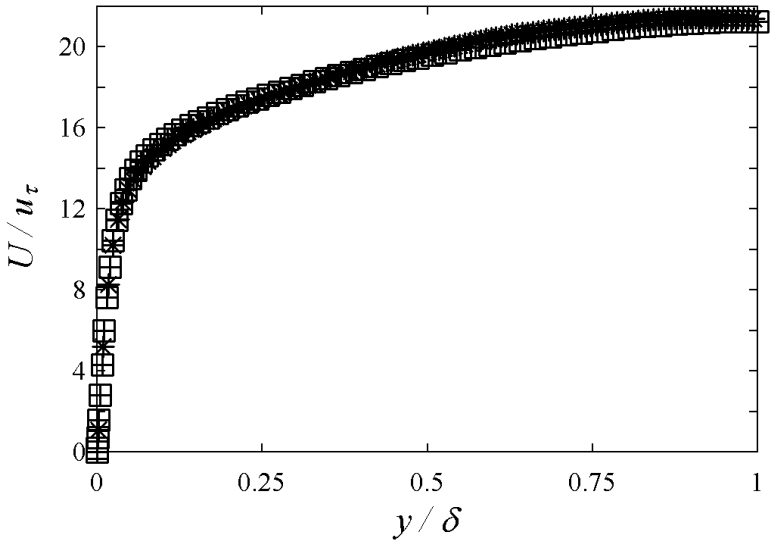

Figure 3.12. A comparison of overall half channel velocity profiles obtained from Moser *et al.* [29] and the CFD code for turbulent channel flow between two infinite parallel plates at $Re_\tau \approx 590$.

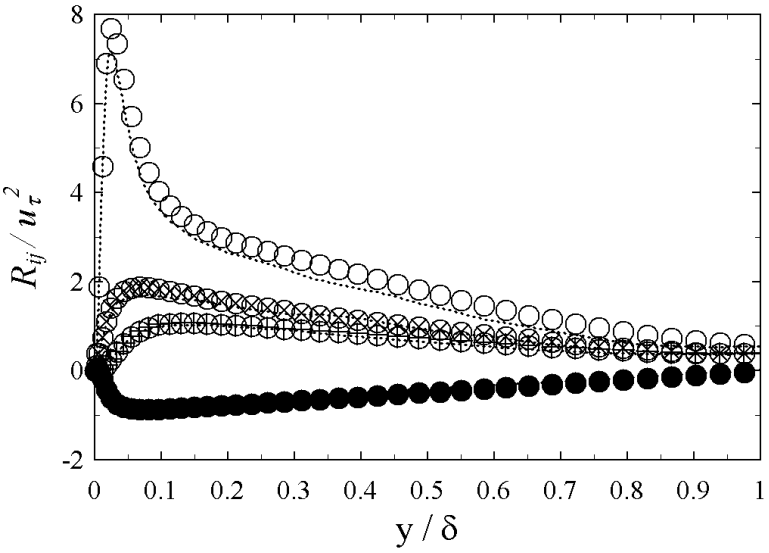

Figure 3.13. $Re_\tau \approx 590$: A comparison of Reynolds stresses obtained from Moser *et al.* [29] (symbols; see Table 3.2) and the CFD code (lines) for turbulent channel flow between two infinite parallel plates.

state. Agreement in the Reynolds stress profiles (Figure 3.13) was not as close, and on average agreed within 5%. Most disagreement was in R_{11}, a direct result of the simulation not yet being at the same Reynolds number or steady state. Agreement for R_{22}, R_{33}, and R_{12} was much better, back within 2% of the benchmark. Appendix C includes a comparison of mean flow variables such as Reynolds numbers, velocity ratios, and skin friction coefficients for the benchmarks and simulations at all three Reynolds numbers.

CHAPTER 4

RESULTS

Upon completing the CFD code validation, simulations were performed in both the laminar and turbulent regime investigating the effect of superhydrophobic surfaces on channel flow. In all cases, the SHS boundary conditions were applied to the bottom wall only, which corresponds to the left hand side of the velocity profile and Reynolds stress plots below (at $y = 0$ or $y = -\delta$ depending on normalization). The top wall remained no-slip throughout.

4.1 Laminar Regime

Laminar investigations are limited to flow over ridges. In these trials, the spacing and width of the ridges, as well as the overall width and height of the channel, was varied. For each geometric arrangement, the mass flow rate was calculated (as the pressure gradient was fixed) and a relationship was discovered between the ridge size, the channel size, and the mass flow rate. In the following results (see Figure 4.1), d represents the ridge width in the Z-direction, w is the gap width in the Z-direction, W is the overall channel width (in Z), and H is the overall channel height (in Y).

The ratio of the channel height to the ridge spacing H/w, and the ratio of the ridge width to the ridge spacing d/w, were varied. The mass flow rate was computed and scaled by the mass flow rate of a channel with two no-slip walls. The scaled mass flow rate is denoted M^*. $M^* = 1$ corresponds to a channel whose mass flow rate is equal to that of a standard no-slip channel. $M^* > 1$ indicates the surfaces are enabling a greater mass flow rate for a given pressure gradient, which is related

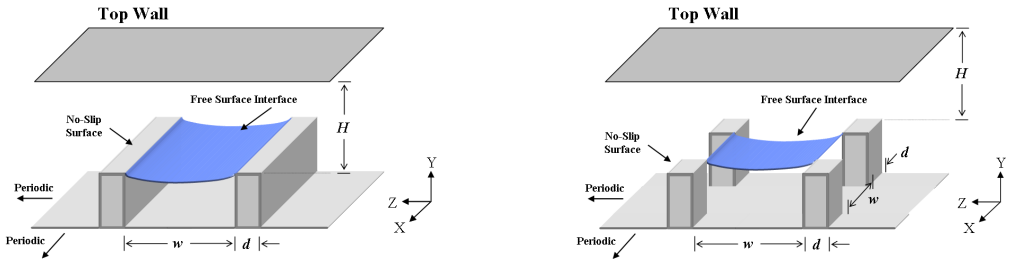

(a) Microridge dimensions. (b) Micropost dimensions.

Figure 4.1. Schematic of relevant dimensions for ridges, posts, and the overall channel height, used in laminar results.

to drag reduction. $M^* < 1$ would suggest the surface features actually *decrease* the mass flow rate for a given pressure gradient, which would indicate a drag *increase*. Results are shown in Figure 4.2.

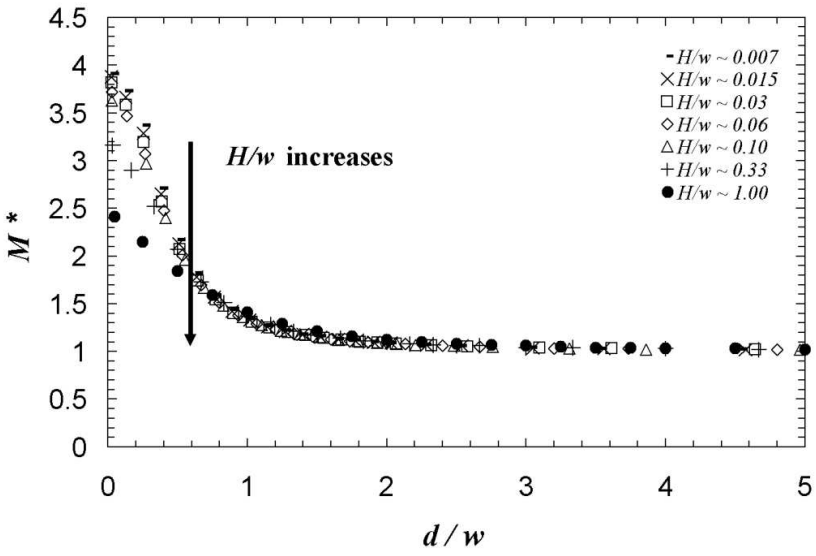

Figure 4.2. Trends in M^* versus channel and ridge proportions. Notice that increasing H/w lessens the effect of the ridges, as does increasing d/w.

Figure 4.2 shows a clear relationship between the scaled mass flow rate M^* and the channel size and ridge spacing ratios H/w and d/w. As the ratio of the ridge width d to the ridge spacing w increases, the shear-free surface area on the bottom wall

becomes smaller, and M^* approaches unity. This is expected, as M^* is scaled by the mass flow rate for a normal no-slip channel. As d/w decreases and approaches zero, the no-slip surface area becomes smaller, and M^* approaches four, indicating a fourfold increase in the mass flow which is equivalent to a 75% reduction in the drag experienced along the bottom wall. This result matches with the limit of Phillip's solution for a regular array of streamwise no-shear bands (discussed in Section 3.2.4), and discussed in [34]. The effect of the channel height to ridge width ratio H/w on the mass flow rate is important in determining the limits of the drag reducing capabilities of the surfaces in laminar flows. A small H/w indicates a very thin channel with respect to feature spacing, and yields the highest scaled mass flow rates. Drag reduction is maximized in very thin channels, or channels with very wide ridge spacing. It is interesting to note that even in the lower limit where d/w is effectively zero, the maximum scaled mass flow rate for a channel, with the channel height to spacing ratio near 100%, is much lower than that where the ratio is below 1%. Thus, the ratio d/w has an upper effective limit, governed by the channel height and feature size. Some work was done investigating the relationship between the angle of the flow over the ridges and the resulting M^*, but this work was not analyzed to the point of trend identification. Further investigation into the relationship between the size and spacing ratios, flow angle, and M^* could be considered as an extension to current research.

4.2 Turbulent Regime

4.2.1 Background

Previous experimental work [33, 34, 11], which motivated current research, employed feature sizes and spacing that ranged from 15μm to 90μm. Current turbulent flow research employs similarly dimensioned features. It is important to point out that most of the quantities reported are dimensionless (as was the case in the valida-

tion section, and in Kim's and Moser's data), and, as shown in the previous section, the ratio of channel height to feature spacing is important to characterize the drag reducing performance of the superhydrophobic surface. For simplicity, the ridge and post dimensions reported reflect their real-world counterparts. Results for turbulent flows over superhydrophobic surfaces include trials with friction Reynolds numbers ranging from $Re_\tau \approx 180$ to $Re_\tau \approx 590$, over uniform ridges and posts of width and spacing ranging from 15μm to 90μm, and 30μm square posts, uniformly-spaced (in X and Z) from 30μm to 90μm. Results include velocity profiles and Reynolds stresses, as well as wall shear stresses and skin friction coefficients.

Unlike the smooth wall cases, the profiles are no longer symmetric about the channel's vertical center plane, thus results for the entire channel height are included. Prominent slip velocities, up to 65% and 75% of the mean velocity are present for the ridge and post cases, respectively. Also, a decrease of up to 23% and 32% in the peak values of R_{11} the wall with the superhydrophobic surface boundary conditions was found for the ridges and posts, respectively. This suggests the surfaces do in fact reduce the turbulence production near the wall, which indicates a reduction in wall shear stress, and thus in drag. At $Re_\tau \approx 180$, reduction in the wall shear stress τ_w (see Equation 3.10) ranged from about 8% for $15\mu m - 15\mu m$ ridges to 25% for $30\mu m - 90\mu m$ ridges. Also at $Re_\tau \approx 180$, a 10% reduction in wall shear stress was observed for $30\mu m - 30\mu m$ posts, while $30\mu m - 90\mu m$ posts produced nearly 37% drag reduction. At $Re_\tau \approx 395$, $30\mu m - 30\mu m$ ridges had a slip velocity 45% of the mean velocity and a shear stress reduction near 15%. $30\mu m - 90\mu m$ posts showed a slip velocity nearly 80% of the mean velocity, and a shear stress reduction at the SHS near 45%. At $Re_\tau \approx 590$, $30\mu m - 30\mu m$ ridges had a slip velocity 40% of the mean velocity and a shear stress reduction near 18%. $30\mu m - 90\mu m$ posts showed a slip velocity nearly 75% of the mean velocity, and a shear stress reduction at the SHS

near 50%. See Chapter 5 for more details, specifically an explanation of the lower than expected slip velocities reported for the $Re_\tau \approx 590$ case.

4.2.2 $Re_\tau \approx 180$

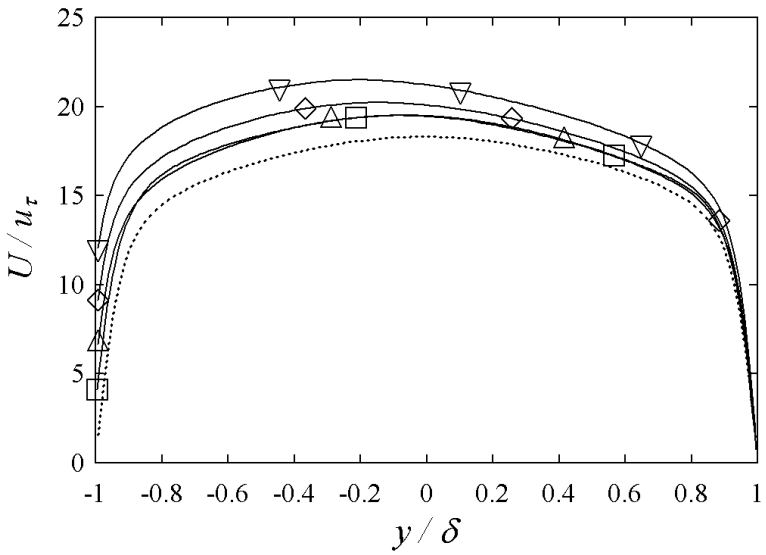

Figure 4.3. $Re_\tau \approx 180$: Bulk velocity profiles from a simulation with uniform streamwise ridges of size and spacing $15\mu m - 15\mu m(\square)$, $30\mu m - 30\mu m(\triangle)$, $30\mu m - 50\mu m(\Diamond)$, and $30\mu m - 90\mu m(\triangledown)$. Note the large slip velocity. See Table 3.2 for symbol description.

Figures 4.3 and 4.4 show velocity profiles for ridges at a Reynolds number $Re_\tau \approx 180$. An average slip velocity exists along the SHS wall. Also, the peak of the velocity profile has shifted slightly toward the bottom wall. Results from the ridge cases show slip velocities and peak mean velocities that increase with increased width to spacing ratio d/w. In addition, the peak velocity moves closer to the SHS. The $15\mu m$-$15\mu m$ ridge case was performed with 256 grid points in each direction for validation purposes, explaining the presence of a data point closer to the SHS. It is interesting to note that in Figure 4.4 the velocity profiles for $15\mu m$-$15\mu m$ and $30\mu m$-$30\mu m$ ridges cross at roughly y/δ = -0.8 ($y^+ \approx 28$). This appears to be a characteristic of the flow resulting from the interplay of the slip velocity and the subsequent asymmetry in the

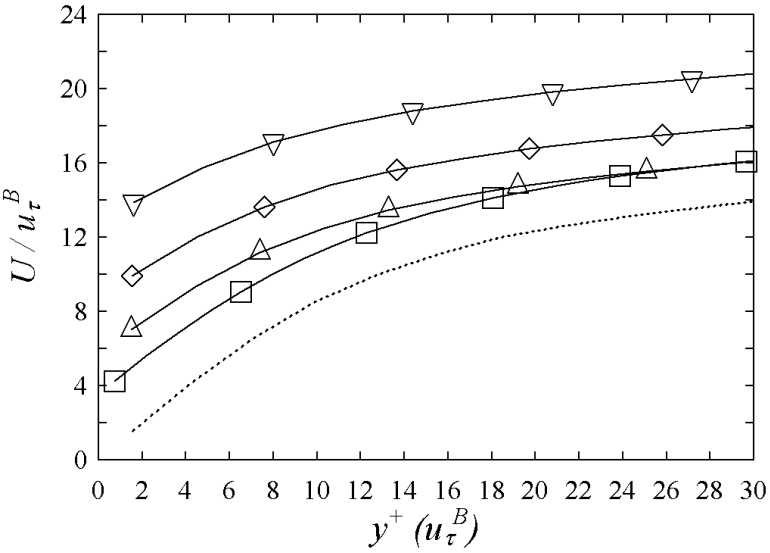

Figure 4.4. A close look at the bulk velocity profile near the SHS, for the same ridges at $Re_\tau \approx 180$. Note the velocity is normalized by the value of u_τ at the bottom wall.

velocity profile and not a resolution issue, as the profile for $30\mu m$-$30\mu m$ ridges at twice the resolution (256^3) is nearly identical to the one presented in the resolution independence section later in this chapter (Figure 4.27). Figure 4.5 shows a distinct decrease in the peak values of R_{11}, indicating a decrease in the turbulent intensity at the SHS. In addition, the location of the central minimum R_{11} values have shifted toward the bottom wall. R_{22} shows a distinct loss of symmetry, with a decrease in the peak above the SHS, similar to R_{11}. R_{33} shows clear non-zero values at the SHS, indicating an average transverse velocity not present in the smooth channel. Again note the asymmetry present in R_{33}. The linearity of the mid-channel R_{12} values is largely unaffected; however, the peak values of R_{12} have decreased near the SHS and increased near the channel's top wall, indicating the turbulent structures present in the channel have changed location but may otherwise resemble those found in the smooth channel. Note that, as with the validation results presented in Chapter 3, all Y locations are normalized by the channel half height δ, all velocities are scaled by

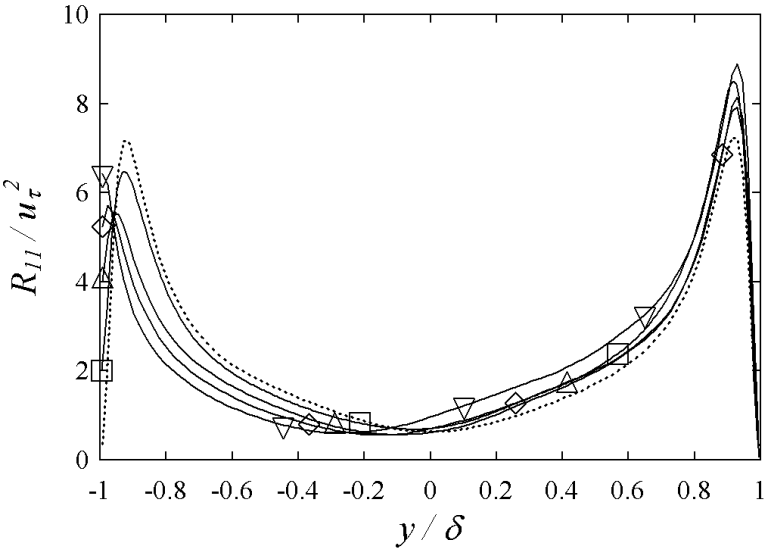

Figure 4.5. R_{11} profiles for ridges at $Re_\tau \approx 180$. Note the non-zero values of R_{11} at the SHS.

the friction velocity u_τ, and all friction Reynolds stresses are scaled by the square of the friction velocity, u_τ^2. In the middle of the channel, the slope of the shear stress (R_{12}) must balance the fixed pressure gradient, resulting in curves that are all parallel in this region. Note that, due to the slip velocities present in the X and Z directions, R_{11} and R_{33} become non-zero at the SHS.

Figures 4.9 and 4.10 show velocity profiles for uniform posts ranging is size from $30\mu m - 30\mu m$ (width and spacing in X and Z) to $30\mu m - 90\mu m$, at a Reynolds number $Re_\tau \approx 180$, similar to those reported for ridges above. A very large slip velocity can be seen, which is nearly the value of the bulk velocity. Furthermore, the location of the peak velocity has shifted much closer to the wall than was observed with the ridged surfaces. The presence of this slip velocity explains the large reduction in wall shear stress for the posts reported above. The peak velocity shows a noticeable increase as the post spacing (w) is increased.

In Figure 4.11, the characteristic R_{11} peaks at the SHS are completely absent, and the maximum value of R_{11} is about 32% lower than the peak value at the upper wall.

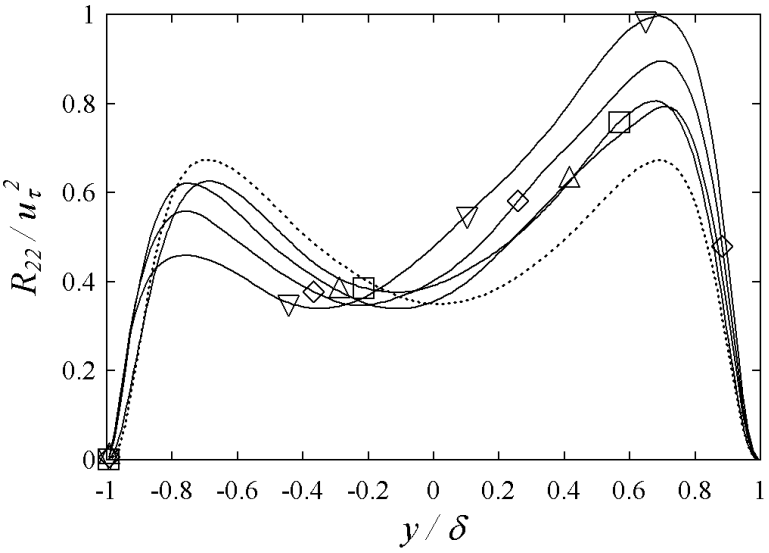

Figure 4.6. R_{22} profiles ridges at $Re_\tau \approx 180$.

R_{11} for $30\mu m - 50\mu m$ and $30\mu m - 90\mu m$ posts do not have any peak above the SHS, and instead the peaks lie **on** the SHS. Asymmetry is observed in R_{22} and R_{33}, with R_{33} values at the SHS once again non-zero. Despite large changes in the shape of the Reynolds stress profiles, R_{12} retains its linear region away from the channel walls, but exhibits the same shift of location and results in a lower (negative) peak value over the SHS. Since the mean pressure gradient remains constant in these simulations, a net reduction in drag or shear on the superhydrophobic boundary leads to a corresponding increase in the net shear on the smooth wall. With reduced shear, turbulence levels decrease near the superhydrophobic boundary. The turbulence levels increase on the no-slip boundary because of the higher shear now present near the upper wall.

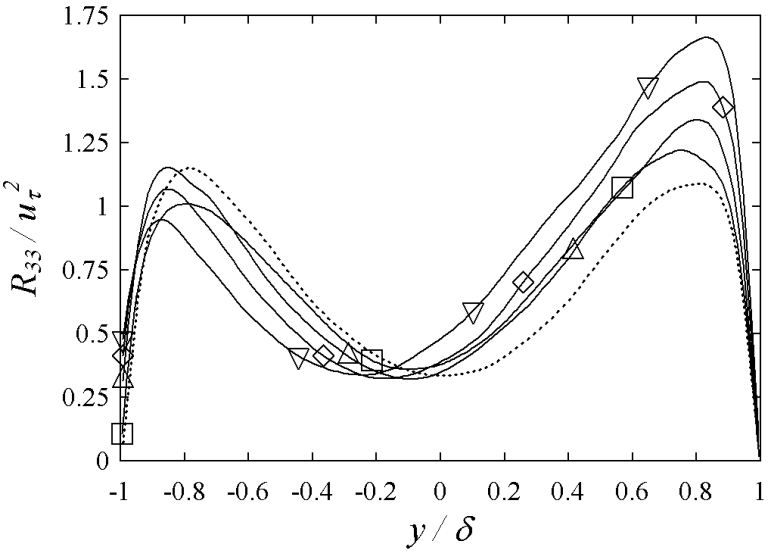

Figure 4.7. R_{33} profiles for ridges at $Re_\tau \approx 180$.

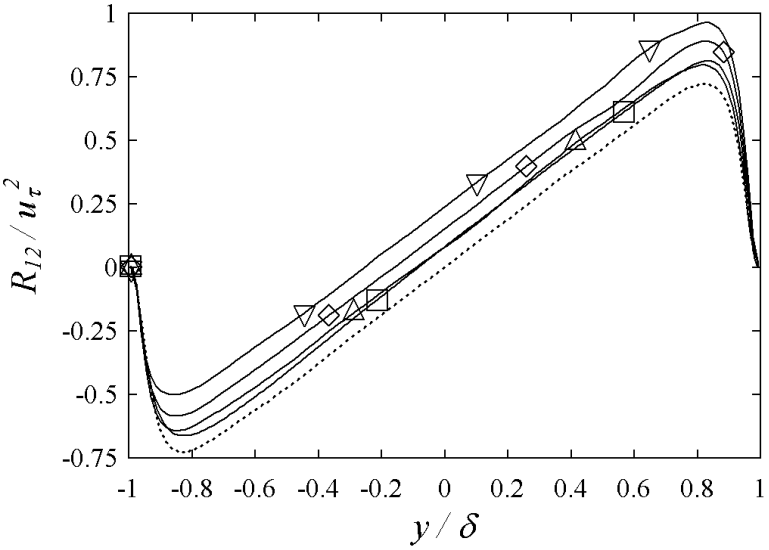

Figure 4.8. R_{12} profiles for ridges at $Re_\tau \approx 180$. Note that the linearity of R_{12} is unaffected by the presence of the SHS, but the peaks and symmetry are both altered.

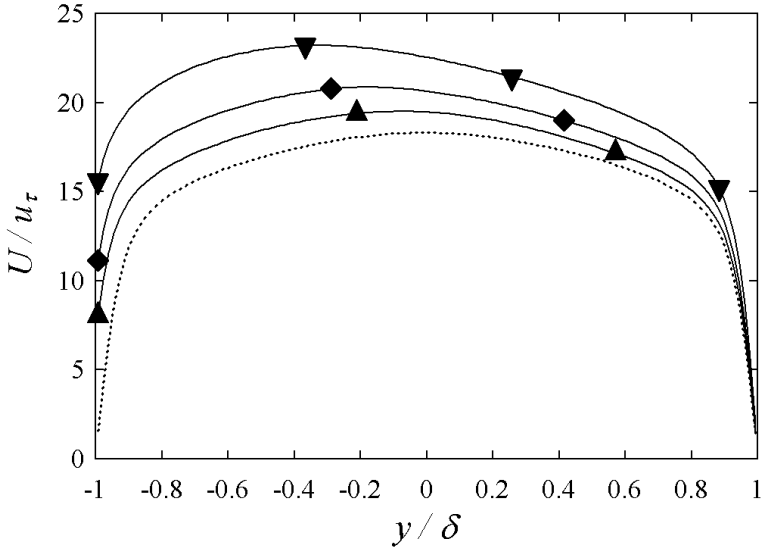

Figure 4.9. $Re_\tau \approx 180$: Bulk velocity profiles from a simulation with uniform posts of size and spacing $30\mu m - 30\mu m$(▲), $30\mu m - 50\mu m$(♦), and $30\mu m - 90\mu m$(▼). Note the large slip velocity and increase in peak velocity with increased post spacing. See Table 3.2 for symbol description.

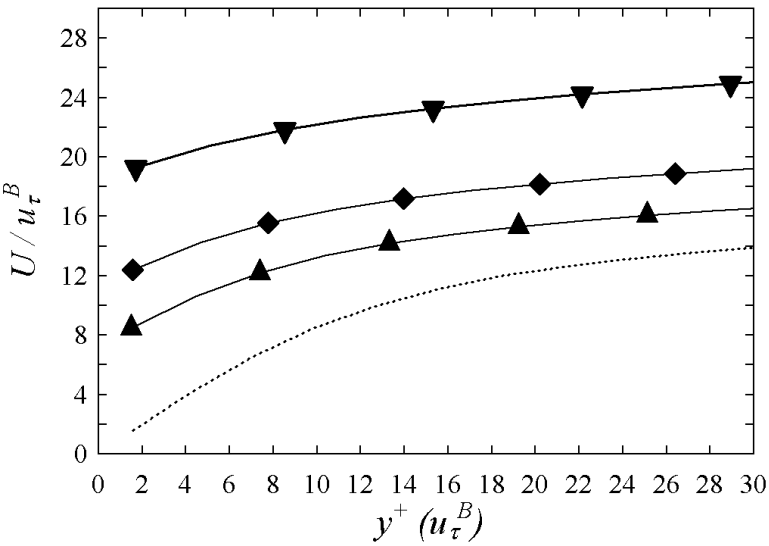

Figure 4.10. A close look at the bulk velocity profile near the SHS for the same posts at $Re_\tau \approx 395$. Note the velocity is normalized by the value of u_τ at the bottom wall.

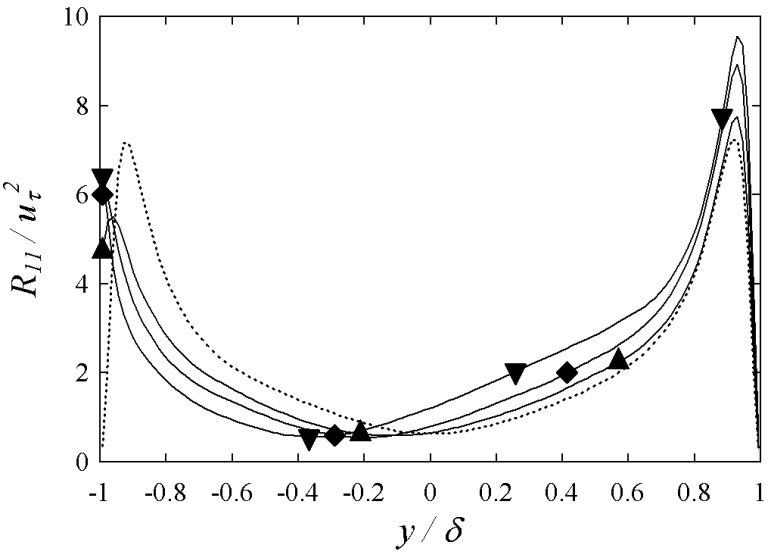

Figure 4.11. R_{11} profiles for posts at $Re_\tau \approx 180$. Note the non-zero values of R_{11} at the SHS.

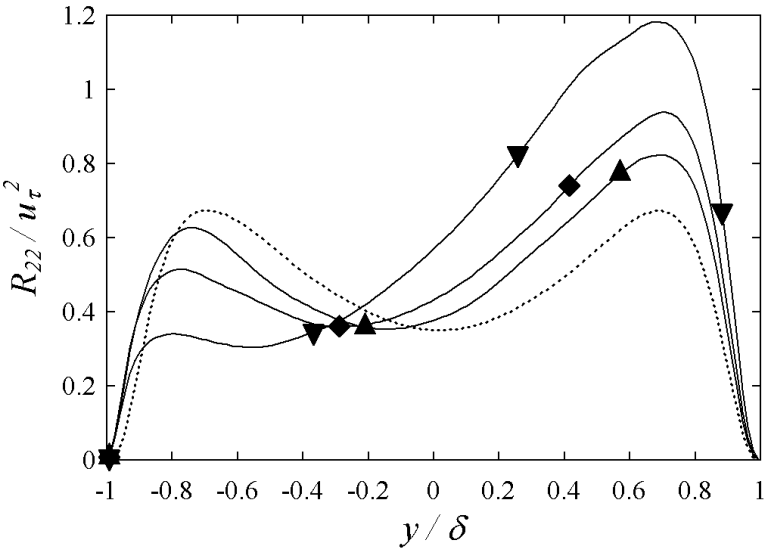

Figure 4.12. R_{22} profiles for posts at $Re_\tau \approx 180$. There is marked asymmetry in the profiles.

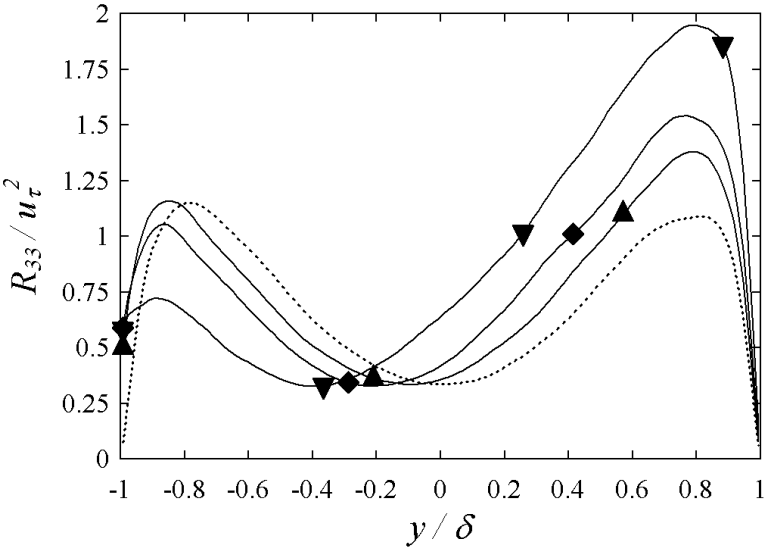

Figure 4.13. R_{33} profiles for posts at $Re_\tau \approx 180$. Again, note the non-zero values of R_{33} at the SHS. There is only a small peak for the $30\mu m - 90\mu m$ case.

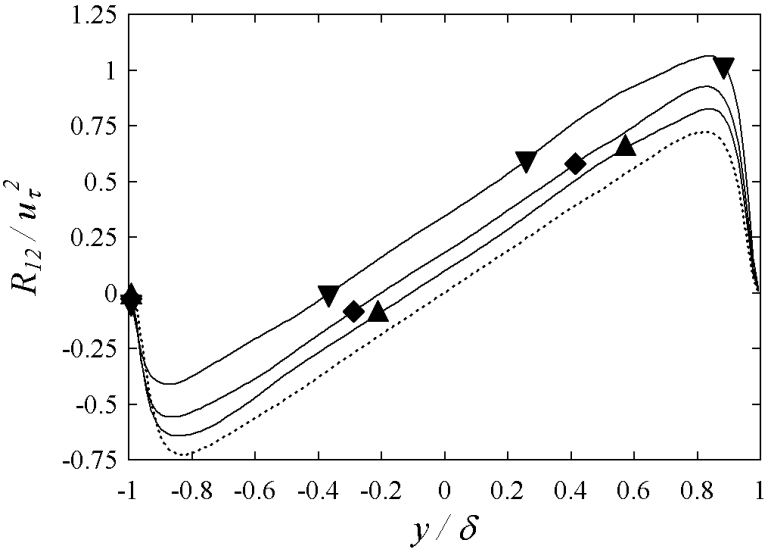

Figure 4.14. R_{12} for posts at $Re_\tau \approx 180$. Note that the linearity of R_{12} is unaffected by the presence of the SHS, but, as with the ridge cases, the peak shifts and the profile is not symmetric about $y = 0$. .

4.2.3 $Re_\tau \approx 395$

In addition to the $Re_\tau \approx 180$ cases presented above, several ridge and post geometries were studied at a higher friction Reynolds number of $Re_\tau \approx 395$, to correspond with the validation presented in Chapter 3, which, in turn, is based upon the Reynolds numbers selected by Moser *et al.* [29]. Not all geometric arrangements investigated at $Re_\tau \approx 180$ were considered at this higher Reynolds number. $15\mu m - 15\mu m$ and $30\mu m - 30\mu m$ ridges were considered, as well as $30\mu m - 90\mu m$ posts. An investigation of the relationship between average slip velocities, wall shear stress reduction, and Reynolds number is discussed in Chapter 5. As with the $Re_\tau \approx 180$ results, all Y locations are normalized by the channel half height δ, all velocities are scaled by the friction velocity u_τ, and all Reynolds stresses are scaled by the square of the friction velocity, u_τ^2.

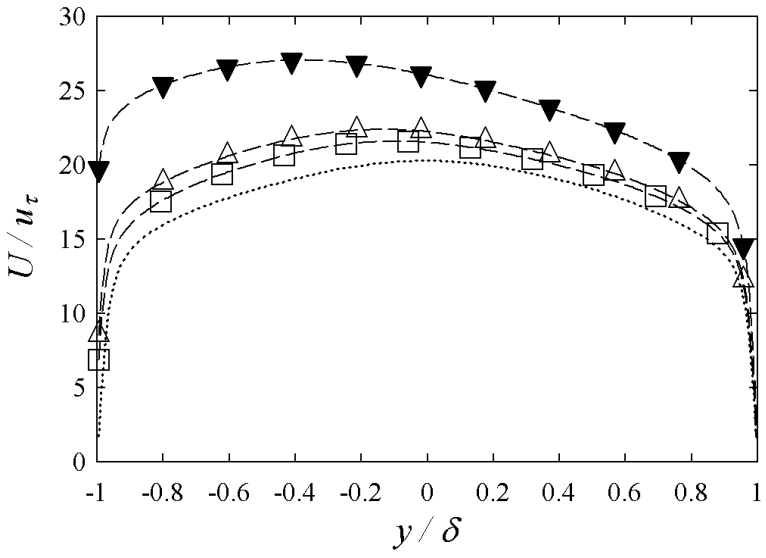

Figure 4.15. $Re_\tau \approx 395$: Bulk velocity profiles from simulations with $15\mu m - 15\mu m$(□) and $30\mu m - 30\mu m$(△) ridges, and $30\mu m - 90\mu m$(▼) posts. Again, note the large slip velocity. See Table 3.2 for symbol description.

The $30\mu m - 90\mu m$ posts exhibit a large slip and peak velocity in Figure 4.15 compared to the $15\mu m - 15\mu m$ and $30\mu m - 30\mu m$ ridges. The asymmetry present in the $30\mu m - 90\mu m$ post velocity profile is pronounced.

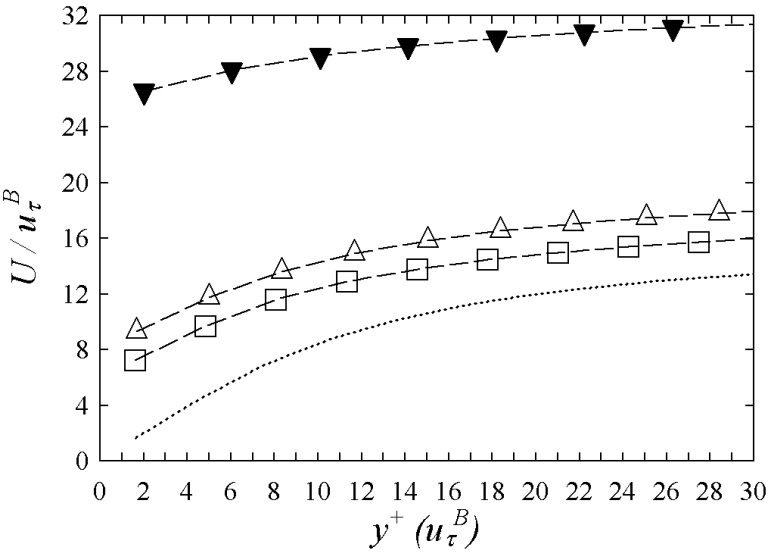

Figure 4.16. $Re_\tau \approx 395$: A close look at the bulk velocity profile near the SHS for the posts and ridges. Note the velocity is normalized by the value of u_τ at the bottom wall.

$Re_\tau \approx 180$ cases suffer from "low Reynolds number effects" (see [23]). The $Re_\tau \approx 395$ cases show much sharper R_{11} peaks in Figure 4.17 which are also much closer to the channel walls. The $30\mu m - 90\mu m$ post case has the R_{11} peak at the SHS. For $30\mu m - 90\mu m$ posts, R_{11} on the top half of the channel is larger than the ridge cases by nearly a factor of two, while on the bottom half the profile minimum is lower (and much more pronounced) than the ridges cases.

While still zero at the walls, the asymmetry present in R_{22} profiles is clearly present in Figure 4.18 than R_{22} profile for similar geometries at lower Reynolds numbers. The R_{22} peaks at the SHS for the post case is nearly half as high as the ridge cases, and is nearly 30% higher at the upper wall.

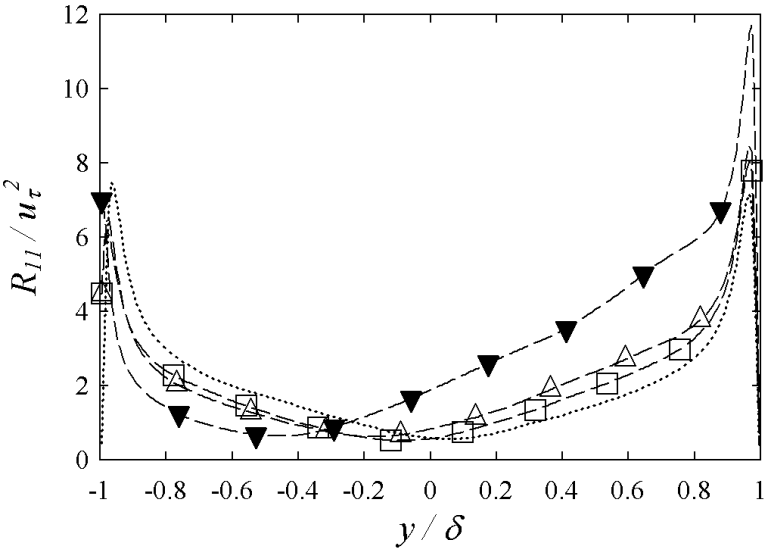

Figure 4.17. $Re_\tau \approx 395$: R_{11} profiles for ridges and posts. Note the non-zero values of R_{11} on the SHS.

R_{33} has a fairly large non-zero value at the SHS for all cases in Figure 4.19, and a high peak at the smooth (upper) wall. The "wobble" present in the $30\mu m - 90\mu m$ post case shows the case may not yet be at steady state.

R_{12} for the $30\mu m - 90\mu m$ post case in Figure 4.20 shows a linear region across the middle of the channel, revealing the case is nearly at steady state (contrary to the observations made in Figure 4.19). All R_{12} profiles are shifted upward from the smooth case and show decreasing peak values near the SHS, and increasing peak values on the smooth wall.

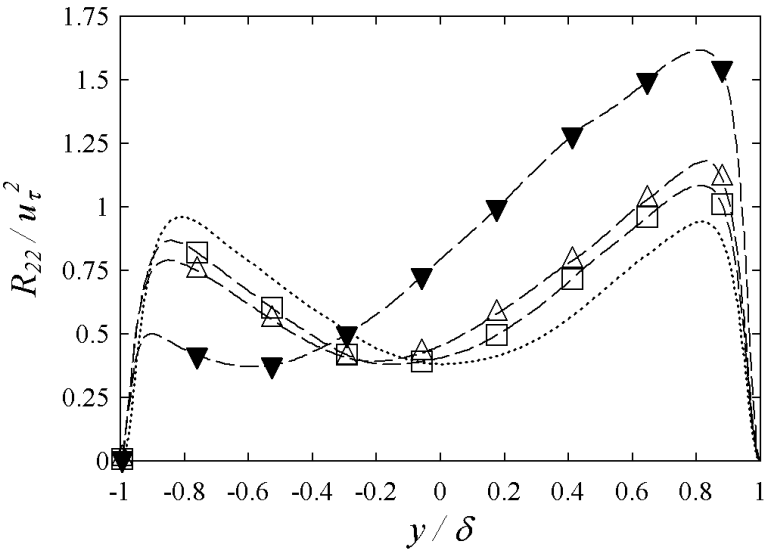

Figure 4.18. $Re_\tau \approx 395$: R_{22} profiles for ridges and posts.

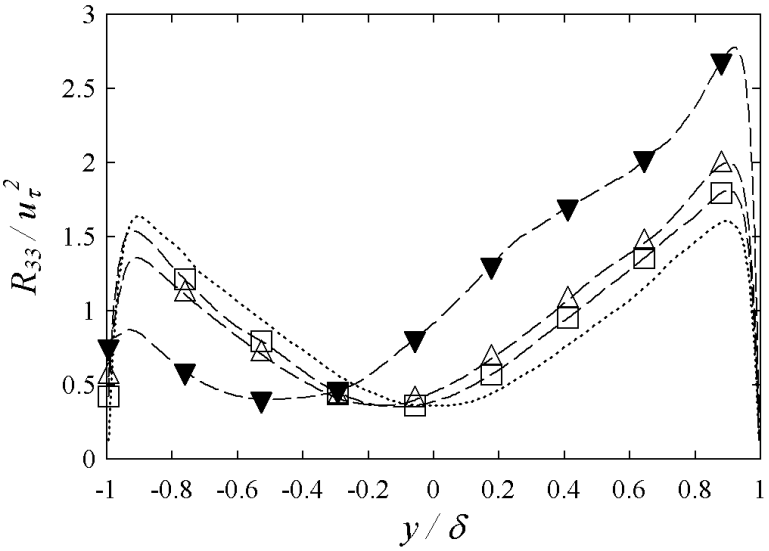

Figure 4.19. $Re_\tau \approx 395$: R_{33} profiles for ridges and posts. Again, note the non-zero values of R_{33} on the SHS.

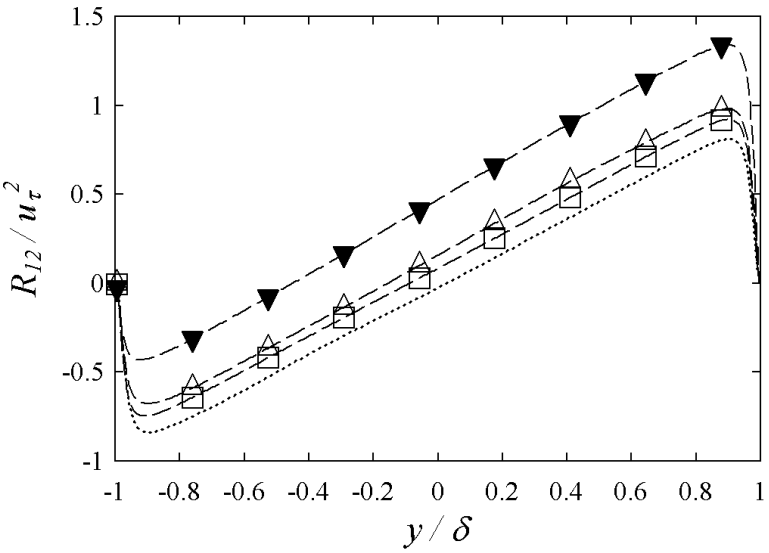

Figure 4.20. $Re_\tau \approx 395$: R_{12} profiles for ridges and posts. Note that the linearity of R_{12} is unaffected by the presence of the SHS.

4.2.4 $Re_\tau \approx 590$

To better understand how the SHS behaves at higher Reynolds numbers, simulations were performed at a third friction Reynolds number of $Re_\tau \approx 590$. As with the $Re_\tau \approx 395$ cases, only a limited range of geometries were studied in the interest of time, including $30\mu m - 30\mu m$ ridges and $30\mu m - 90\mu m$ posts. In order to properly resolve all scales relevant to a flow at $Re_\tau \approx 590$, the resolution was increased fourfold in each direction, and the simulation time step decreased to maintain stability. As such, the $Re_\tau \approx 590$ results are still reaching steady state. This is most obvious in Figure 4.26, where R_{12} does not yet exhibit a linear region near the center of the channel. This is most likely not due to the presence of the features, as R_{12} for identical features at $Re_\tau \approx 180$ and $Re_\tau \approx 395$, once at steady state, contains linear regions, as expected. This fact is also seen in the "wiggle" present in the entirety of the Reynolds stress plots, and slip velocities that are consistently lower (as a percentage of the bulk velocity) than those found in the $Re_\tau \approx 395$ cases, which is unexpected and indictave of a simulation that has yet to reach steady state. Again, as with the $Re_\tau \approx 180$ and $Re_\tau \approx 395$ results above, all Y locations are normalized by the channel half height δ, all velocities are scaled by the friction velocity u_τ, and all Reynolds stresses are scaled by the square of the friction velocity, u_τ^2.

In Figure 4.21, velocity profiles for the $Re_\tau \approx 590$ cases exhibit the most asymmetry out of all cases previously investigated, with the peak velocity occurring very close to the SHS. Figure 4.22 shows a slip velocity for the $30\mu m - 90\mu m$ post case that is more than three times greater than that for $30\mu m - 30\mu m$ ridges, the largest disparity in slip velocities out of all cases studied clearly showing that posts out-perform ridges even at higher Reynolds numbers.

As with the $Re_\tau \approx 395$ cases, the R_{11} peaks in Figure 4.23 are very sharp and located close to the smooth channel wall. At the SHS, the peak for the $30\mu m - 90\mu m$ posts lies on the wall. Also, R_{11} for the $30\mu m - 90\mu m$ posts crosses the profiles for

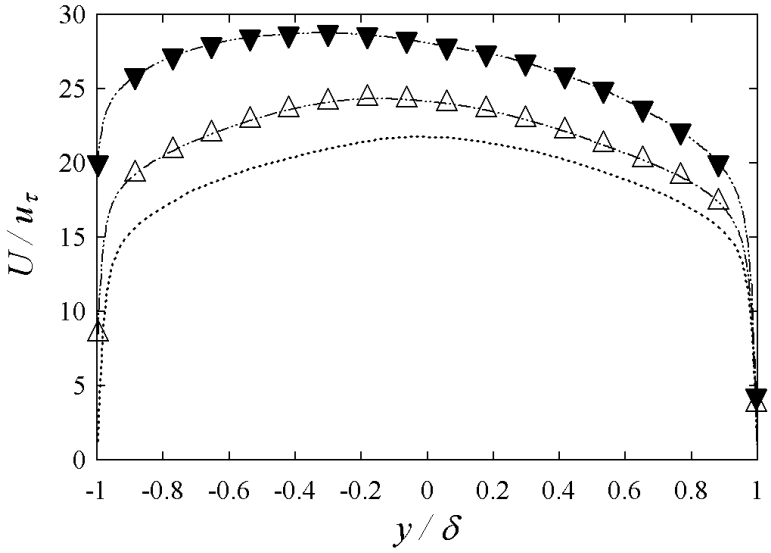

Figure 4.21. $Re_\tau \approx 590$:Bulk velocity profiles from simulations with $30\mu m - 30\mu m(\triangle)$ ridges and $30\mu m - 90\mu m(\blacktriangledown)$ posts. Note the large slip velocity. See Table 3.2 for symbol description.

the ridge and smooth cases, exhibiting higher values on the upper half of the channel, and a lower minimum value near the SHS.

Trends in R_{22} (Figure 4.24) match those for both the $Re_\tau \approx 180$ and $Re_\tau \approx 395$ cases. For the $30\mu m - 90\mu m$ posts, the peak at the SHS is nearly flat.

Similar to R_{22}, R_{33} trends (Figure 4.25) behave as those at lower Reynolds numbers. The R_{33} peak for $30\mu m - 90\mu m$ posts nearly lies upon the SHS, similar to R_{11} profiles for this geometry at the same Reynolds number.

As with cases at lower Reynolds numbers, R_{12} profiles (Figure 4.26) shift upward from their smooth wall counterparts with increased feature spacing. The non-linearity in all $Re_\tau \approx 590$ R_{12} profiles shows the need for the simulations to reach steady state.

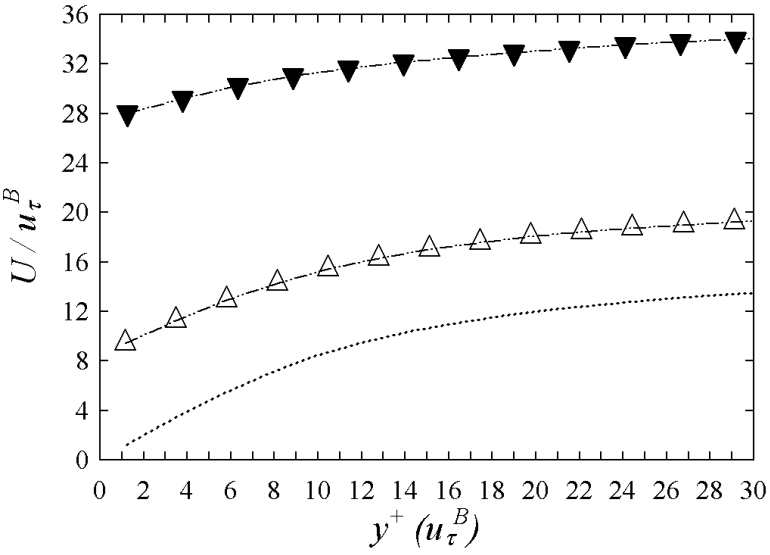

Figure 4.22. $Re_\tau \approx 590$: A close look at the bulk velocity profile near the SHS for ridges and posts. Note the velocity is normalized by the value of u_τ at the bottom wall.

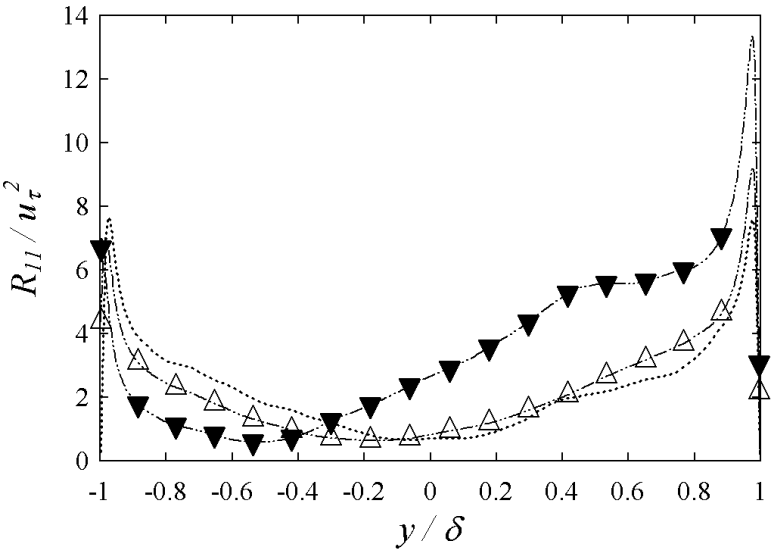

Figure 4.23. $Re_\tau \approx 590$: R_{11} profiles for ridges and posts. Note the non-zero values of R_{11} at the SHS. The "wiggle" present in R_{11} tends to indicate the simulations have yet to reach steady state.

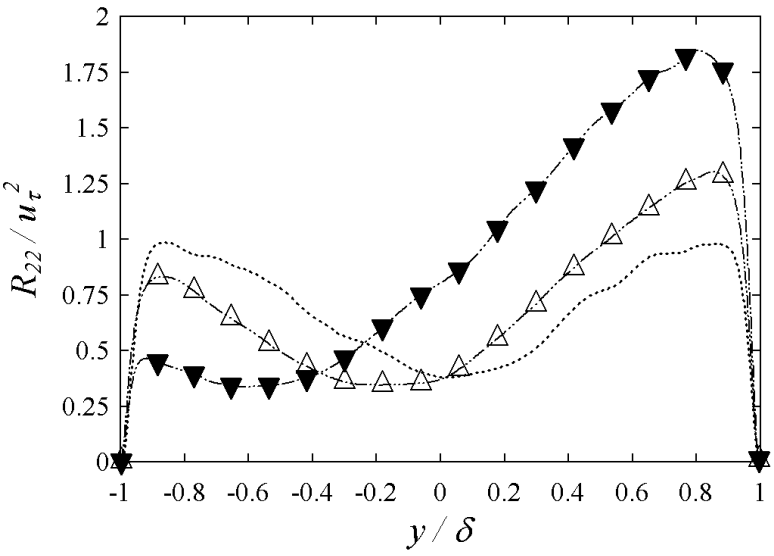

Figure 4.24. $Re_\tau \approx 590$: R_{22} profiles for ridges and posts.

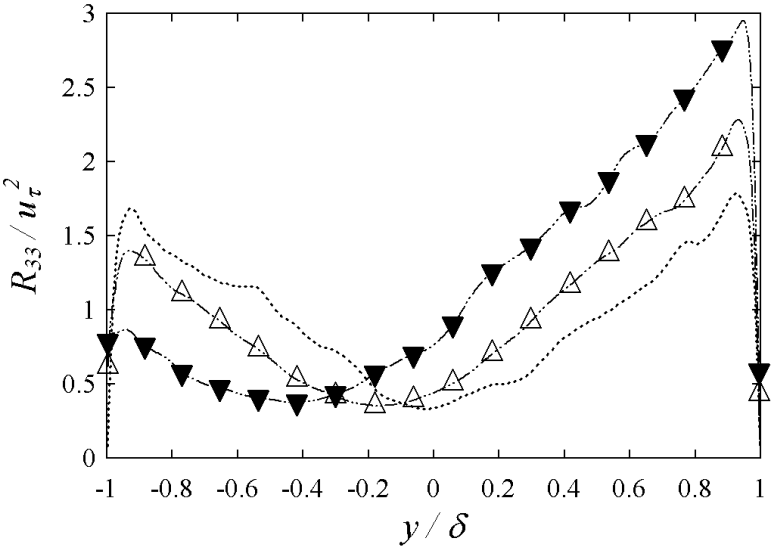

Figure 4.25. R_{33} profiles for ridges and posts at $Re_\tau \approx 590$.

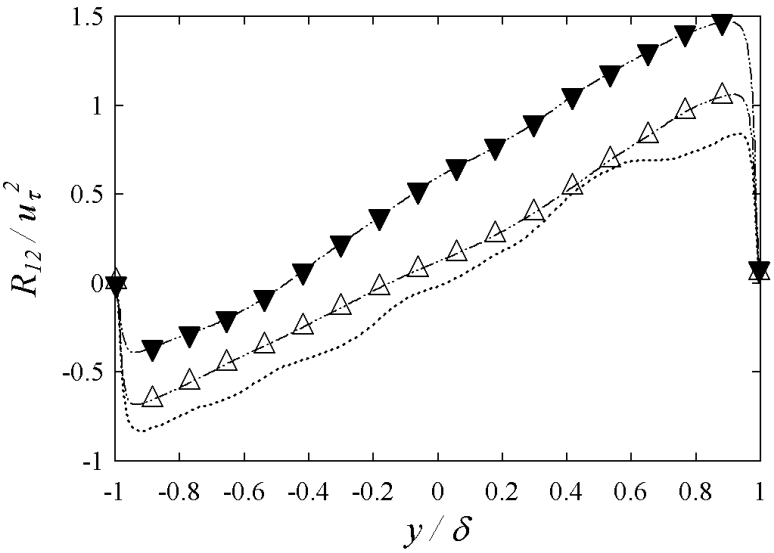

Figure 4.26. R_{12} profiles for ridges and posts at $Re_\tau \approx 590$. The lack of linearity in R_{12} indicates the simulations are not yet at steady state.

4.3 Resolution Independence

When dealing with simulations of turbulence, specifically those which are run at a variety of resolutions (as is the case with this research), it is customary to conduct a resolution independence study. In many cases, this involves performing the same simulation at two resolutions and comparing mean and higher order statistics. For this study, $30\mu m - 30\mu m$ ridges at $Re_\tau \approx 180$ were employed. The first case was run with 128 grid points in each direction, for a total of 128^3 (2,097,152) points over the entire domain. This resolution was employed for most $Re_\tau \approx 180$ cases described previously. To provide a means of comparison to the case with $30\mu m - 30\mu m$ ridges with 128^3 grid points, the same case was run with 256 gridpoints in each direction, for a total of 256^3 (16,777,216) points in the entire domain. One consequence of doubling the resolution in each direction, and one cause of the small variation in the results, stems from the locations of the grid points very close to the walls of the channel. The non-uniform mesh (see Section 2.3) weights resolution toward the walls. Simulations run at higher resolutions place grid points closer to the channel walls, and alter the velocity profiles and shear stresses slightly. This is most notable in Figure 4.28, where the velocity profiles near the SHS are examined. The channel's physical dimensions remain constant for all simulations performed.

On average, the profiles in Figure 4.27 exhibit less that 2% difference, which is contained mainly near the center of the channel. The two simulations are not at precisely the same Reynolds number, which is most evident at the center of the channel, where there is a small ($< 5\%$) but noticeable difference between the two profiles.

Similar to Figure 4.27, Figure 4.28 examines the near-wall velocity for $30\mu m - 30\mu m$ ridges at the two resolutions investigated. Note the gridpoints of the 256^3 simulation reach closer to the wall than those of the 128^3. The profiles differ very little until the last two points of the 128^3 simulation, where they differ less than

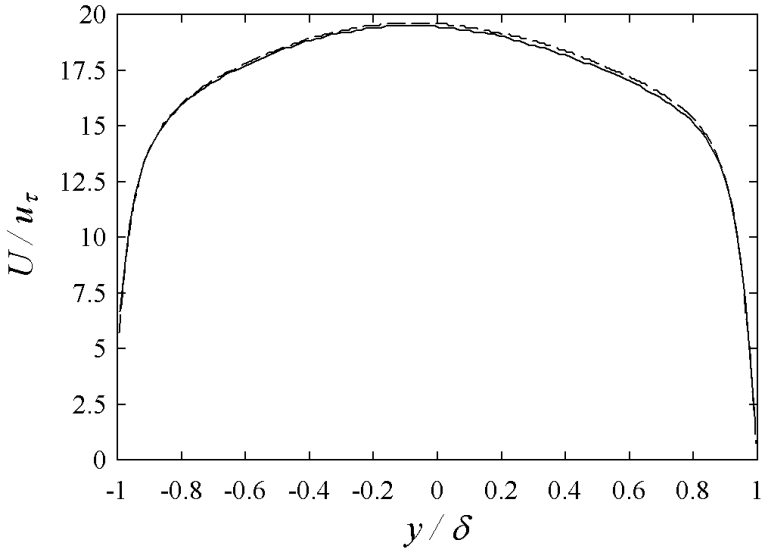

Figure 4.27. Comparison of bulk velocity profiles obtained from $30\mu m - 30\mu m$ ridge simulations at $Re_\tau \approx 180$ with resolutions of 128^3 (–) and 256^3 (---).

5%. Note that the velocity at the SHS for the 256^3 case is slightly less than that for the lower resolution case, resulting in a slightly lower slip velocity. This results in slightly higher shear stress at the SHS. If this trend were to continue (as the final grid point location approached the true location of the wall), the current simulations may slightly overestimate drag reduction, but the effect is small compared with the overall drag reduction performace of the SHS.

Figure 4.29 shows noticeable differences in R_{11}, specifically the height of the near-wall peaks and the minimum R_{11} value at the SHS. The value of R_{11} at the SHS for the 256^3 case is expected to be slightly higher than that of the 128^3, as the slip velocity for that case is lower and the shear stress higher. R_{22}, R_{33}, and R_{12} are largely unaffected, and the profiles exhibit less than 4% difference.

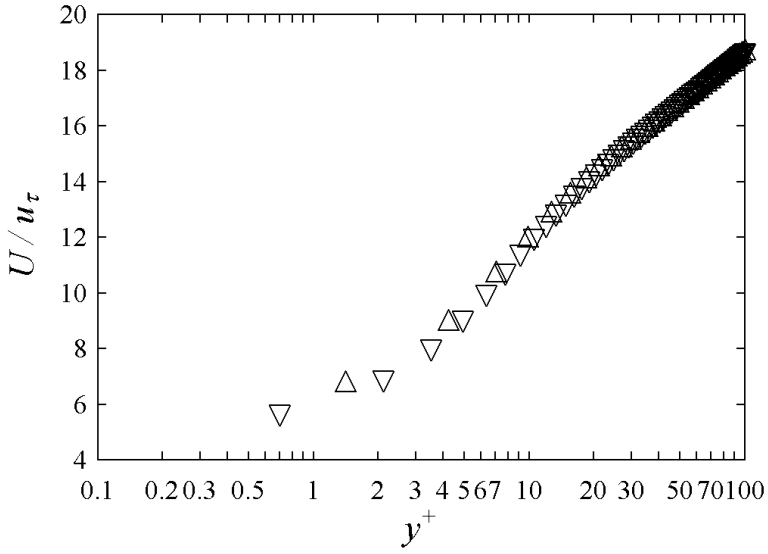

Figure 4.28. A closer look a the velocity profiles from Figure 4.27 near the SHS for ridges for $Re_\tau \approx 180$ ridges at 128^3 ($\triangle$) and 256^3 ($\triangledown$).

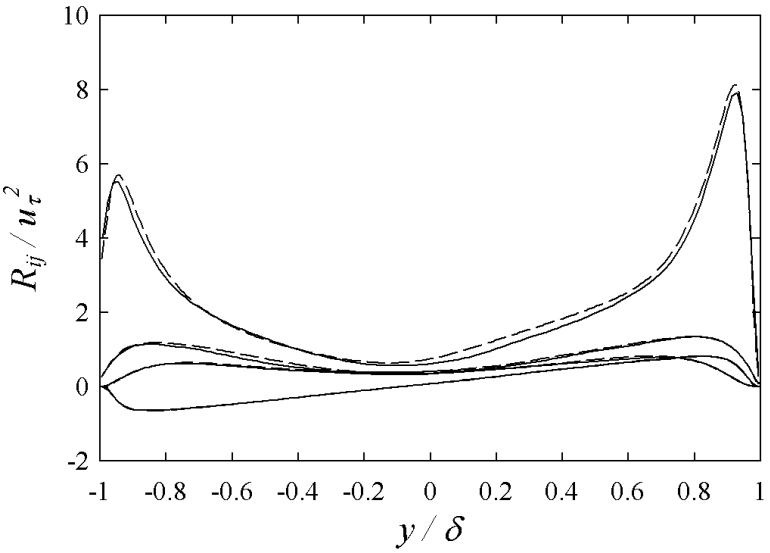

Figure 4.29. Reynolds stress profiles for $Re_\tau \approx 180$, $30\mu m - 30\mu m$ ridge simulations at 128^3 (–) and 256^3 (---).

CHAPTER 5

DISCUSSION

The presence of SHS micro-features has a significant effect on the behavior of turbulent channel flow. Marked changes in the velocity profiles, Reynolds stresses, and wall shear stress are observed for a variety of micro-ridge and micro-post geometries. These results are consistent with the recent experimental work of Daniello, *et al.* [11], who have investigated turbulent flow over superhydrophobic surfaces with similar micro-feature geometries.

Table 5.1. Reynolds numbers, geometric ratios, and length scales for the cases investigated.

Re_τ (nominal)	Geometry	Size	$\frac{d}{w}$	$\frac{wu_\tau}{\nu}$	$\frac{w}{\delta}$
180	Ridges	$15\mu m - 15\mu m$	1.0	16.8	0.09375
		$30\mu m - 30\mu m$	1.0	33.7	0.18750
		$30\mu m - 50\mu m$	0.6	42.1	0.23437
		$30\mu m - 90\mu m$	0.333	50.6	0.28125
	Posts	$30\mu m - 30\mu m$	1.0	33.7	0.18750
		$30\mu m - 50\mu m$	0.6	42.2	0.23437
		$30\mu m - 90\mu m$	0.333	50.6	0.28125
395	Ridges	$30\mu m - 30\mu m$	1.0	74.2	0.18750
	Posts	$30\mu m - 90\mu m$	0.333	110.9	0.28125
590	Ridges	$30\mu m - 30\mu m$	1.0	107.3	0.18750
	Posts	$30\mu m - 90\mu m$	0.333	148.4	0.28125

The $\frac{wu_\tau}{\nu}$ column in Table 5.1 represents the gap width of the various microfeatures investigated in wall units. This is important to consider, as the size of the gap width relative to the size of the turbulent features present in the channel can affect the drag

reduction performance of the SHS in question. A variety of literature ([8], for example) places common riblet dimensions (in wall units) between 15^+ and 50^+. Although spacings are similar to some of the gap widths in Table 5.1, riblets do not support an interface, and the gap widths exceed most common riblet spacings above $Re_\tau \approx 395$. The $\frac{w}{\delta}$ column in Table 5.1 shows the ratio of w, the feature spacing in Z (gap width) to δ, the channel half height. The spacings range to between $\approx 10\%$ and $\approx 30\%$ of the channel half height, or $\approx 5\%$ and $\approx 15\%$ of the overall channel height. This ratio represents the largest physical difference between the experiments of Daniello, *et al.* (some of which are presented later in this chapter) and the current work: typical ratios for Daniello's work are around $\frac{w}{\delta} \approx 0.018898$, which is 80% *smaller* than the smallest feature width investigated, $15\mu m$. This disparity arises from limits that both experiment and simulation are subject to. On the experimental side, it becomes increasingly difficult to manufacture a thin flow cell while still being able to maintain the Reynolds numbers necessary for this work. On the simulation side, it is difficult to simulate a large channel and still resolve very small scales (the microfeatures) without using an extremely fine mesh, which in turn increases simulation time.

5.1 Turbulent Drag Reduction

5.1.1 Relationship to Surface Geometry and Reynolds Number

5.1.1.1 $30\mu m - 30\mu m$ Ridges

$30\mu m - 30\mu m$ ridges and $30\mu m - 90\mu m$ posts were investigated for all three Reynolds numbers considered. As such, these geometries are employed to analyze the drag reducing performance of certain SHS geometries as a function of Reynolds number. In Figure 5.1 the slip velocity of the $Re_\tau \approx 590$ case is close to that of the $Re_\tau \approx 395$ case, indicating the simulation has not yet reached steady state. The peak (and bulk) velocities increase even when scaled by the friction velocity, indicating the friction velocity increases slowly compared to the bulk velocity. There is little

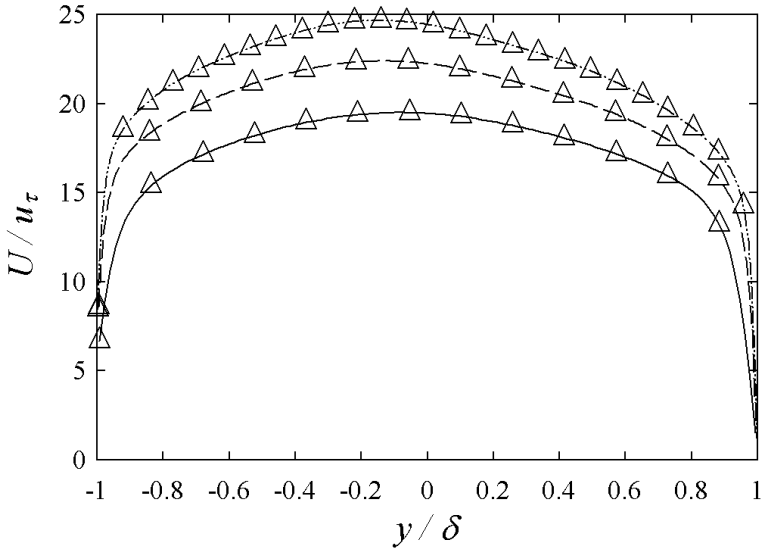

Figure 5.1. Comparison of bulk velocity profiles for $30\mu m - 30\mu m$ ridges ($\triangle$) across the three Reynolds numbers investigated: $Re_\tau \approx 180$ (–), $Re_\tau \approx 395$ (– –), and $Re_\tau \approx 590$ (– ·· –).

noticeable asymmetry in the velocity profiles for $30\mu m - 30\mu m$ ridges. The profiles in Figure 5.2 look nearly identical, and simply shifted upwards with increased friction Reynolds number. The slopes of the profiles are nearly identical, especially above $y^+ \approx 30$. In Figure 5.3, cases with $Re_\tau \approx 395$ and 590 have peaks much higher and closer to the wall than the $Re_\tau \approx 180$ case as one would expect. It appears as if the velocity scales with y^+, indicating the mean flow characteristics have changed little with the addition of SHS, other than the significant slip velocity.

Plotting R_{11} against wall units (which are different for each different Re_τ) helps to place the peaks in the proper location. In Figure 5.4, for example, the peaks for all three Reynolds numbers appear to be in nearly the same location, which is a closer representation of the actual physical phenomenon, namely the nature of the underlying turbulent structures appears to be largely unaffected by the presence of SHS, even as Reynolds number is increases. R_{22} profiles in Figure 5.5 with higher $Re_\tau \approx 395$ and 590 have peaks much higher and closer to the wall than the $Re_\tau \approx 180$

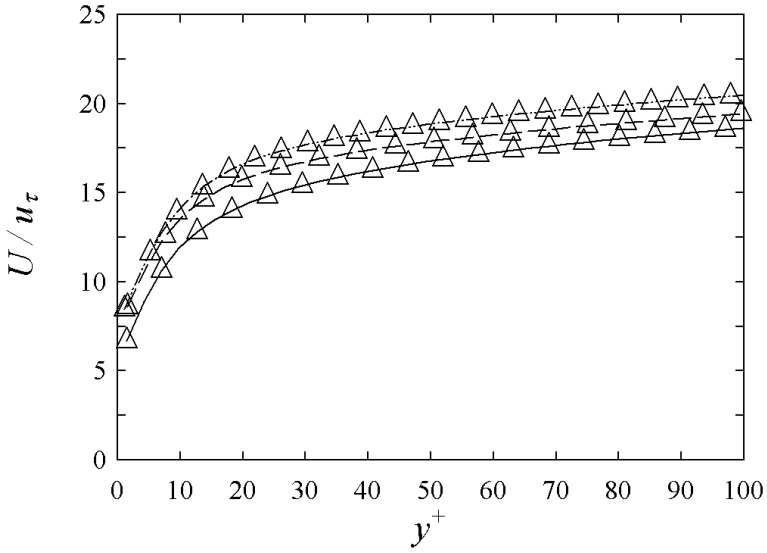

Figure 5.2. A close look at the velocity profiles for $30\mu m - 30\mu m$ ridges near the SHS and plotted against wall units y^+.

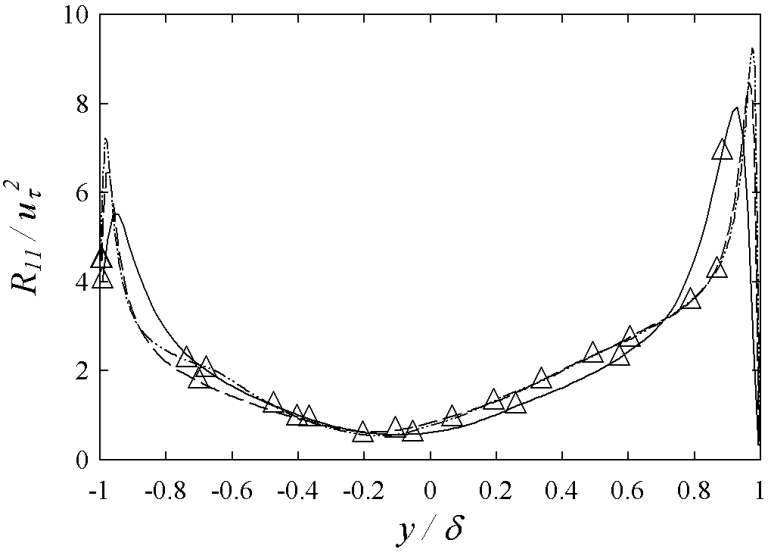

Figure 5.3. Comparison of R_{11} profiles for $30\mu m - 30\mu m$ ridges.

case. As with all other cases investigated, R_{22} consistently goes to zero at the walls (as necessitated by the no-penetration boundary condition), and displays noticeable asymmetry. When plotted against the physical channel location (as opposed to y^+),

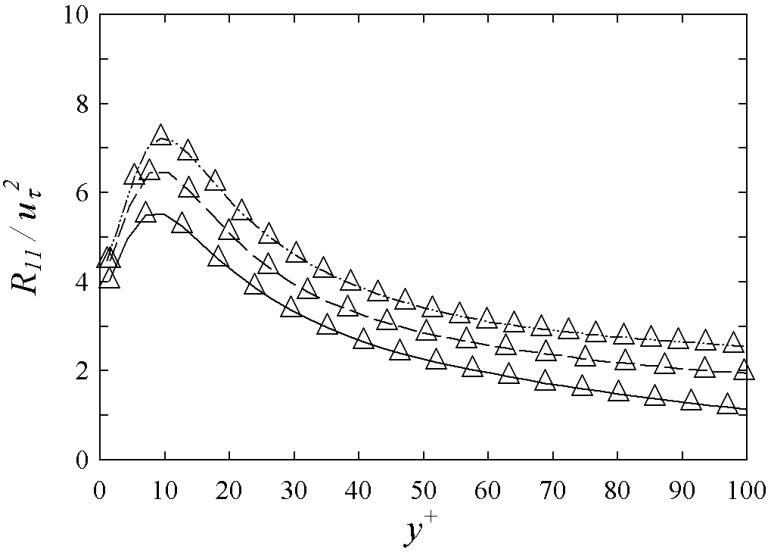

Figure 5.4. R_{11} profiles $30\mu m - 30\mu m$ ridges, plotted against y^+, close to the SHS.

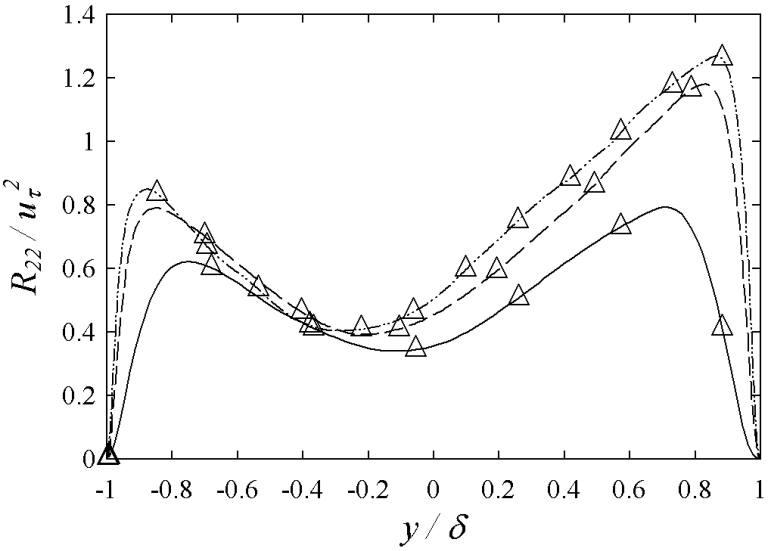

Figure 5.5. R_{22} profiles for $30\mu m - 30\mu m$ ridges.

R_{22} peaks shift toward the walls (and upward). As expected, when plotted against wall units, R_{22} peaks lie at roughly the same y^+ location (as in Figure 5.6) as all peaks

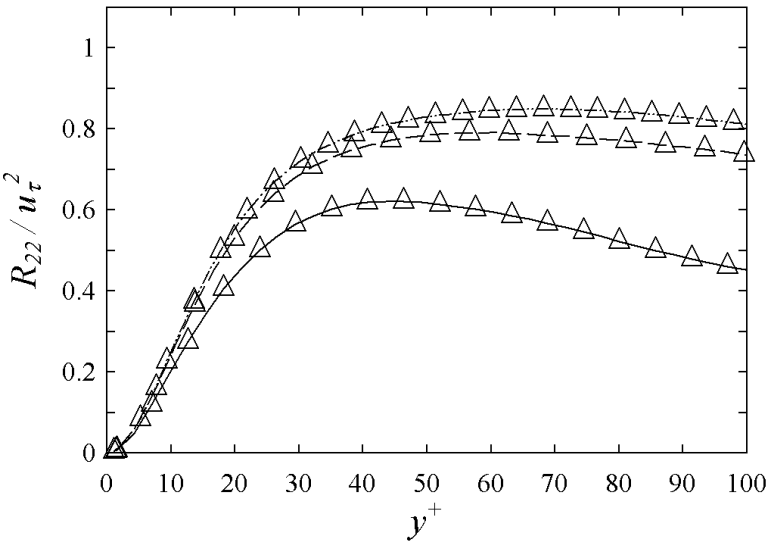

Figure 5.6. R_{22} plotted against wall units for $30\mu m - 30\mu m$ ridges reveals the peak locations to be in roughly the same location.

are due to the turbulent structures (streaks) present in the flow, and the streaks scale with wall units.

The R_{33} profiles (shown in Figure 5.7) with higher $Re_\tau \approx 395$ and $Re_\tau \approx 590$ have peaks much higher and closer to the wall than the $Re_\tau \approx 180$ case. All three cases have non-zero R_{33} values at the SHS. The noticeable "wiggle" in the $Re_\tau \approx 590$ case is due to the simulation not yet reaching steady state. As with R_{22}, R_{33} peaks group roughly at the same y^+ location. Figure 5.8 shows R_{33} trends as a function of Reynolds number. R_{33} at the SHS increases with increased Reynolds number. The peaks do not lie exactly in the same vertical location, which may indicate a change in the transverse component of the turbulent structures as Reynolds number increases.

As with the other Reynolds stresses investigated, the R_{12} profiles in Figure 5.9 at higher $Re_\tau \approx 395$ and $Re_\tau \approx 590$ have peaks higher and closer to the wall than the $Re_\tau \approx 180$ case, again a result of the wall units scaling differently for different Reynolds numbers. The presence of the (mostly) linear mid-channel region indicates

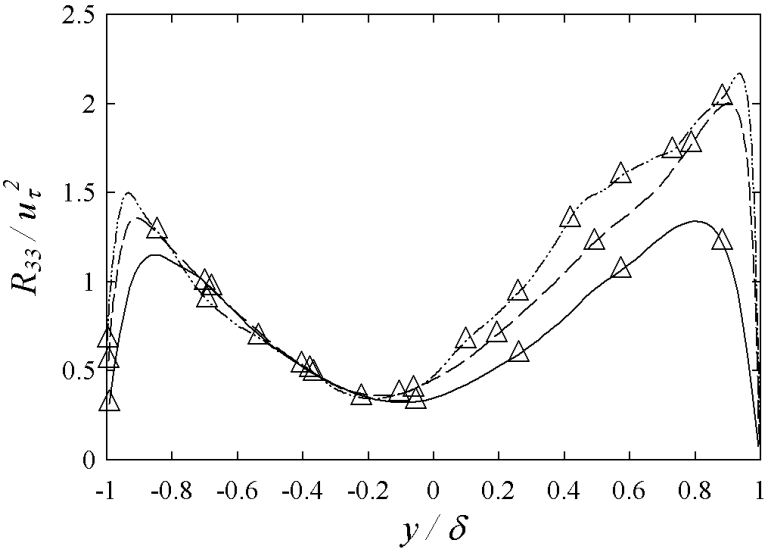

Figure 5.7. R_{33} profiles for t30μm – 30μm ridges.

that (contrary to the suggestions of the R_{33} profiles, the turbulent structures remain fundamentally unaltered, and are simply shifted. The slope of the profiles become closer as they approach the upper wall of the channel. Figure 5.10 takes a closer look at R_{12} for the three Reynolds numbers considered, and reveals the different mid-channel linear region slopes, and similar peak locations near the SHS. Section 5.2.1 has more details on R_{12} normalization and its relation to turbulent structures.

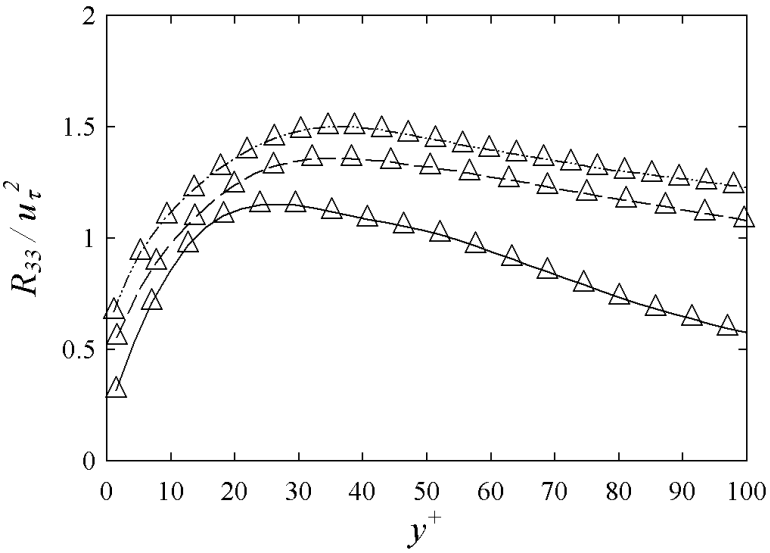

Figure 5.8. Unlike other cases, the R_{33} peaks (for $30\mu m - 30\mu m$ ridges) do not lie exactly in the same vertical location, despite being plotted against y^+.

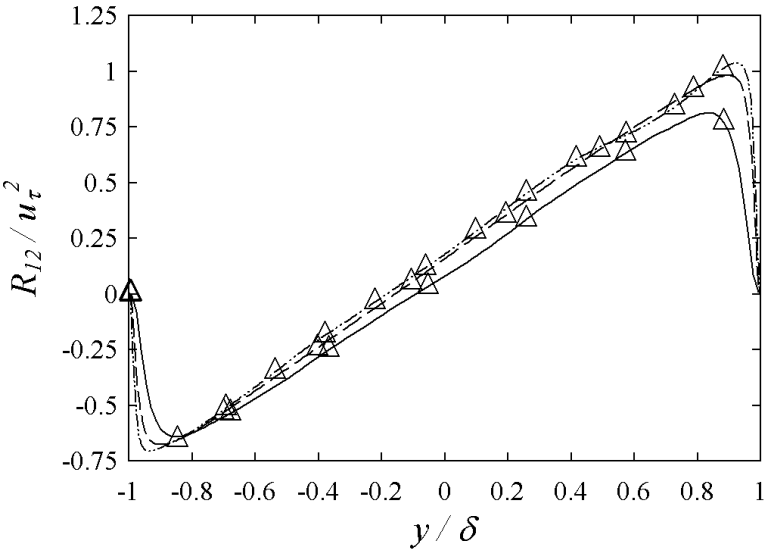

Figure 5.9. R_{12} profiles for $30\mu m - 30\mu m$ ridges.

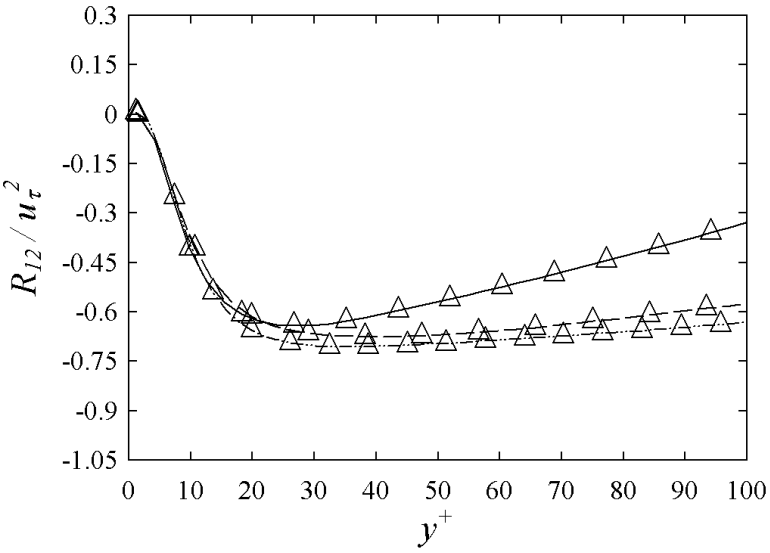

Figure 5.10. R_{12} profiles for $30\mu m - 30\mu m$ ridges at $Re_\tau \approx 180$ (–), $Re_\tau \approx 395$ (– –), and $Re_\tau \approx 590$ (– ·· –).

5.1.1.2 $30\mu m - 90\mu m$ Posts

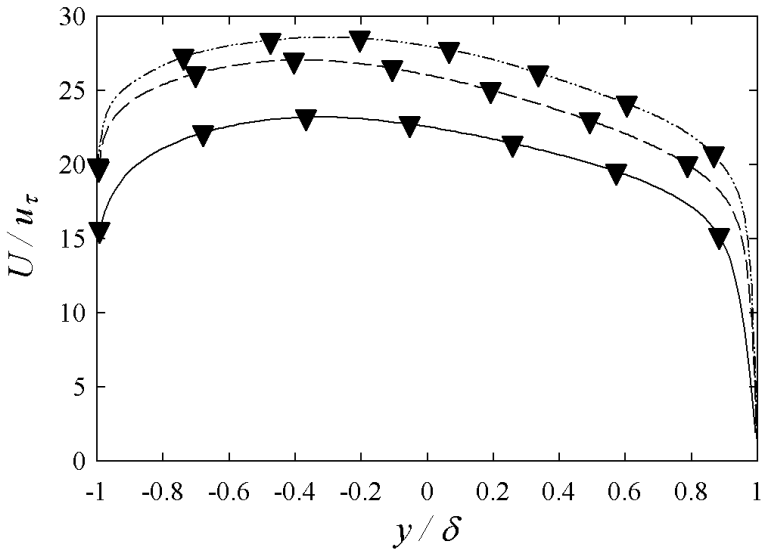

Figure 5.11. Comparison of bulk velocity profiles for $30\mu m - 90\mu m$ posts for $Re_\tau \approx 180$ (–), $Re_\tau \approx 395$ (– –), and $Re_\tau \approx 590$ (– ·· –).

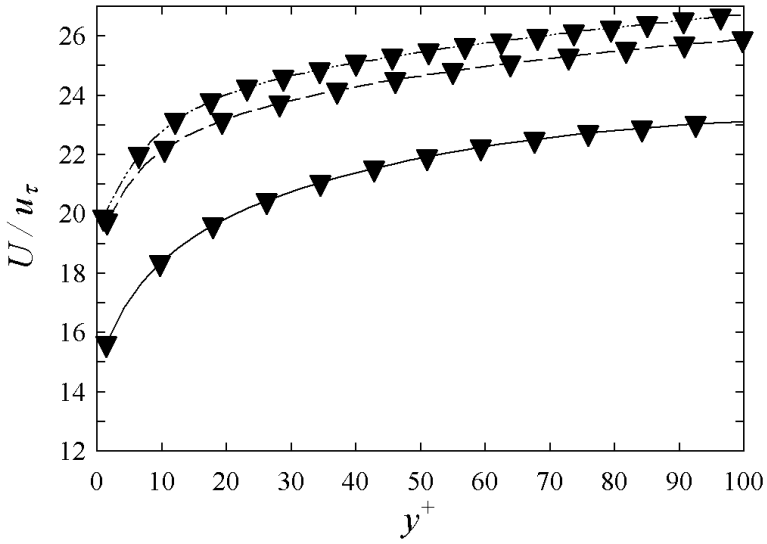

Figure 5.12. A close look at the velocity profiles for $30\mu m - 90\mu m$ posts near the SHS and plotted against wall units y^+.

In Figure 5.11, the slip velocity of the $Re_\tau \approx 590$ case is close to that of the $Re_\tau \approx 395$ $30\mu m - 90\mu m$ post case, perhaps because the simulation has not yet reached steady state. Slip velocities near the mean (bulk) velocity are present at the three Reynolds numbers considered. Velocity profile asymmetry remains fairly consistent for all three Reynolds numbers, with peak velocities shifted toward the SHS. In Figure 5.12, the profiles look nearly identical, and simply shifted upwards with increased friction Reynolds number. The $Re_\tau \approx 590$ case is the noted exception, and that difference is most likely due to the simulation not yet reaching steady state. Note that the location of the grid point closest to the SHS changes slightly across the Reynolds numbers shown. This is due to the differences in resolution across the simulations.

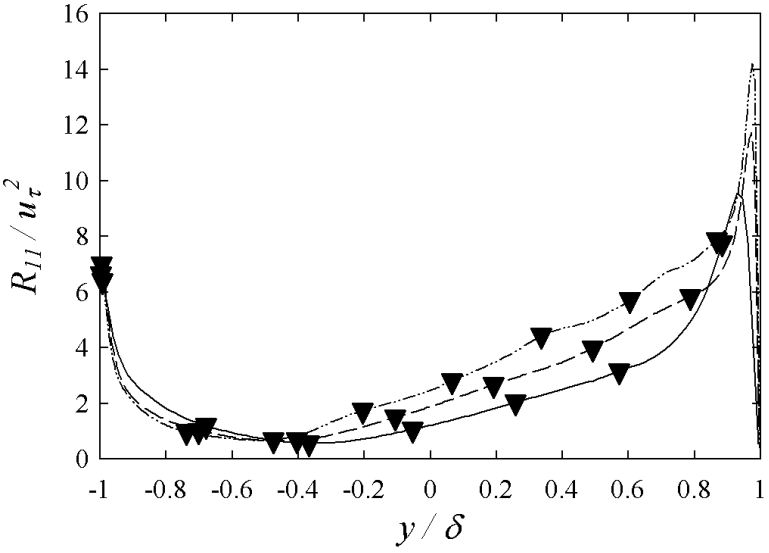

Figure 5.13. Comparison of R_{11} profiles for $30\mu m - 90\mu m$ posts.

In Figure 5.13, the cases with $Re_\tau \approx 395$ and $Re_\tau \approx 590$ have peaks much higher and closer to the upper wall than the $Re_\tau \approx 180$ case. Also note the complete absence of peaks at the SHS, with R_{11} values at that wall being nearly identical. Recalling all $30\mu m - 90\mu m$ post cases have R_{11} regions in the upper half of the channel which were

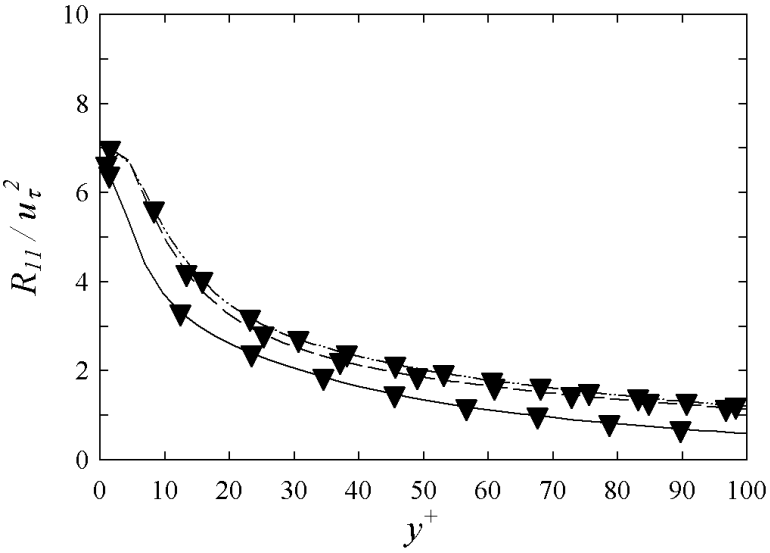

Figure 5.14. Plotting R_{11} against y^+ for $30\mu m - 90\mu m$ posts.

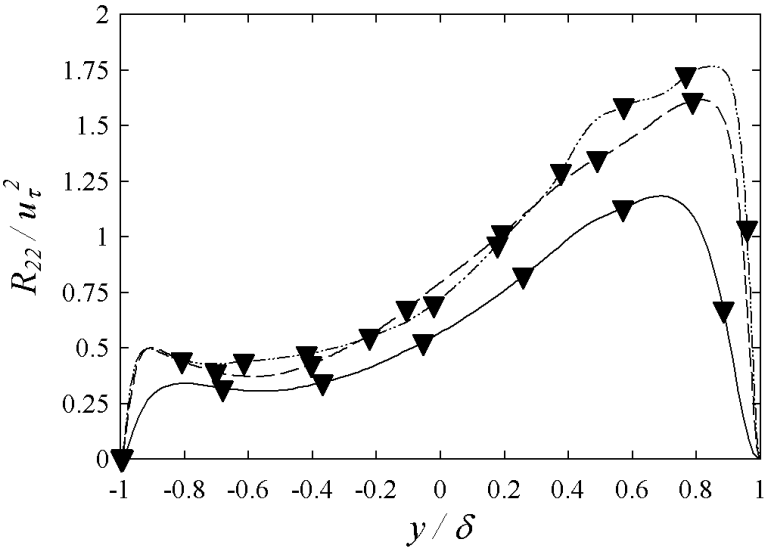

Figure 5.15. R_{22} profiles for $30\mu m - 90\mu m$ posts.

higher than their ridge or smooth wall counterparts, Figure 5.13 clearly shows this trend increases with increased Reynolds number. In Figure 5.14, the shift present between the R_{11} profiles at $Re_\tau \approx 180$ and the two at higher Reynolds numbers is

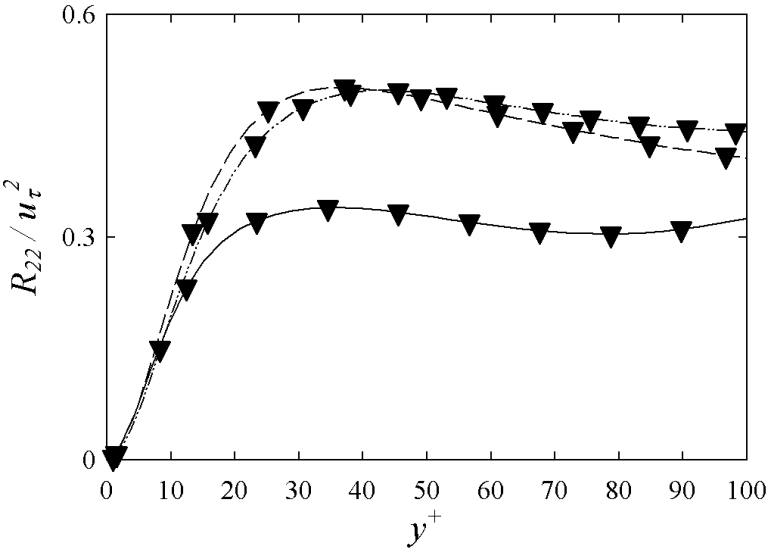

Figure 5.16. R_{22} profiles plotted against y^+ for $30\mu m - 90\mu m$ posts.

quite pronounced, while the $Re_\tau \approx 395$ and $Re_\tau \approx 590$ cases nearly lie atop one another. R_{11} profile peak locations are difficult to compare, as they lie nearly at (or indeed upon) the SHS. Again, for the R_{22} profiles shown in Figure 5.15, the cases at higher Reynolds numbers have peaks much higher than the $Re_\tau \approx 180$ case. As with other cases investigated, R_{22} consistently goes to zero at the walls, and displays noticeable asymmetry. The $Re_\tau \approx 590$ case crosses the $Re_\tau \approx 395$ case several times, which further supports the notion that the case has yet to reach steady state, as the profile crossing is almost certainly not a physical effect. In Figure 5.16, plotting against wall units reveals the R_{22} peak locations to be in roughly the same location. As was the case in Figure 5.15, the $Re_\tau \approx 590$ case clearly crosses the $Re_\tau \approx 395$, which is contrary to previously observed trends and most likely non-physical.

Figures 5.17 and 5.18 show the non-zero R_{33} values at the SHS increase with increased Reynolds number, indicating an increase in the average transverse slip velocity with increasing Reynolds number. Unlike other cases, the R_{33} peaks in Figure 5.18 do not lie in the same vertical location, despite being plotted against y^+. This

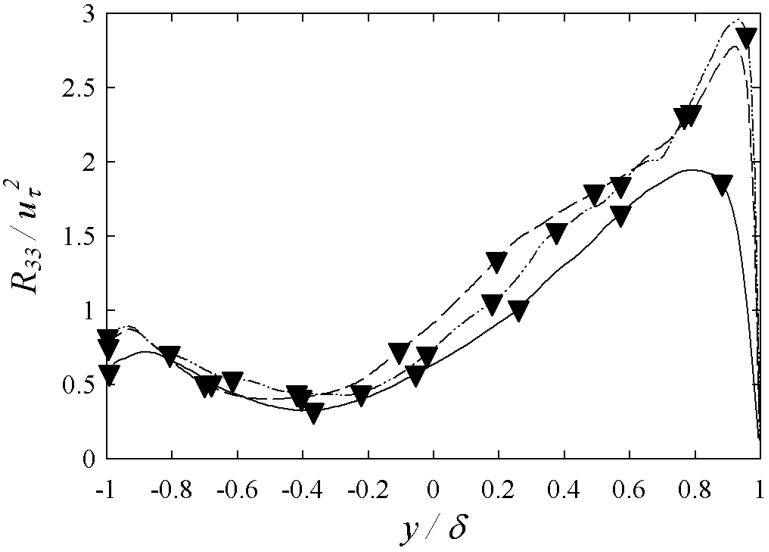

Figure 5.17. R_{33} profiles for $30\mu m - 90\mu m$ posts.

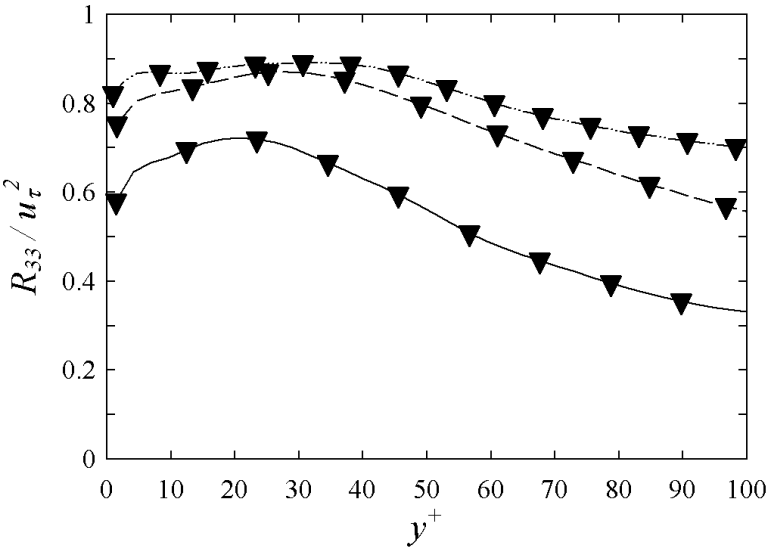

Figure 5.18. A closer look at the R_{33} profiles for $30\mu m - 90\mu m$ posts, near the SHS and plotted against y^+.

may indicate a change in the transverse component of the turbulent structures, or simply an indication of a simulation that is not yet at steady state. The R_{12} profiles in Figure 5.19 indicate that the $Re_\tau \approx 590$ case has yet to reach steady state, as is

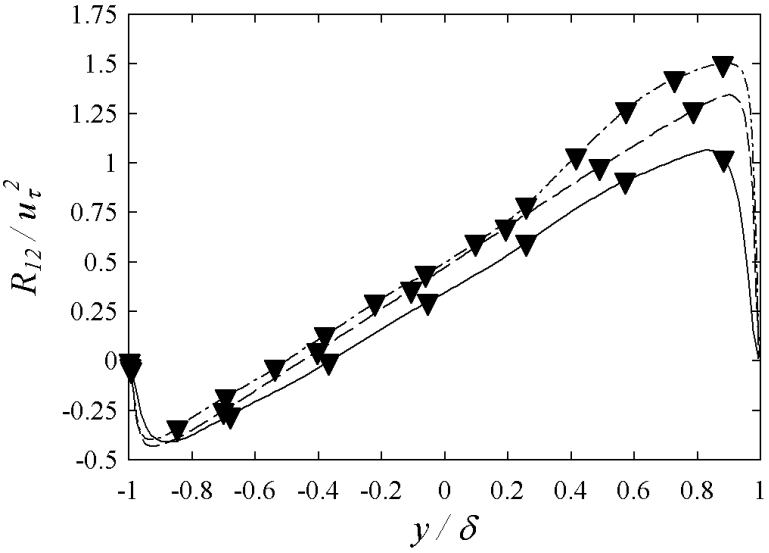

Figure 5.19. R_{12} profiles for $30\mu m - 90\mu m$ posts.

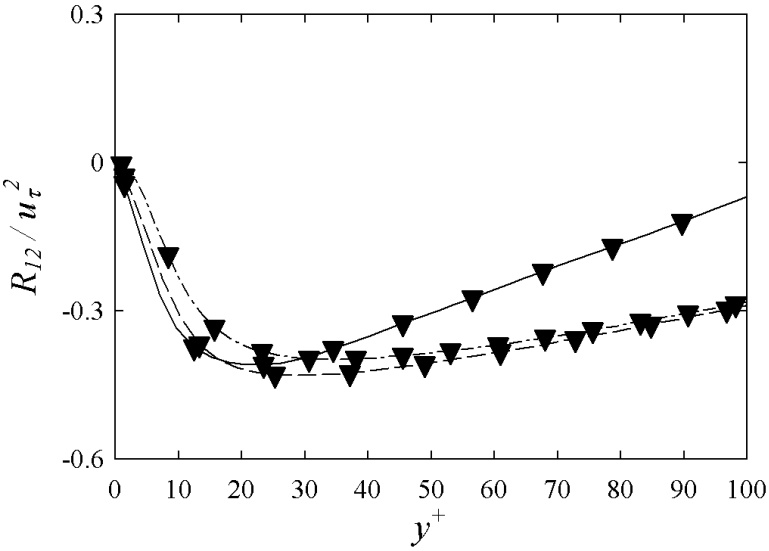

Figure 5.20. A closer look at R_{12} profiles for $30\mu m - 90\mu m$ posts.

evidenced by the nonlinearity of the profile, especially near the channel's center and upper wall. Otherwise, the profiles exhibit the expected shift upward and further loss of symmetry as the Reynolds number increases. Figure 5.20 reveals the different mid-

channel linear region slopes, and similar peak locations near the SHS. Section 5.2.1 has more details on R_{12} normalization and its relation to turbulent structures. The figure also shows the R_{12} profile for the $Re_\tau \approx 180$ case crossing both the $Re_\tau \approx 395$ and $Re_\tau \approx 590$ profiles. In addition, the linear, mid-channel region of the $Re_\tau \approx 180$ case appears to have a slope much greater than those of the other cases. This may be due to the $30\mu m - 90\mu m$ post cases not yet reaching steady state. Other possibilities include low Reynolds number effects present in the $Re_\tau \approx 180$ simulation, or an actual physical phenomenon present in the flow field.

5.1.1.3 Trends in U_{slip} and τ_w for varying SHS Geometries

The slip and drag reduction properties of the SHS as a function of feature width and spacing are summarized in Figures 5.21 and 5.22. Drag reduction performance increases with increased feature spacing. This trend is consistent for both ridges and posts, as the slip velocity attains a maximum nearly 65% of the bulk velocity for ridges, and over 75% of the bulk velocity for posts, with a width to spacing ratio just above $d/w > 0.3$. For ridge width to spacing ratios $d/w = 1$, more slip is achieved with larger micro-feature widths and gaps. This is clearly seen in Figure 5.21, where the slip velocity for $15\mu m - 15\mu m$ ridges is nearly 40% lower than the slip velocity for the $30\mu m - 30\mu m$ ridges. A similar trend for the drag reduction is found in Figure 5.22, where the bottom wall shear stress reduction for the $15\mu m - 15\mu m$ ridges is nearly 30% lower than that for $30\mu m - 30\mu m$ ridges. This is consistent with the observations made by [34].

Experimental data from [11] observes similar trends for features with identical d/w ratios but different sizes ($15\mu m - 15\mu m$ versus $30\mu m - 30\mu m$ ridges for simulations, and $30\mu m - 30\mu m$ versus $60\mu m - 60\mu m$ ridges for experimental data), where thinner feature widths and gaps show less drag reduction and lower slip velocities (see Figures 5.21 and 5.22). This indicates that the actual size of the features, and not simply the

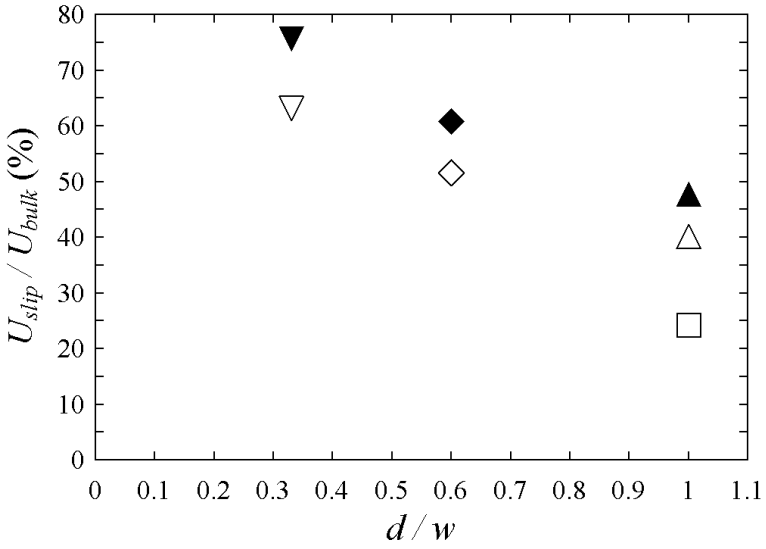

Figure 5.21. Slip velocity as a percentage of bulk velocity for all $Re_\tau \approx 180$ cases: ridges of width and gap $15\mu m - 15\mu m$ (□), $30\mu m - 30\mu m$ (△), $30\mu m - 50\mu m$ (◊), and $30\mu m - 90\mu m$ (▽), with posts of width and gap $30\mu m - 30\mu m$ (▲), $30\mu m - 50\mu m$ (♦), and $30\mu m - 90\mu m$ (▼). Slip velocity increases with increased SHS feature spacing.

ratio of width to spacing (or the percentage of shear-free surface on the SHS), plays an important role in the surface's drag-reduction. Smaller features lead to diminished drag-reduction performance. Also note the close agreement with $30\mu m - 30\mu m$ ridge data from Daniello *et al.* [11] (☆) at the same Reynolds number superimposed over the simulation data in Figure 5.22, which shows the same shear stress reduction as predicted by simulation. Small differences in wall shear stress reduction may be attributed to experimental error or the slight disparity between the geometries employed in the experiments and simulations. When comparing posts and ridges, it is clear that for a given ratio of micro-feature size to spacing, d/w, posts yield higher slip velocities and larger shear stress reductions. The performance advantage of posts over ridges appears to increase with increased feature spacing.

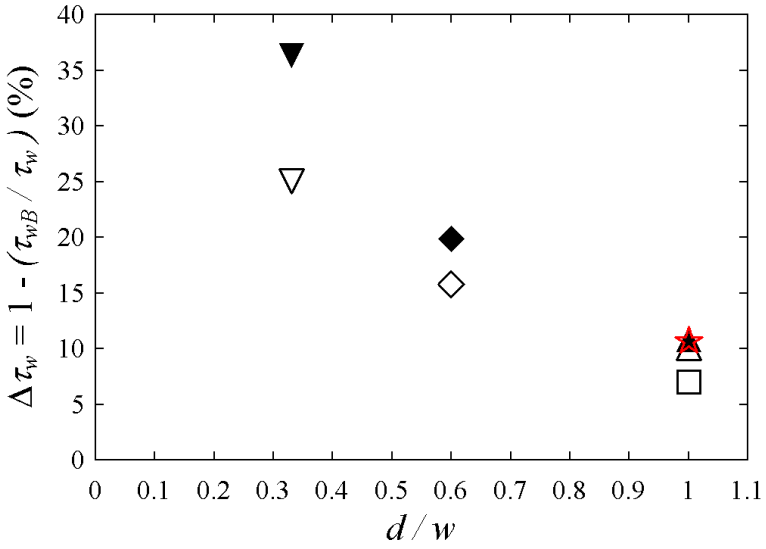

Figure 5.22. SHS (bottom wall) shear stress reduction as a function of SHS feature width and spacing for the same cases presented in Figure 5.21. Shear stress decreases with increased feature spacing, indicating SHS perform better at larger spacing w. Note that experimental data from Daniello *et al.* [11] is denoted by ☆.

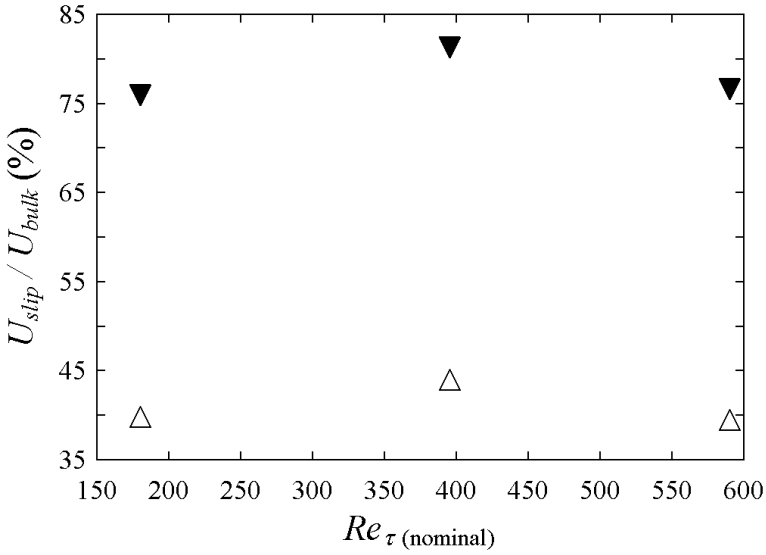

Figure 5.23. Slip velocity as a percentage of bulk velocity for $30\mu m - 30\mu m$ ridges (△) and $30\mu m - 90\mu m$ posts (▼) at $Re_\tau \approx 180, 395,$ and 590.

5.1.1.4 Trends in U_{slip} and τ_w for varying Re_τ

In Figure 5.23, slip velocity normalized by the channel bulk velocity increases between $Re_\tau \approx 180$ and $Re_\tau \approx 395$, but then decreases again at $Re_\tau \approx 590$. This is most likely due to the $Re_\tau \approx 590$ case not yet being at steady state. Further simulations may reveal that normalized slip velocity continues to increase with increased Reynolds number.

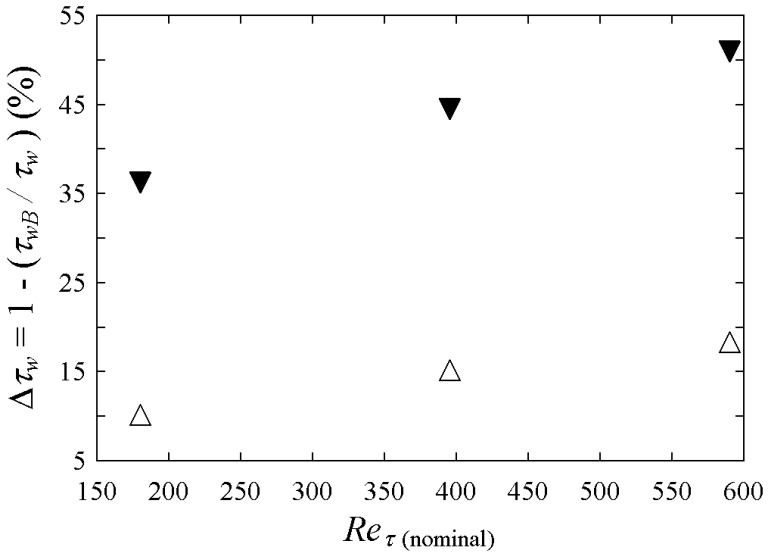

Figure 5.24. SHS shear stress reduction as a function of friction Reynolds number for $30\mu m - 30\mu m$ ridges (△) and $30\mu m - 90\mu m$ posts (▼).

Unlike the slip velocity trends shown in Figure 5.23, Figure 5.24 shows that wall shear stress reduces (reduction increases) as Re_τ increases. It appears that wall shear stress in the $Re_\tau \approx 590$ case is not affected by a lack of steady state in the simulation or the slightly lower slip velocity at the SHS. This clearly indicates that turbulent drag reduction over an SHS ($30\mu m - 30\mu m$ ridges and $30\mu m - 90\mu m$ posts, in this case) is dependent upon, and increases with, Reynolds number, but not as drastically as it depends upon feature spacing. Further investigations at both higher and lower

Reynolds numbers may show a continued linear relationship between SHS performace and Reynolds number.

5.2 Turbulent Structures

5.2.1 R_{12} Normalization

Figures 4.14, 4.20, and 4.26 suggest that the essential scaling properties of turbulent boundary layers remain intact even when an SHS is present and significant drag reduction is occurring for that boundary layer. In those figures, $u^+ = \frac{U_{slip}}{u_\tau} + y^+$ to within 10% for all the cases considered. For this result it was important to scale with the local boundary shear stress. Figures 5.25 and 5.26 investigate if this scaling holds for the turbulence as well as the mean flow. These figures show R_{12} profiles for all seven cases investigated scaled by the top and bottom wall shear stress, respectively. The profiles all collapse onto the standard channel flow profile near the top and bottom wall (SHS), suggesting that the structure of the near-wall turbulence has not fundamentally changed. It is not surprising that this scaling is present at the top (smooth) wall. The presence of such scaling at the SHS, however, is not obvious.

When normalized appropriately, the R_{12} profiles in Figure 5.26 collapse to the standard channel profile near the bottom wall, and continue to suggest that the structure of the near-wall turbulence may not be much different from that in a standard channel. The R_{12} profiles in Figure 5.27 collapse to the standard channel profile near the bottom wall for the $Re_\tau \approx 395$ cases investigated, also suggesting that the structure of the near-wall turbulence (at the SHS) has not changed. This is another non-obvious result, and suggests structures, although shifted toward the SHS, may not be much different from those in a standard channel. The collapse is less prominent than the $Re_\tau \approx 180$ cases but is still present. As with the previous cases, the R_{12} profiles at $Re_\tau \approx 590$ shown in Figure 5.28 collapse to the standard channel profile near the bottom wall. As with the $Re_\tau \approx 395$ cases, the collapse occurs up to the

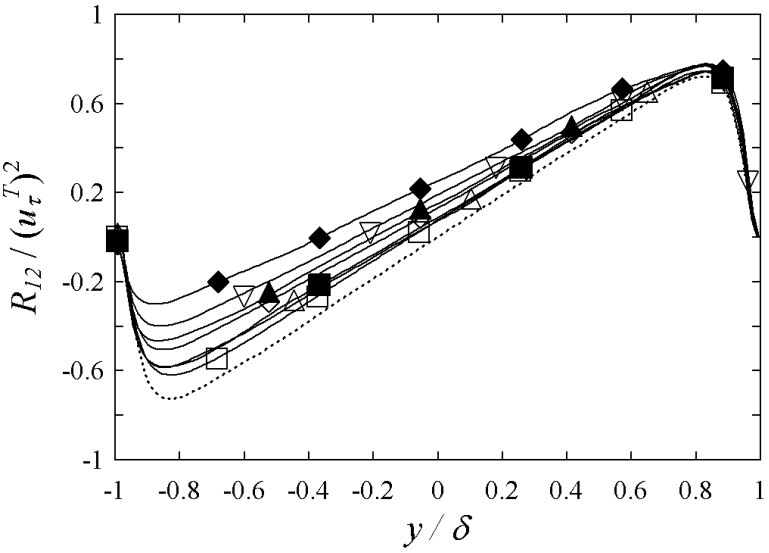

Figure 5.25. R_{12} profiles for all $Re_\tau \approx 180$ cases normalized by the square of the top wall shear stress u_τ^T. Symbols are consistent with those presented in Table 3.2.

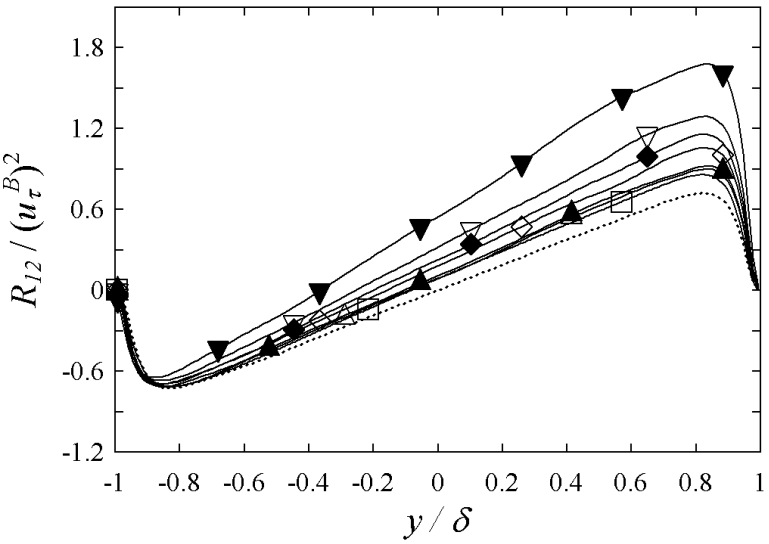

Figure 5.26. R_{12} profiles for all $Re_\tau \approx 180$ cases normalized by the square of the bottom wall shear stress u_τ^B.

peak R_{12}.. The presence of the collapse for all geometries at all Reynolds numbers

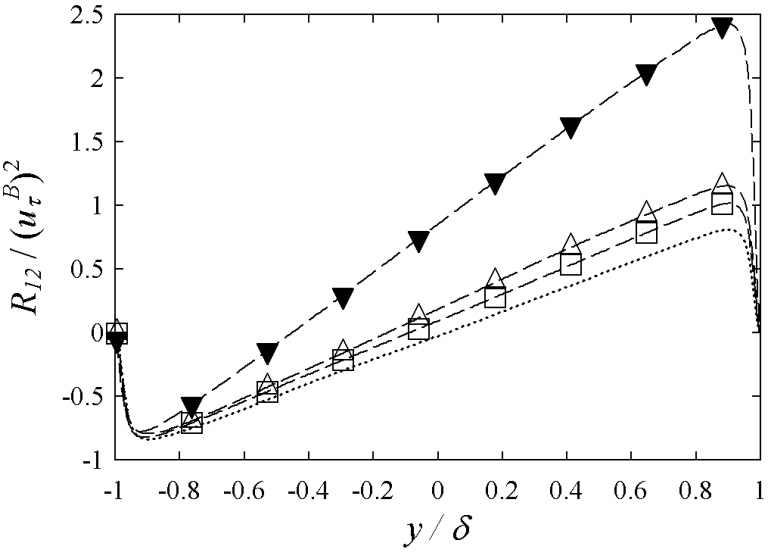

Figure 5.27. R_{12} profiles for all $Re_\tau \approx 395$ cases normalized by the square of the bottom wall shear stress u_τ^B.

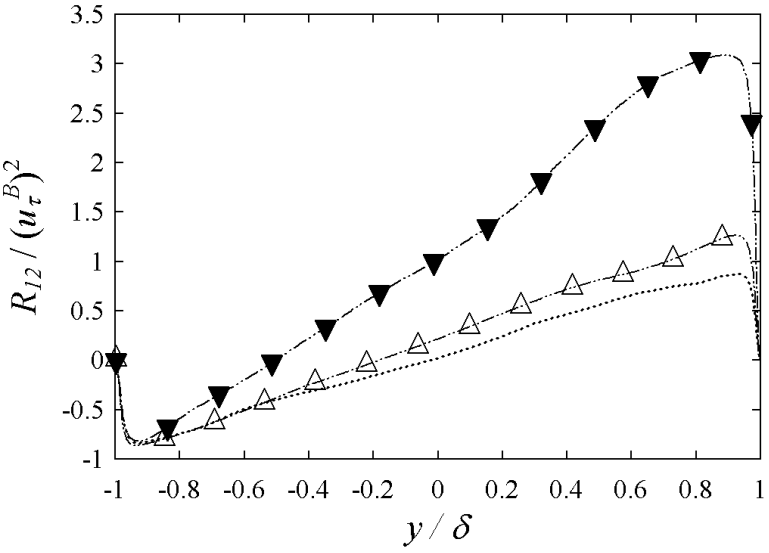

Figure 5.28. R_{12} profiles for all $Re_\tau \approx 590$ cases normalized by the square of the bottom wall shear stress u_τ^B.

indicates the turbulent structures are shifted (due to the different $u_{\tau B}$ values), but otherwise unaffected, for all cases examined in this study.

5.2.2 Turbulent Structure Sizes in $Re_\tau \approx 180$ Simulations

For $30\mu m - 30\mu m$ ridges at $Re_\tau \approx 180$,, vortex pairs are roughly 50^+ wide, a ridge-gap combination is 67.5^+ wide, and the channel 540^+ wide. Note that there are eight ridge-gap combinations across the channel. In this case, a vortex pair may spans slightly less than one ridge-gap combination. At this Reynolds number, ridges are on the same scale as riblets (see [10]), and the turbulent streaks are roughly the same scale. Despite the similar scales, it can be argued that the SHS do not act as riblets for any feature sizing or Reynolds number. First and foremost, posts are physically different from riblets in that they allow a large transverse slip velocity, allow for non-zero slip velocity down stream ("slip-streaming"), and of course support an air-water interface, which riblets do not. In the same vein, ridges support an interface, and thus physically differ from riblets. Most importantly, both ridges and posts appear to outperform the drag reducing properties of riblets and are not restricted to a specific Reynolds number (see Choi, *et al.* [10]).

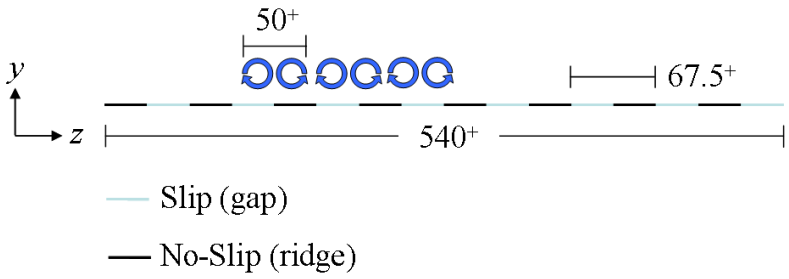

Figure 5.29. A schematic representing pairs of counterrotating vortices for channel flow at $Re_\tau \approx 180$ with $30\mu m - 30\mu m$ ridges. Here, the feature spacing is 33.75^+, which is more than half of the vortex pair width.

Due to slip, the streamwise velocities appear to be closer to the SHS than their counterparts in a standard channel. Figure 5.31 shows that the near-wall velocity of the post case is much higher than that of the ridge case, at the same distance from the wall and same Reynolds number. In addition, the structures appear to be quite

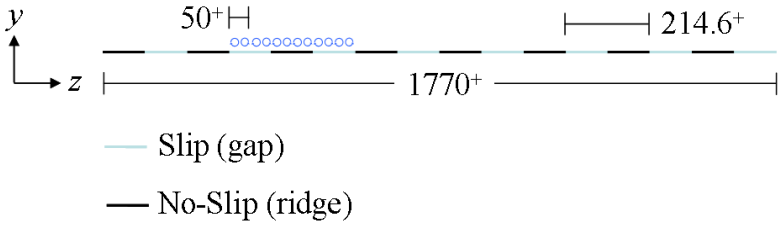

Figure 5.30. A schematic representing pairs of counterrotating vortices for channel flow at $Re_\tau \approx 590$ with $30\mu m - 30\mu m$ ridges. The feature spacing for this channel is 107.3^+, which is more than twice the pair width.

different. This indicates that the turbulent structures have moved, seeming closer to the SHS as the slip velocity for the $30\mu m - 90\mu m$ posts (at the same vertical location) is larger than that at the $30\mu m - 30\mu m$ ridges.

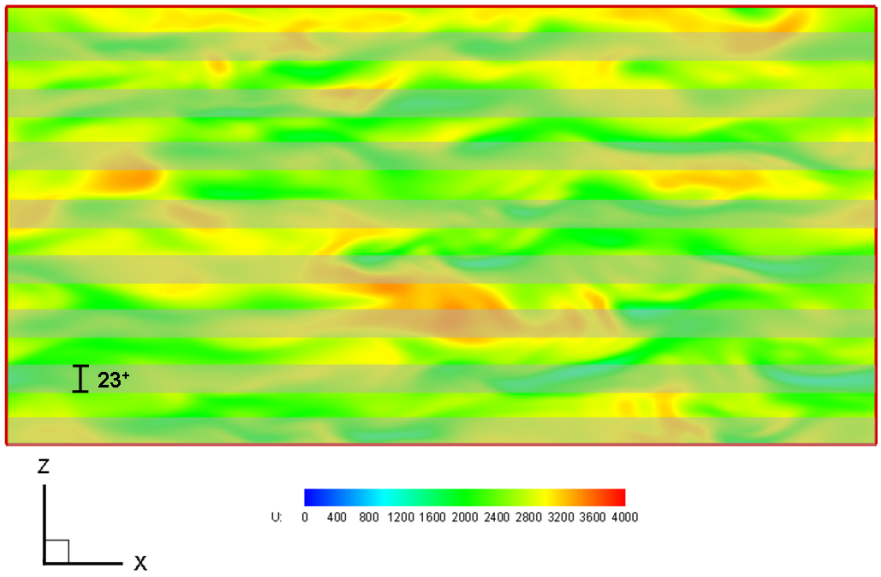

(a) $30\mu m - 30\mu m$ ridges.

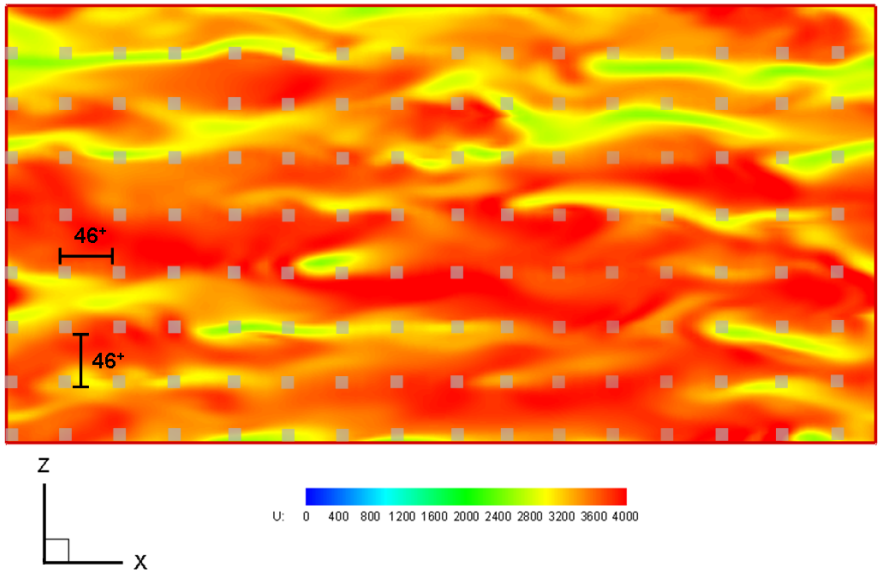

(b) $30\mu m - 90\mu m$ posts.

Figure 5.31. Approximate ridge and post locations superimposed over a slice of instantaneous streamwise velocity showing feature size and spacing in plus units. Contours are colored by streamwise velocity, have the same scale, and are taken at the same vertical location (in y^+).

5.2.3 Smooth and $30\mu m - 30\mu m$ Ridge Channel Structures

Instantaneous velocity and pressure fields were extracted from two statistically steady simulations both at a friction Reynolds number $Re_\tau \approx 180$ with 128^3 grid points. One simulation (the $Re_\tau \approx 180$ benchmark) has smooth, no-slip walls. The second, the $30\mu m - 30\mu m$ ridge channel, was allowed to run for numerous flow-through times after it was determined to be at steady state in order to establish persistent, identifiable turbulent structures. The streamwise velocity fields were scaled by the bulk velocity (which varied for each case). Horizontal planar slices (XZ) were taken at $y^+ \approx 21$ and $y^+ \approx 12$ for the smooth and ridged cases, respectively. Different vertical locations were chosen in an attempt to determine whether the locations of the turbulent structures were shifted by a fixed amount (when compared to the non-SHS channel). In this case, the two locations were determined by matching the planar-averaged velocity derivative (essentially the shear stresses), as the kinematic viscosity is equal to unity in all $Re_\tau \approx 180$ cases), noting the locations of this parity, and taking slices at those locations.

A single streak was identified, and is roughly the expected width of 50^+ units (see Figure 5.29) for a channel at this friction Reynolds number. For both geometries, the feature characteristics are similar, once again supporting the notion that turbulent structures are not fundamentally altered by the presence of the SHS. Figure 5.33 shows XZ planar slices of non-normalized instantaneous vertical velocity, similar to the streamwise slices shown in Figure 5.32. The vertical velocity features clearly show the presence of a streamwise vortex which is roughly 50^+ units wide, as expected. Again, the structures for the smooth and SHS channels are shifted but otherwise similar.

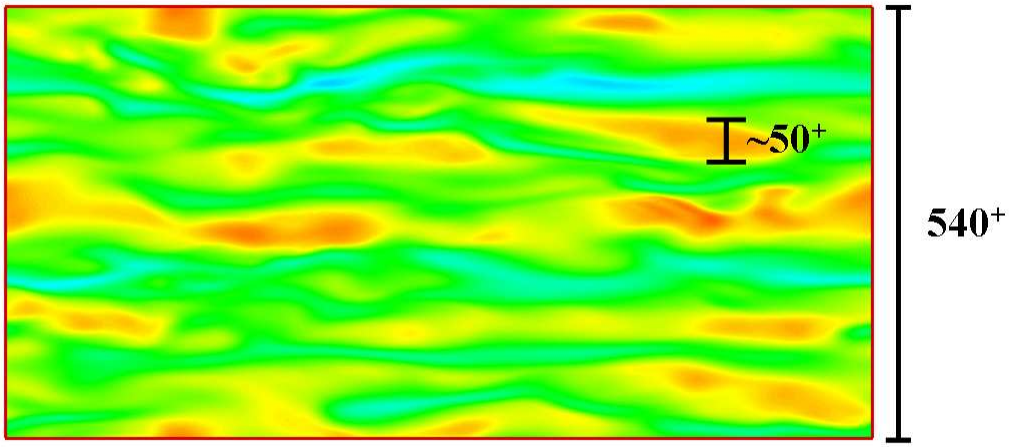

(a) Smooth (non-SHS) channel.

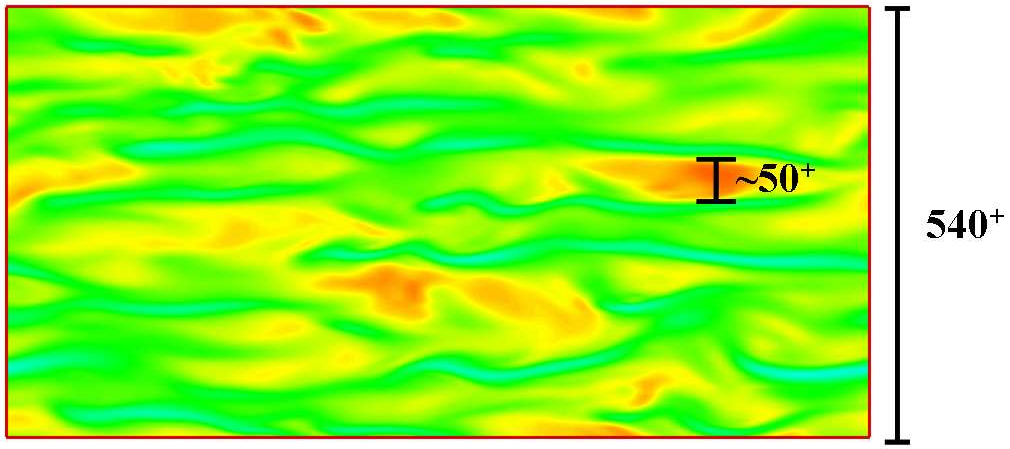

(b) $30\mu m - 30\mu m$ ridges.

Figure 5.32. Instantaneous streamwise velocity contour slices (XZ), normalized by U_{bulk}, for a smooth channel and one with $30\mu m - 30\mu m$ ridges. The slice in (a) is taken at $y^+ \approx 21$, while the slice in (b) is taken at $y^+ \approx 12$. Feature sizes and shapes are roughly equivalent.

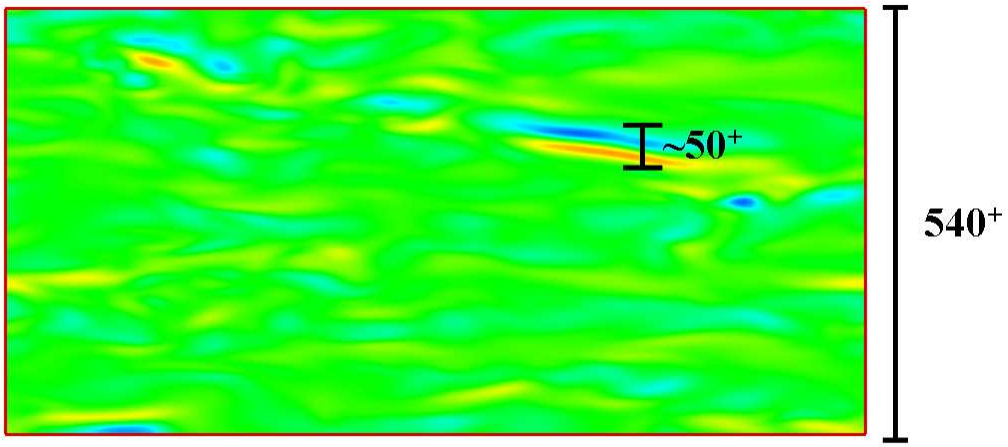

(a) Standard (non-SHS) channel.

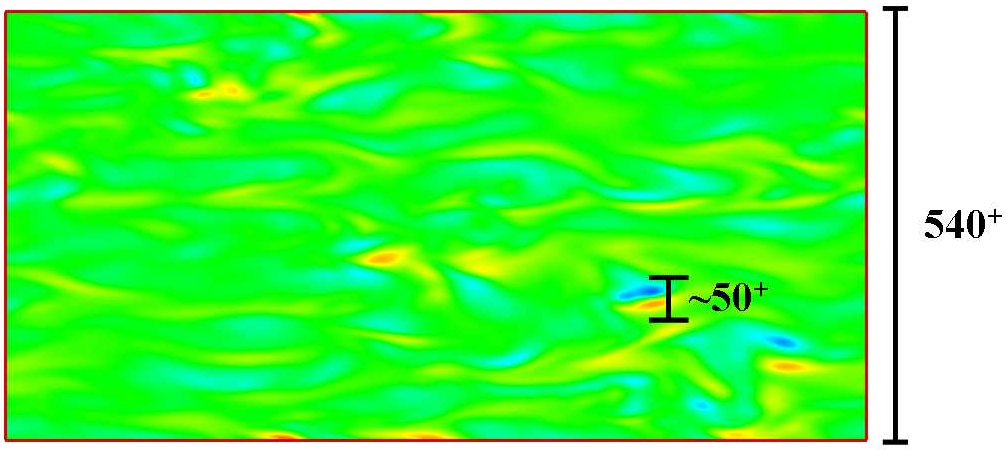

(b) $30\mu m - 30\mu m$ ridges.

Figure 5.33. Instantaneous vertical velocity contour slices (XZ), similar to those found in Figure 5.32, for the same geometries (from the same simulations). The slice in (a) is taken at $y^+ \approx 21$, while the slice in (b) is taken at $y^+ \approx 12$. Again, feature sizes and shapes are roughly equivalent.

5.3 Conclusions

Superhydrophobic surfaces affect changes in turbulent channel flow through several different mechanisms. First and foremost, they admit average slip velocities (along the SHS) up to 80% of the channel bulk velocity, with the possibility of being even higher when the unfinished $Re_\tau \approx 590$ $30\mu m - 90\mu m$ post simulation reaches steady state. Second, shear stress at the SHS (which can be directly related to drag reduction) is lowered by upwards of 50% when compared with non-SHS channel flow, and the shear stress reduction of 10% found for $Re_\tau \approx 180$ $30\mu m - 30\mu m$ ridges closely matches drag reduction found by the experiments of Daniello *et al.* [11] for the same geometry and Reynolds number. In addition, the SHS alters the symmetry, peak magnitude, and peak locations of Reynolds stresses, which is not surprising considering the presence of a significant slip velocity and a reduction in the SHS wall shear stress.

For all geometries investigated at all Reynolds numbers, posts outperformed ridges by supporting a higher slip velocity and exhibiting greater decreases in wall shear stress. A comparison of posts and ridges at various spacing (Figures 5.21 and 5.22) most clearly display this, for ridges and posts of equal width and spacing. Closely tied to this is the relationship between the width to gap (d/w) ratio of the microfeature and the drag reducing performance of the surface. A decrease in this ratio leads to an increase in slip velocities and a decrease in SHS wall shear stress for both ridges and posts. Interestingly, this behavior does not persist if the width to gap ratio is fixed but the features themselves made to be smaller (or the channel higher; the effect is identical). For thin $15\mu m - 15\mu m$ ridges with a width to gap ratio of unity, the slip velocity was nearly half that of $30\mu m - 30\mu m$ ridges, and the shear stress reduction 5% less than that found for the $30\mu m - 30\mu m$ ridges. This clearly shows that the spacing and width of the microfeatures, and not simply the ratio of the two, plays a vital role in the performance of the surface. Trends in Reynolds number

are less pronounced. The slip velocity trends as a function of Reynolds number (for $30\mu m - 30\mu m$ ridges and $30\mu m - 90\mu m$ posts) are inconclusive as the $Re_\tau \approx 590$ has yet to reach steady state, and has a lower slip velocity than the $Re_\tau \approx 395$ case for both geometries studied. Slip velocity increases for both cases with an increase from $Re_\tau \approx 180$ to $Re_\tau \approx 395$. The wall shear stress reduction trends are more definitive, as, for the same feature geometry, drag reduction increases with increased Reynolds number. Further simulations at other Reynolds numbers could further confirm the wall shear stress reduction trend observed.

Turbulent structures in the channel are affected by the superhydrophobic surface, as is evidenced by the changes in Reynolds stresses and velocity profiles that occur when an SHS is introduced to turbulent channel flow. Examination of scaled R_{12} profile collapse, and of instantaneous streamwise and vertical velocity fields, indicates that the turbulent structures remain intact, and are simply shifted toward the SHS. This is useful, as it means the existing theory and understanding of turbulent structures still applies to turbulent channel flow over SHS, and simply requires the turbulent structure locations to be modified. An understanding of this shift allows engineers to model and predict the performance of SHS in many different applications without the time and expense of performing DNS or experimental trials.

5.4 Summary

DNS of SHS

For the first time, direct numerical simulations of superhydrophobic surfaces were performed. This enabled an investigation of the fundamental physics of turbulent drag reduction using SHS without the use of turbulence models or assumed slip lengths or velocities. The microfeatures and all relevant scales were well resolved in the simulations performed.

Temporal and Ensemble Averaging

A unique method of gathering velocity and pressure statistics was devised which allowed the average effect of the SHS to be observed, as well as instantaneous velocity fields to be used for feature identification. This method was written to minimize the amount of data stored in memory and written to disk at each sampling period.

Multiple Feature Sizes and Spacings

A variety of feature sizings and spacings were investigated in order to determine the effect of feature and gap width on the performance of the SHS. It was determined that, at a given Reynolds number, increased feature spacing w leads to a higher slip velocity and increased drag reduction. In addition, it was discovered that the ratio of feature width to spacing $\frac{d}{w}$ was not the only factor in determining drag reducing performance, as $15\mu m - 15\mu m$ ridges with $\frac{d}{w} = 1$ performed poorly when compared to $30\mu m - 30\mu m$ ridges (also with $\frac{d}{w} = 1$).

Multiple Reynolds Numbers

Ridges and posts were investigated at three Reynolds numbers. It was determined that drag reduction scales with Reynolds number: for the same $30\mu m - 30\mu m$ ridges, wall shear stress reduction was nearly 30% higher for the $Re_\tau \approx 590$ case than was observed for the $Re_\tau \approx 180$ case, despite the drastic differences in turbulent structure sizes.

Turbulent Structures

Turbulent structures were identified in $30\mu m - 30\mu m$ ridge case at $Re_\tau \approx 180$. They were of expected size (roughly 50^+ wide) and arrangement. It appears that the

nature of the structures is not fundamentally altered by the presence of SHS, but the locations of the structures is simply shifted toward the SHS.

Supercomputers

It was determined that, if one is able to use over 1,000,000 CPU hours on a government supercomputer in roughly two fiscal years, and willing to send multiple faxes and emails to the Department of Defense every month reassuring them that one is not trying to use the supercomputer to overthrow the United States government, then one may, in fact, be able to complete direct numerical simulations of turbulent channel flow up to $Re_\tau \approx 590$ with meshes exceeding 134,217,728 grid points in a reasonable amount of time, assuming one ensures proper placement of "*" when using "rm -rf".

APPENDIX A

THE CONJUGATE GRADIENT ALGORITHM

The conjugate gradient (CG) algorithm is employed as the sparse matrix solver in the code. A more thorough explanation of this method can be found in [43]. The CG method is well suited for solving systems of the type

$$Ax = b \tag{A.1}$$

The unknown, x, is solved from the matrix A and its solution b. A must be positive definite and symmetric in order for CG to robustly invert the system. The conjugate gradient method is closely related to the method of steepest descent, which involves two steps: choosing a descent direction, and then finding the local minimum in that chosen direction. When specifying a descent direction, it is easy to visualize being on a hill, with the intent of finding the lowest point in the valley below (i.e. the minimum, or solution). The method does not know where the point is located, but it knows the point does not lie above it, thus is must descend. The method chooses the direction which sends it downward by way of steepest descent. Once it gets to the lowest point on that plane, it then searches and chooses the next direction of greatest descent rate, and goes in that direction. This process continues until the solver reaches the lowest possible point. This is the solution for x. CG has the added benefit of never searching in the same direction twice, which can lead to faster convergence. The CG algorithm requires an initial matrix A and a guess solution for x, x_0. The algorithm solves for the initial residual:

$$r_0 = b - Ax_0 \tag{A.2}$$

A preconditioner P is applied to the initial residual to get the initial search direction, z_0:

$$z_0 = Pr_0 \tag{A.3}$$

The initial minimization direction p_0 is set to the initial search direction, as a first guess:

$$p_0 = z_0 \tag{A.4}$$

The residual is dotted with the search direction to calculate $\eta_0 = r_0 \cdot z_0$, which is an indicator of convergence of the algorithm. η can be defined in terms of the residual and the minimizing direction, which can in turn be defined in terms of the known matrix A and some unknown error, e.

$$\eta = r^T Pr \tag{A.5}$$

$$\eta = eA^T PAe \tag{A.6}$$

$$\eta \approx eAe \tag{A.7}$$

if $PA \approx I$, the identity matrix. In Equation A.5, the definitions of r and z are employed. In Equation A.6, the residual r is rewritten in terms of some unknown error multiplied by the known matrix, from the definition of the residual. Finally, in Equation A.7, it is assumed that P is a relatively good approximate inverse, thus $A^T P = 1$, leaving eAe. Thus, η is not the error, but is a measure of it, in that $\eta < ||A||\ ||e||^2$. For convenience, this will be referred to as the error.

The algorithm loops until the error has fallen below a predetermined error (absolute convergence), the *change* in the residuals has fallen below a set tolerance (relative convergence), or the maximum number of iterations has been exceeded (something went wrong). Inside the CG loop, the search direction p_i and matrix A are multiplied to calculate w_i. The minimization direction is dotted with this to yield $\delta_i = p_i \cdot w_i$, which is used as an intermediate variable. The variable $\alpha = \frac{\eta_i}{\delta_i}$ is calculated. Using orthogonality properties, it can be shown that

$$\alpha = \frac{r_i \cdot p_i}{p_i \cdot w_i} \tag{A.8}$$

Note that the numerator of α in Equation A.8 is $r_i \cdot p_i$, rather than $r_i \cdot z_i$. It can be shown that the two are equivalent by using the equation which updates the minimizing direction (see Equation A.14):

$$p_{i+1} = z_{i+1} + \beta_{i+1} p_i$$

$$r_{i+1} \cdot p_{i+1} = r_{i+1} \cdot z_{i+1} + r_{i+1} \cdot \beta_{i+1} p_i \tag{A.9}$$

$$r_{i+1} \cdot p_{i+1} = r_{i+1} \cdot z_{i+1} + 0 \tag{A.10}$$

$$r_{i+1} \cdot p_{i+1} = r_{i+1} \cdot z_{i+1}$$

In Equation A.9, all terms are dotted with the residual r_{i+1}. In Equation A.10, the fact that $r_{i+1} \cdot p_i = 0$ is employed. This is proven below (Equations A.12 and A.13). The variable α is used in the next step, which updates the solution with the old solution and a multiple of the minimizing direction:

$$x_{i+1} = x_i + \alpha p_i \tag{A.11}$$

The new residual is calculated $r_{i+1} = r_i - \alpha w_i$. Note that the use of α ensures that the new residual r_{i+1} (or w_{i+1}) is orthogonal to all previous search directions:

$$
\begin{aligned}
r_{i+1} &= r_i - \alpha w_i \\
r_{i+1} \cdot p_i &= r_i \cdot p_i - \alpha \left(w_i \cdot p_i \right) && \text{(A.12)} \\
r_{i+1} \cdot p_i &= r_i \cdot p_i - \left(\frac{r_i \cdot p_i}{p_i \cdot w_i} \right) \left(w_i \cdot p_i \right) && \text{(A.13)} \\
r_{i+1} \cdot p_i &= r_i \cdot p_i - r_i \cdot p_i \\
r_{i+1} \cdot p_i &= 0
\end{aligned}
$$

This shows that α has taken the "best step" possible along the search direction p_i. Left alone, the use of α to update the new minimizing direction p_{i+1} would results in the steepest descent method, not conjugate gradient. Note that in Equation A.12, all terms were dotted with the current minimizing direction p_i, and in Equation A.13, the definition of α (from Equation A.8) was applied.

If the algorithm has not converged (or reached the maximum number of allowed iterations), the code updates the search direction $z_{i+1} = Pr_{i+1}$, updates η with the new residual and new search direction, $\eta_{i+1} = r_{i+1} \cdot z_{i+1}$, and the ratio of the old and new η terms is calculated and saved as $\beta_{i+1} = \frac{\eta_{i+1}}{\eta_i}$, which actually guarantees the new minimizing direction is conjugate to the previous. The new minimizing direction is calculated:

$$
p_{i+1} = z_{i+1} + \beta_{i+1} p_i \qquad \text{(A.14)}
$$

Using Equation A.14, it can be shown that the use of β ensures orthonormality to $A \cdot p_i$ and not simply p_i, which results from defining $\beta = \frac{z_{i+1} A p_i}{p_i A p_i}$, which is equivalent to the previous definition (see [43] for more details). It is important to note that $p_i \cdot A p_k = 0$ for *all* $k < 1$ (see [43]), meaning that the new search direction is not only to the previous search direction, but to *all* past search directions. After p_{i+1} is calculated, the loop starts again and continues until convergence is reached.

The iterative CG algorithm is popular, as direct methods tend to have much higher memory requirements $O(N^2)$ and cost $O(N^3)$, with N being the number of unknown present in the system to be solved, and thus are imossible to use for the problems tackled in this work. In theory, CG will converge in N iterations. In reality (as is the case in this code), the algorithm tends to converge much more rapidly, on the order of $N^{\frac{1}{3}}$ iterations in three dimensions. The answer CG returns after N iterations tends to be totally corrupted by round-off error for $N > 1000$. The entire CG algorithm, adapted from [43]:

$r_0 = b - Ax_0$
$z_0 = Pr_0$
$p_0 = z_0$
$\eta_0 = r_0 \cdot z_0$
for $i = 0, 1, \ldots$ **do**
  $w_i = Ap_i$
  $\delta_i = p_i \cdot w_i$
  $\alpha = \eta_i / \delta_i$
  $x_{i+1} = x_i + \alpha p_i$
  Exit if converged
  $r_{i+1} = r_i - \alpha w_i$
  $z_{i+1} = Pr_{i+1}$
  $\eta_{i+1} = r_{i+1} \cdot z_{i+1}$
  $\beta_{i+1} = \eta_{i+1} / \eta_i$
  $p_{i+1} = z_{i+1} + \beta_{i+1} p_i$
end

APPENDIX B

DETAILS ON REYNOLDS STRESSES

Section 2.5.3 introduced Reynolds stresses, and gave a brief explanation of how they are calculated and used to analyze the nature of the turbulent flow results produced by the DNS code. This Appendix will provide a more detailed look at the derivation of the Reynolds stresses. Pope [41] presents a thorough look at the theory behind, and mathematics of, Reynolds stresses.

Various statistical quantities, such as the probability density function (PDF), two point correlations, and ensemble averages, are used to analyze the instantaneous velocity fields produced by turbulent flows. Although useful, it is often difficult to find a means of predicting the behavior of these qualities as they evolve. This can be achieved by employing *Reynold's decomposition*, where the mean velocity $\langle \boldsymbol{u}(\boldsymbol{x},t)\rangle$ is subtracted off of the total velocity $\boldsymbol{u}(\boldsymbol{x},t)$, leaving only the *fluctuating* component of the velocity $\boldsymbol{u}'(\boldsymbol{x},t)$ [41]:

$$\boldsymbol{u}'(\boldsymbol{x},t) \equiv \boldsymbol{u}(\boldsymbol{x},t) - \langle \boldsymbol{u}(\boldsymbol{x},t)\rangle \tag{B.1}$$

In what follows, the spatial and time dependencies are implied, and will be dropped for convenience. Beginning with the total continuity equation $\nabla \cdot \boldsymbol{u} = 0$ and substituting in the decomposition from Equation B.1, we can arrive at the mean and fluctuating continuity equations. Cartesian tensor notation will be employed for convenience, noting $\boldsymbol{u} = u_i$, $\langle \boldsymbol{u}\rangle = \langle u_i\rangle$, $\boldsymbol{u}' = u_i'$, and $\nabla \cdot \boldsymbol{u} = \frac{\partial u_i}{\partial x_i}$, with $x_i = \boldsymbol{x}$.

$$\frac{\partial u_i}{\partial x_i} = 0$$

$$\frac{\partial}{\partial x_i}\left(\langle u_i \rangle + u_i'\right) = 0$$

$$\frac{\partial}{\partial x_i}\langle u_i \rangle + \frac{\partial}{\partial x_i} u_i' = 0 \tag{B.2}$$

$$\left\langle \frac{\partial}{\partial x_i}\langle u_i \rangle + \frac{\partial}{\partial x_i} u_i' \right\rangle = 0 \tag{B.3}$$

$$\frac{\partial}{\partial x_i}\langle\langle u_i \rangle\rangle + \frac{\partial}{\partial x_i}\langle u_i' \rangle = 0 \tag{B.4}$$

$$\frac{\partial}{\partial x_i}\langle u_i \rangle + 0 = 0 \tag{B.5}$$

$$\frac{\partial}{\partial x_i}\langle u_i \rangle = 0 \tag{B.6}$$

In Equation B.3, the ensemble average of the entire continuity equation was taken, and in Equation B.4, it was brought inside of the derivative. Two rules of ensemble averaging were then applied, namely the average of an average is an average, $\langle\langle u_i \rangle\rangle = \langle u_i \rangle$, and the average of the fluctuating components is always zero, $\langle u_i' \rangle = 0$. This led to Equations B.5 and then B.6, the mean continuity equation. If Equation B.6 is substituted into Equation B.2, we can arrive at the fluctuating continuity equation.

$$\frac{\partial}{\partial x_i} u_i' = 0 \tag{B.7}$$

Equations B.6 and B.7, as well as the rules applied to Equation B.4, are useful when performing an ensemble average on the momentum equation, which yields the Reynolds stress term. Again, Cartesian tensor notation will be employed for the derivation. Note that density and viscosity are assumed to be constant in this derivation (and in all simulations performed).

$$\frac{\partial}{\partial t}u_j + \frac{\partial}{\partial x_i}u_i u_j = -\frac{1}{\rho}\frac{\partial}{\partial x_j}p + \nu\frac{\partial^2}{\partial x_i \partial x_i}u_j \tag{B.8}$$

$$\frac{\partial}{\partial t}\left(\langle u_j\rangle + u_j'\right) + \frac{\partial}{\partial x_i}\left[(\langle u_i\rangle + u_i')(\langle u_j\rangle + u_j')\right] = -\frac{1}{\rho}\frac{\partial}{\partial x_j}\left(\langle p\rangle + p'\right) + \nu\frac{\partial^2}{\partial x_i \partial x_i}\left(\langle u_j\rangle + u_j'\right) \tag{B.9}$$

$$\frac{\partial}{\partial t}\langle u_j\rangle + \frac{\partial}{\partial t}u_j' + \frac{\partial}{\partial x_i}\left[\langle u_i\rangle\langle u_j\rangle + \langle u_i\rangle u_j' + u_i'\langle u_j\rangle + u_i'u_j'\right] = -\frac{1}{\rho}\left[\frac{\partial}{\partial x_j}\langle p\rangle + \frac{\partial}{\partial x_j}p'\right] + \nu\left[\frac{\partial^2}{\partial x_i \partial x_i}\langle u_j\rangle + \frac{\partial^2}{\partial x_i \partial x_i}u_j'\right] \tag{B.10}$$

$$\left\langle \frac{\partial}{\partial t}\langle u_j\rangle + \frac{\partial}{\partial t}u_j' + \frac{\partial}{\partial x_i}\left[\langle u_i\rangle\langle u_j\rangle + \langle u_i\rangle u_j' + u_i'\langle u_j\rangle + u_i'u_j'\right]\right\rangle = \left\langle -\frac{1}{\rho}\left[\frac{\partial}{\partial x_j}\langle p\rangle + \frac{\partial}{\partial x_j}p'\right] + \nu\left[\frac{\partial^2}{\partial x_i \partial x_i}\langle u_j\rangle + \frac{\partial^2}{\partial x_i \partial x_i}u_j'\right]\right\rangle \tag{B.11}$$

$$\frac{\partial}{\partial t}\langle u_j\rangle + \frac{\partial}{\partial x_i}\left[\langle u_i\rangle\langle u_j\rangle + \langle u_i'u_j'\rangle\right] = -\frac{1}{\rho}\frac{\partial}{\partial x_j}\langle p\rangle + \nu\frac{\partial^2}{\partial x_i \partial x_i}\langle u_j\rangle \tag{B.12}$$

where ρ is the density, ν the kinematic viscosity, p the pressure, $\frac{\partial^2}{\partial x_i \partial x_i}$ is the Laplacian, ∇^2, and $\langle u_i'u_j'\rangle$ is the Reynolds stress tensor. Similar to the process followed for Equations B.2 through B.6, the Reynolds decomposition of velocity was substituted into the momentum equation (B.8) to yield Equation B.9. The velocity terms were expanded in Equation B.10, and the ensemble average taken in Equation B.11. The same ensemble averaging rules were applied to Equation B.11: $\langle\langle u_i\rangle\rangle = \langle u_i\rangle$, and $\langle u_i'\rangle = 0$, both of which are true for u_j, u_j', and p. This resulted in Equation B.12, and the desired form of the momentum equation. Expanded into matrix form, the Reynolds stress tensor is symmetric, and becomes

$$\begin{bmatrix} \langle u_i'u_i'\rangle & \langle u_i'u_j'\rangle & \langle u_i'u_k'\rangle \\ \langle u_j'u_i'\rangle & \langle u_j'u_j'\rangle & \langle u_j'u_k'\rangle \\ \langle u_k'u_i'\rangle & \langle u_k'u_j'\rangle & \langle u_k'u_k'\rangle \end{bmatrix}$$

APPENDIX C

FURTHER TURBULENT BENCHMARK RESULTS

Table C.1. Tabulated results for $Re_\tau \approx 180$

Mean flow variables for $Re_\tau \approx 180$			
Name	Formula	Moser, *et al.* [29]	CFD Result
Re_τ	$\frac{u_\tau \delta}{\nu}$	≈ 180	180.0573
Re_c	$\frac{U_c \delta}{\nu}$	≈ 3300	3308.846
Re_m	$\frac{U_m 2\delta}{\nu}$	≈ 5600	5663.030
-	$\frac{U_m}{u_\tau}$	15.63	15.72535
-	$\frac{U_c}{u_\tau}$	18.20	18.37657
-	$\frac{U_c}{U_m}$	1.16	1.168578
C_f	$\frac{\tau_w}{\frac{1}{2}\rho U_m^2}$	8.118 x 10^{-3}	8.087611 x 10^{-3}
C_{f0}	$\frac{\tau_w}{\frac{1}{2}\rho U_c^2}$	6.042 x 10^{-3}	5.922501 x 10^{-3}

Table C.2. Tabulated results for $Re_\tau \approx 395$

Mean flow variables for $Re_\tau \approx 395$			
Name	Formula	Moser, *et al.* [29]	CFD Result
Re_τ	$\frac{u_\tau \delta}{\nu}$	392.24	389.1105
Re_c	$\frac{U_c \delta}{\nu}$	7896.97	7902.024
Re_m	$\frac{U_m 2\delta}{\nu}$	11726.9	11718.30
-	$\frac{U_m}{u_\tau}$	14.9486	15.05750
-	$\frac{U_c}{u_\tau}$	20.133	20.3079
-	$\frac{U_c}{U_m}$	1.3468	1.34831
C_f	$\frac{\tau_w}{\frac{1}{2}\rho U_m^2}$	8.950 x 10^{-3}	8.8210 x 10^{-3}
C_{f0}	$\frac{\tau_w}{\frac{1}{2}\rho U_c^2}$	4.934 x 10^{-3}	4.8497 x 10^{-3}

Table C.3. Tabulated results for $Re_\tau \approx 590$

Mean flow variables for $Re_\tau \approx 590$			
Name	Formula	Moser, *et al.* [29]	CFD Result
Re_τ	$\frac{u_\tau \delta}{\nu}$	587.19	588.6635
Re_c	$\frac{U_c \delta}{\nu}$	12485.4	12731.67
Re_m	$\frac{U_m 2\delta}{\nu}$	18890.8	18978.30
-	$\frac{U_m}{u_\tau}$	16.0858	16.14880
-	$\frac{U_c}{u_\tau}$	21.263	21.6670
-	$\frac{U_c}{U_m}$	1.3218	1.34171
C_f	$\frac{\tau_w}{\frac{1}{2}\rho U_m^2}$	7.729 x 10^{-3}	7.6690 x 10^{-3}
C_{f0}	$\frac{\tau_w}{\frac{1}{2}\rho U_c^2}$	4.424 x 10^{-3}	4.2602 x 10^{-3}

BIBLIOGRAPHY

[1] Residual fuel oil prices by sales type. Tech. rep., Energy Information Administration, U.S. D.O.E.

[2] Basic principles of ship propulsion. Tech. rep., The MAN Diesel Group, 2004. http://www.manbw.com/files/news/filesof3859/P254-04-04.pdf.

[3] *Pocket Guide to Transportation 2008*. U.S. Department of Transportation, Washington,DC, USA, 2008. http://www.bts.gov/publications/pocket_guide_to_transportation/2008/pdf%/entire.pdf.

[4] Personal communication, N. Gopalakrishnan, 8 April 2008. Electrical Engineer [Maritime].

[5] Anderson, J.D. *Computational Fluid Dynamics: The Basics with Applications*. McGraw-Hill, New York, NY, USA, 1995.

[6] Aubé, F. Guide for computing CO_2 emissions related to energy use. Tech. rep., CANMET Energy Diversification Research Laboratory, 2001. http://cetc-varennes.nrcan.gc.ca/fichier.php/codectec/En/2001-66/2001-6%6e.pdf.

[7] Barthlott, W., and Neinhuis, C. Purity of the sacred lotus, or escape from contamination in biological surfaces. *Planta 202*, 1 (1997).

[8] Bushnell, Dennis M., and Hefner, Jerry M. *Viscous Drag Reduction in Boundary Layers*. American Institute of Aeronautics and Astronautics, Washington, DC, USA, 1990.

[9] Chen, W., Fadeev, A.Y., and M.C. Hsieh, *et al.* Ultrahydrophobic and ultralyophobic surfaces: some comments and examples. *Langmuir 15* (1999), 3395.

[10] Choi, H., Moin, P., and Kim, J. Direct numerical simulation of turbulent flow over riblets. *Journal of Fluids Mechanics 255* (1993), 503–539.

[11] Daniello, R., Waterhouse, N. E., and Rothstein, J. P. Turbulent drag reduction using ultrahydrophobic surfaces. Submitted to Physical Review Letters, 2008.

[12] Davies, J., Maynes, D., Webb, B.W., and Woolford, B. Laminar flow in a microchannel with superhydrophobic walls exhibiting transverse ribs. *Physics of Fluids 18* (2006), 087110:1–087110:11.

[13] de Bruyn Kops, S.M., and Riley, J.J. Direct numerical simulation of laboratory experiments in isotropic turbulence. *Physics of Fluids 10* (1998), 2125–2127.

[14] Deen, W.M. *Analysis of Transport Phenomena*. Oxford University Press, New York, NY, USA, 1998.

[15] Ferziger, J.H., and Peric, M. *Computational Methods for Fluid Dynamics*. Springer, Berlin, 2002.

[16] Fukagata, K., Kasagi, N., and Koumoutsakos, P. A theoretical prediction of friction drag in turbulent flow by superhydrophobic surfaces. *Physics of Fluids 18* (2006), 051703:1 – 051703:4.

[17] Gadebusch, J. On the development of self-adapting (RANS/LES) turbulence models for fluid simulation at any mesh resolution. Master's thesis, The University of Massachusetts, Amherst, 2007.

[18] Gogte, S., Vorobieff, P., Truesdell, R., Mammoli, A., van Swol, F., Shah, P., and Brinker, C. J. Effective slip on textured superhydrophobic surfaces. *Physics of Fluids 17* (2005), 051701:1–051701:4.

[19] Hahn, S., Je, J., and Choi, H. Direct numerical simulation of turbulent channel flow with permeable walls. *Journal of Fluid Mechanics 450* (2002), 259–285.

[20] Isrealachvili, J.N. *Intermolecular and surfaces forces: with applications to colloidal and biological systems*. Addison Wesley, 2004.

[21] Joseph, P., Cottin-Bizonne, C., Benot, J.-M., Ybert, C., Journet, C., Tabeling, P., , and Bocquet, L. Slippage of water past superhydrophobic carbon nanotube forests in microchannels. *Physical Review Letters 97*, 15 (2006), 156104–1:156104–4.

[22] Kim, J. Active control of turbulent boundary layers for drag reduction. *Lecture Notes in Physics 529* (1999), 142–152.

[23] Kim, John, Moin, Parviz, and Moser, Robert. Turbulence statistics in fully developed channel flow at low Reynolds number. *Journal of Fluid Mechanics 177* (1987), 133–166.

[24] Lauga, J., and Stone, H. Effective slip in pressure-driven stokes flow. *Journal of Fluid Mechanics 489* (2003), 55–77.

[25] Maynes, D., and Webb, B. W. Fully developed electro-osmotic heat transfer in microchannels. *International Journal of Heat and Mass Transfer 46*, 8 (2003).

[26] Min, T., and Kim, J. Effects of hydrophobic surface on skin-friction drag. *Physics of Fluids 16*, 7 (2004), L55–L58.

[27] Min, T., and Kim, J. Effects of hydrophobic surface on stability and transition. *Physics of Fluids 17* (2005), 108106:1–108106:4.

[28] Mittal, R., and Moin, P. Suitability of upwind-biased finite difference schemes for large-eddy simulation of turbulent flows. *American Institute of Aeronautics and Astronautics Journal 35*, 8 (1998).

[29] Moser, R., Kim, J., and Mansour, N. Direct numerical simulation of turbulent channel flow up to $\mathrm{Re}_\tau = 590$. *Physics of Fluids 11*, 4 (1998), 943–945.

[30] Murai, Y., Oiwa, H., and Takeda, Y. Frictional drag reduction by bubbles in taylor-couette flow. *APS Meeting Abstracts* (Nov. 2006).

[31] Nilsson, M. Exploring fundamental turbulent physics using Direct Numerical Simulations. Master's thesis, The University of Massachusetts, Amherst, 2008.

[32] Oner, D., and McCarthy, T.J. Ultrahydrophobic surfaces. Effects of topography length scales on wettability. *Langmuir 16* (2000), 7777.

[33] Ou, J., Perot, J.B., and Rothstein, J. Laminar drag reduction in microchannels using superhydrophobic surfaces. *Physics of Fluids 16*, 12 (2004), 4635–4643.

[34] Ou, J., and Rothstein, J. Direct velocity measurements of the flow past drag-reducing ultrahydrophobic surfaces. *Physics of Fluids 17*, 10 (2005), 13606:2–13606:10.

[35] Perot, J. B. An analysis of the fractional step method. *Journal of Computational Physics 108*, 1 (1993), 51–58.

[36] Perot, J. B. Comments on the fractional step method. *Journal of Computational Physics 121* (1995), 190.

[37] Perot, J. B. Conservation properties of unstructured staggered mesh schemes. *Journal of Computational Physics 159* (2000), 58–89.

[38] Perot, J.B., and Moin, P. Shear-free turbulent boundary layers. Part 1. Physical insights into near-wall turbulence. *Journal of Fluid Mechanics 295* (1995), 199.

[39] Philip, J.R. Flows satisfying mixed no-slip and no-shear conditions. *Journal of Applied Mathematics and Physics (ZAMP) 23* (1972), 353–371.

[40] Philip, J.R. Integral properties of flows satisfying mixed no-slip and no-shear conditions. *Journal of Applied Mathematics and Physics (ZAMP) 23* (1972), 960–968.

[41] Pope, S.B. *Turbulent Flows*. Cambridge University Press, New York, NY, USA, 2000.

[42] Sanders, W.C., Winkel, E.S., Dowling, D.R., Perlin, M., and Ceccio, S.L. Bubble friction drag reduction in a high-Reynolds-number flat-plate turbulent boundary layer. *Journal of Fluid Mechanics 552* (2006), 353–380.

[43] Shewchuk, J. R. An introduction to the conjugate gradient method without the agonizing pain. Tech. rep., Pittsburgh, PA, USA, 1994.

[44] Tretheway, D.C., and Meinhart, C.D. Apparent fluid slip at hydrophobic microchannel walls. *Physics of Fluids 14*, 3 (2002).

[45] Watanabe, K., Yanuar, and Udagawa, H. Drag reduction of Newtonian fluid in a circular pipe with highly water-repellant wall. *Journal of Fluids Mechanics 381* (1999), 225.

[46] White, Frank M. *Viscous Fluid Flow.* McGraw-Hill, Inc., New York,NY, USA, 1991.

[47] Wilcox, D. *Basic Fluid Mechanics.* DCW Industries, La Cañada, CA, USA, 2000.

[48] Ybert, C., Barentin, C., and Cottin-Bizonne, C. Achieving large slip with superhydrophobic surfaces: Scaling laws for generic geometries. *Physics of Fluids 19* (2007), 123601:1–123601:10.